

MEASUREMENTS AND MODELING OF ARCTIC ATMOSPHERIC
PROCESSES DURING THE NORWEGIAN YOUNG SEA ICE
FIELD CAMPAIGN

By

SARAH YVETTE MURPHY

A dissertation submitted in partial fulfillment of
the requirements for the degree of

DOCTOR OF PHILOSOPHY

WASHINGTON STATE UNIVERSITY
Voiland School of Engineering and Architecture

MAY 2023

©Copyright by SARAH YVETTE MURPHY, 2023
All Rights Reserved

©Copyright by SARAH YVETTE MURPHY, 2023
All Rights Reserved

To the Faculty of Washington State University:

The members of the Committee appointed to examine the dissertation of SARAH YVETTE MURPHY find it satisfactory and recommend that it be accepted.

Von P. Walden, Ph.D., Chair

Stephen Hudson, Ph.D.

Brian Lamb, Ph.D.

Heping Liu, Ph.D.

Hailong Wang, Ph.D.

ACKNOWLEDGEMENTS

The N-ICE field campaign was supported by the Norwegian Polar Institute’s Centre for Ice, Climate and Ecosystems (ICE) through the N-ICE project, and the Research Council of Norway through the STASIS project (221961/F20).

The modeling using the idealized version of WRF and the flux equation research (Chapters 5 and 6) were partially supported by the U.S. Department of Energy, Office of Science, Office of Workforce Development for Teachers and Scientists, Office of Science Graduate Student Research (SCGSR) program. The SCGSR program is administered by the Oak Ridge Institute for Science and Education (ORISE) for the DOE. ORISE is managed by ORAU under contract number DE-SC0014664. All opinions expressed in this document are the author’s and do not necessarily reflect the policies and views of DOE, ORAU, or ORISE.

NCAR’s Cheyenne supercomputer was used for all Polar WRF simulations except for the idealized WRF simulations. We would like to acknowledge high-performance computing support from Cheyenne (doi:10.5065/D6RX99HX) provided by NCAR’s Computational and Information Systems Laboratory, sponsored by the National Science Foundation.

The author would like to thank the Python community for the open-source data science tools, including wrf-python (Ladwig, 2017), xarray (Hoyer & Hamman, 2017), and matplotlib (Hunter, 2007). All were used extensively throughout this dissertation.

Chapter 3 was made possible with help from Dr. Keith Hines (Polar Meteorology Group, Byrd Polar and Climate Research Center at The Ohio State University), who provided useful insight to help get the Polar WRF model running on the Washington State University supercomputer. Dr. Hines also assisted in some early decisions regarding the setup of Polar WRF, including insight into input data sets and formatting of WRF configuration files.

Dr. Xiang-Yu Li (Pacific Northwest National Laboratory) helped with the setup of the idealized WRF model and troubleshooting some model issues. The author would like to thank him for the helpful conversations and for taking the time to help translate WRF error files.

Dr. Lana Cohen provided research advice from the perspective of someone who was on the ship at N-ICE and helped clarify some of the caveats of the measurement data. Conversations with her have helped with the details of Chapters 2 and 3.

This research for this dissertation was supported by the National Science Foundation grants PLR-1304657, PLR-1314248, NNA-1801764, OPP-2110341.

MEASUREMENTS AND MODELING OF ARCTIC ATMOSPHERIC
PROCESSES DURING THE NORWEGIAN YOUNG SEA ICE
FIELD CAMPAIGN

Abstract

by Sarah Yvette Murphy, Ph.D.
Washington State University
May 2023

Chair: Von P. Walden

The Arctic is warming more quickly than other regions, resulting in modifications to the surface energy budget. The Norwegian Young Sea Ice (N-ICE) field campaign took place in January through June 2015, monitoring key components of the surface energy budget. This was the first field campaign to take observations of the surface energy budget during the seasonal transition from winter to spring/summer since the Surface Heat Budget of the Arctic (SHEBA) field campaign in 1997 through 1998. These observations are valuable not only due to the amount of time that has passed since the SHEBA field experiment but also because N-ICE took place on younger, thinner sea ice, and in a different part of the Arctic. This study uses data from the N-ICE experiment to recommend improvements to the Polar Weather Research

and Forecasting (WRF) model. The goals of this study are: 1) compare atmospheric measurements to models, 2) investigate model cloud microphysics and boundary layer parameterizations within WRF, 3) determine what cloud properties were observed during N-ICE, 4) investigate the effects of turbulent fluxes and clouds on young sea ice, and 5) make recommendations for improving the Polar WRF model. The Polar WRF model results show that there were issues in calculating both the turbulent and radiative fluxes over first-year sea ice. The cloud conditions during N-ICE varied, and mixed-phase clouds (a mixture of water and ice) were seen throughout the entire experiment. The model, however, did not accurately simulate the radiative impacts of these clouds. To determine if the calculations of sensible and latent heat flux can be accurately estimated given the correct cloud conditions, a study was conducted comparing turbulent fluxes from the Maximum Entropy Production method and the bulk flux algorithm (based on Monin-Obukhov theory and the technique used to estimate fluxes within WRF). Sensible heat flux was accurately estimated, but all equations overestimated the amount of latent heat flux. When compared to an idealized (offline) version of the WRF model using the measured radiative fluxes as input, the WRF model estimates the turbulent fluxes well, indicating that the model is using an appropriate version of the flux equations and that most of the error within the model can be attributed to bias in the cloud properties.

TABLE OF CONTENTS

| | Page |
|--|------|
| ACKNOWLEDGEMENTS | iii |
| ABSTRACT | v |
| CHAPTER | |
| 1. THE ARCTIC ATMOSPHERE | 1 |
| The Arctic and Climate Change | 1 |
| Surface Energy Budget | 3 |
| Clouds: Longwave and Shortwave Radiation | 4 |
| Sensible and Latent Heat Flux | 5 |
| Arctic Measurements | 5 |
| Dissertation Outline and Attributions | 9 |
| 2. THE NORWEGIAN YOUNG SEA ICE FIELD CAMPAIGN | 13 |
| Introduction | 13 |
| Instruments | 16 |
| Atmospheric components of the surface energy budget over young sea ice | 18 |
| 3. SIMULATION OF ATMOSPHERIC CONDITIONS OVER FIRST-YEAR SEA ICE USING THE POLAR WEATHER RESEARCH AND FORE- CASTING MODEL | 20 |
| Introduction | 20 |
| Observations and Model Setup | 21 |

| | |
|--|----|
| Observations | 21 |
| Model Setup | 22 |
| Results | 28 |
| Skin Temperature | 30 |
| Longwave and Shortwave Fluxes | 34 |
| Turbulent Fluxes | 39 |
| Case Studies | 42 |
| Conclusions | 47 |
| 4. CLOUD MACROPHYSICAL AND RADIATIVE PROPERTIES OBSERVED DURING THE NORWEGIAN YOUNG SEA ICE FIELD CAMPAIGN | 49 |
| Introduction | 49 |
| Measurements | 53 |
| Methods | 56 |
| Cloud Macrophysical Properties | 56 |
| Cloud Radiative Properties | 58 |
| Results and Discussion | 62 |
| Cloud Radiative Properties | 66 |
| Cloud Radiative Forcing modeled by Polar WRF | 76 |
| Conclusions | 80 |
| 5. LATENT AND SENSIBLE HEAT FLUX CALCULATIONS OVER FIRST-YEAR SEA ICE | 82 |

| | |
|---|-----|
| Introduction | 82 |
| Calculating Sensible and Latent Heat Flux | 84 |
| Bulk Flux Algorithm | 85 |
| Maximum Entropy Production Method | 86 |
| Surface Stability | 87 |
| Observations | 90 |
| Results and Discussion | 91 |
| Stability Coefficients | 91 |
| Thermal Conductivity | 95 |
| Bulk Flux Algorithm | 95 |
| Maximum Entropy Production Method | 97 |
| Conclusions | 99 |
| 6. IMPROVEMENTS TO THE WEATHER RESEARCH AND FORECASTING MODEL OVER FIRST-YEAR SEA ICE | 101 |
| Introduction | 101 |
| Methods | 103 |
| Setting Surface Parameters | 106 |
| Turbulent Flux Equations | 108 |
| Results | 111 |
| Sensitivity to Surface Properties | 111 |
| Turbulent Flux Equations | 118 |

| | |
|---|------------|
| Conclusions | 120 |
| 7. CONCLUSIONS, RECOMMENDATIONS, AND FUTURE WORK | 121 |
| Conclusions | 121 |
| Recommendations | 123 |
| Setting Surface Parameters | 123 |
| Turbulent Flux Equations | 124 |
| Future Work | 125 |
| Flux Equations | 125 |
| Clouds Microphysics Schemes | 125 |
| Ice Surface Heterogenities | 127 |
| BIBLIOGRAPHY | 128 |
| APPENDIX | |
| A. GLOSSARY | 141 |
| Acronyms | 141 |
| Constants and Variables | 144 |
| Alphabetical | 144 |
| Greek Letters | 148 |
| B. THE EFFECT OF DATA GAP FILLING ON SENSIBLE HEAT FLUX CALCULATIONS | 150 |
| Introduction | 150 |
| Methods | 152 |

| | |
|--|-----|
| Results and Discussion | 154 |
| Barrow, Alaska – Quality Checking of Filling Algorithm | 154 |
| N-ICE Filled Data Comparison | 159 |
| Future Work | 162 |
| Conclusion | 165 |
| C. ADDITIONAL POLAR WRF VALIDATION STATISTICS | 166 |

LIST OF FIGURES

| | Page |
|--|------|
| 1.1 Flowchart of dissertation chapters. | 10 |
| 2.1 N-ICE location. | 14 |
| 3.1 WRF Model Domain | 23 |
| 3.2 WRF Model physics scheme exchanges. | 26 |
| 3.3 Polar WRF simulated pressure, temperature, sensible and latent heat flux, components of longwave and shortwave flux, and cloud fraction time series. | 29 |
| 3.4 Polar WRF simulated temperature histograms. | 33 |
| 3.5 Polar WRF simulated net longwave flux histograms. | 35 |
| 3.6 Polar WRF simulated net shortwave flux histograms. | 36 |
| 3.7 Polar WRF simulated cloud fraction. | 37 |
| 3.8 Polar WRF simulated latent heat flux histograms. | 39 |
| 3.9 Polar WRF simulated sensible heat flux histograms. | 40 |
| 3.10 Polar WRF Case 1 - Winter cold front (5 Feb 2015) time series . . . | 43 |
| 3.11 Polar WRF Case 2 - Spring clear-sky (23 May 2015) time series . . . | 46 |
| 4.1 RRTM modeled downward flux bias histogram. | 61 |
| 4.2 Cloud fraction and phase, height, and temperature time series. | 63 |
| 4.3 Cloud base height by month histogram. | 65 |
| 4.4 Shortwave, longwave, and net radiative components of flux. | 67 |

| | | |
|------|--|-----|
| 4.5 | Shortwave, longwave, and net components of cloud radiative forcing. | 70 |
| 4.6 | Histograms of cloud radiative forcing by season. | 71 |
| 4.7 | Cloud radiative forcing vs cloud base height, cloud base temperature, cloud fraction, and water cloud fraction for winter. | 73 |
| 4.8 | Cloud radiative forcing vs cloud base height, cloud base temperature, cloud fraction, and water cloud fraction for summer. | 74 |
| 4.9 | Time series of cloud radiative forcing in two WRF model runs. | 77 |
| 4.10 | Histograms of cloud radiative forcing in two WRF model runs. | 78 |
| 5.1 | Obukhov length | 92 |
| 5.2 | Sensible heat flux from the bulk flux method compared to EddyPro. | 96 |
| 5.3 | Latent heat flux from the bulk flux method compared to EddyPro. | 96 |
| 5.4 | Sensible heat flux from the MEP method compared to EddyPro. | 98 |
| 5.5 | Latent heat flux from the MEP method compared to EddyPro. | 98 |
| 6.1 | Idealized Case 1 | 114 |
| 6.2 | Idealized Case 2 | 116 |
| 6.3 | Idealized Case 3 | 117 |
| 6.4 | Sensible heat flux observed at N-ICE and calculated from Polar WRF offline translated code. | 119 |
| 6.5 | Friction velocity observed at N-ICE and calculated from Polar WRF offline translated code. | 119 |
| 6.6 | Latent heat flux observed at N-ICE and calculated from Polar WRF offline translated code. | 120 |
| B.1 | Barrow, Alaska sensible heat flux | 156 |

| | |
|---|-----|
| B.2 Barrow, Alaska power spectra | 160 |
| B.3 N-ICE sensible heat flux | 163 |
| B.4 N-ICE percent differences between filled and unfilled datasets. | 164 |

LIST OF TABLES

| | Page |
|---|------|
| 2.1 N-ICE floe dates and ice edge proximity. | 14 |
| 3.1 WRF input datasets, dates, and settings. | 24 |
| 3.2 Cloud microphysics and planetary boundary layer schemes used in polar WRF simulations. | 27 |
| 3.3 Polar WRF mean model bias and mean modeled flux for temperature, latent heat flux, sensible heat flux, net longwave flux, and net shortwave flux. | 31 |
| 3.4 Polar WRF mean absolute error for temperature, latent heat flux, sensible heat flux, net longwave flux, and net shortwave flux. | 32 |
| 5.1 Scaling parameter equations. | 89 |
| 5.2 Sensible and latent heat flux mean bias and mean flux for each scaling function relationship. | 93 |
| 5.3 Sensible and latent heat flux mean absolute error for each scaling function relationship. | 94 |
| 5.4 Thermal conductivity and thermal inertia. | 95 |
| 6.1 Snow and ice settings in LANDUSE.TBL. | 105 |
| 6.2 N-ICE average measured albedo. | 106 |
| 6.3 Recommended LANDUSE.TBL values. | 112 |
| 6.4 Mean model bias comparison for idealized WRF runs with modified LANDUSE.TBL values. | 112 |
| C.1 Polar WRF CRF mean modeled bias, flux, and absolute error. | 166 |

CHAPTER ONE

THE ARCTIC ATMOSPHERE

Loss of multi-year sea ice and the occurrence of a seasonally ice-free Arctic Ocean by the middle of this century will result in substantial range contraction, if not the disappearance of several Arctic fish, crab, bird, and marine mammal species, including possible extinction of seals and polar bears in certain regions (high confidence).

- Intergovernmental Panel on Climate Change (IPCC)
Sixth Assessment Report, August 2021

1.1 The Arctic and Climate Change

The largest impacts of climate change are those seen in the Arctic. Over the past two decades, Arctic temperatures have increased by more than 2 times the global rate (Core Writing Team & , eds.). Changes occurring in the Arctic modify the atmospheric circulation, impacting both cloudiness and radiation at the surface (Zhang et al., 2008).

Arctic amplification is a series of mechanisms in which the polar regions undergo positive feedback loops which can change the energy balance at the surface. Arctic amplification includes the ice-albedo effect, which amplifies temperature increases due to greenhouse gas emissions by melting sea ice. As sea ice melts, the albedo of the surface decreases, resulting in more solar energy absorption. As the surface absorbs more solar energy, it warms, increasing Arctic air temperatures, which melts additional sea ice. This is a key example of a positive feedback loop (Arias et al., 2021). A second example of Arctic amplification occurs when permafrost thaws,

releasing stored methane into the atmosphere. This increase in atmospheric methane mixes globally, and increases the greenhouse effect everywhere, further increasing permafrost melt. While this is not the focus of this study, it is important to note and can impact global temperatures. To fully understand Arctic climate change, it is crucial for scientists to study this region and the physical processes that contribute to Arctic amplification.

Arctic climate change heavily impacts marine life, indigenous people, and coastal ecosystems (Arias et al., 2021). Beyond these local effects, changes in Arctic sea ice can also cause irreversible changes in the atmospheric and oceanic circulation. Many of the Coupled Model Intercomparison Project Phase 5 (CMIP5) models indicate that within the next few years, the Earth may experience a completely ice-free Arctic during the summer (Stroeve & Notz, 2018).

Sea ice has been declining at an increasing rate throughout the last decade due to lengthened melt seasons replacing multi-year sea ice with thin, first-year sea ice (Meier et al., 2014). Multi-year sea ice can be defined as sea ice that does not completely melt in the summer. Conversely, first-year sea ice melts completely each summer and re-freezes the following winter. Wunderling et al. (2020) found that 55% of the additional warming in the Arctic was a result of the ice-albedo feedback. The rest is attributed to a change in lapse rate and cloud properties resulting in increased surface heating. Overall, these changes have resulted in an ice loss of approximately 3.4% per decade. Multi-year sea ice has decreased from 59% of the ice pack to 28% in 2018 and continues to decrease (Stroeve & Notz, 2018). The fraction of first-year ice has increased as a result. As a consequence of this, there is a need to fully understand atmosphere-ocean interactions over first-year ice. This movement toward

a new ice regime has been referred to as a shift toward a new climate state in the Arctic (Verlinde et al., 2007).

1.2 Surface Energy Budget

The surface energy budget can influence ice growth or melt. A study done using results from the Surface Heat Budget of the Arctic Ocean (SHEBA, described in Section 1.3) field experiment over sea ice shows that the ice and snow thickness have significant impacts on the surface temperature and, as a result, the surface energy budget, due to the changes in heat transfer through the snow and ice (Hines et al., 2015). Additionally, the surface energy budget is often misrepresented in models due to an underestimation of cloud cover, resulting in downward longwave radiation biases (Inoue et al., 2008). Eq. 1.1 and 1.2 show the net radiation and surface energy budget equations.

$$Q_{net} = (Q_{sw\downarrow} - Q_{sw\uparrow}) + (Q_{lw\downarrow} - Q_{lw\uparrow}) \quad (1.1)$$

$$R = Q_{net} + H_s + H_l \quad (1.2)$$

Q_{sw} and Q_{lw} are the shortwave and longwave radiative fluxes, respectively, with the arrow denoting upward (\uparrow) vs downward (\downarrow) flux, R is the residual flux, including heat transfer through the ice and heat storage, and H_s and H_l are the sensible and latent heat fluxes. While net radiative flux can easily be measured or estimated given temperature profiles and cloud cover, values such as the sensible and latent heat fluxes are not as straightforward to estimate. Models often have skill in one value but have large compensating errors in other values. These values are heavily influenced by both the clouds and the near-surface boundary layer structure (Tjernström et al., 2005).

1.2.1 Clouds: Longwave and Shortwave Radiation

Properties such as proximity to melt ponds/open water, the shape of the snow crystals, and snow depth, can all influence how clouds modify surface radiation. Due to complexities in cloud feedbacks and the underlying surface, there are a variety of ways models handle cloud formation and properties. Arctic atmospheric models, while key to understanding cloud processes, are not perfect and still have trouble quantifying these processes.

A key feedback mechanism in the arctic regions is the cloud radiation feedback, which, unlike other Arctic amplification feedbacks, can be either positive or negative depending on influences such as the cloud properties and sun angle. This process applies all over the globe, but due to the high surface albedo and lack of atmospheric moisture, it has a greater potential to influence the surface radiation budget in the Arctic. Further research is still necessary to quantify the exact influence. When clouds are lower in the atmosphere or are more optically thick they emit more long-wave radiation. However, a cooler cloud, one higher in the atmosphere, or optically thin, would radiate less longwave radiation, but still more than under clear-sky conditions. This is an example of how clouds can warm the surface. Clouds can cool the surface as a result of their shortwave impact. The higher the cloud's albedo (higher optical thickness and droplet size), the more shortwave radiation is reflected away, not reaching the surface, and not being included in the surface energy budget. Intrieri et al. (2002) studied the radiative influence of clouds at SHEBA and found that, for their location northeast of Alaska, the net cloud effect was to warm the surface through most of the year. There was only a short two-week period in the middle of the summer, when the location was getting the most direct solar radiation and had

the lowest surface albedo, when clouds had a cooling influence by reflecting shortwave radiation away from the surface.

Cloud radiative forcing (CRF) is often used to quantify the impacts of clouds on surface radiation. This is defined in Eq. 1.3, but can be conceptually understood as the difference between the surface radiation in the absence of clouds (Q_{clear}) and the actual (or all-sky) radiation ($Q_{all} = Q_{net}$). A large positive (negative) cloud radiative forcing indicates surface warming (cooling) due to cloud radiative influence.

$$CRF = Q_{all} - Q_{clear} \quad (1.3)$$

1.2.2 Sensible and Latent Heat Flux

The near-surface planetary boundary layer (PBL) is often strongly stable in the Arctic due to significant surface longwave radiative cooling that is not compensated for by other energy sources. This is mainly due to the low level of solar heating as a result of little incoming sunlight much of the year and generally high surface albedo. Additionally, the latent heat of phase change in the surface during the melt season acts to cool the air closest to the surface, creating a stable boundary layer. Global models, however, often have a difficult time simulating these strongly stable conditions, and either form a PBL not stable enough or too stable for actual conditions. Regional models are generally better than this and can be used to improve larger-scale models, but there is still a need for further model improvement (Tjernström et al., 2005).

1.3 Arctic Measurements

One of the first major experiments studying meteorology and ice dynamics in the Arctic Ocean took place between 1975 and 1976. This experiment, The Arctic

Ice Dynamics Joint Experiment (AIDJEX), was led by the University of Washington and consisted of four ice camps with surrounding buoys (Untersteiner, 1980). Taking measurements over sea ice is both dangerous and difficult as deployment and maintenance is nearly impossible without the aid of a ship. Another way of taking in-situ measurements includes floating buoys, but the measurement capabilities of buoys are limited by the lack of available onboard power. Research vessels are utilized for their ability to provide power, transportation, and housing for scientists while observing the Arctic.

A series of ship-borne experiments took place between 1991 and 2001: the International Arctic Ocean Experiment (AOE) (1991), AOE-96 (1996) (Tjernström et al., 2004), SHEBA (October 1997 - October 1998) (Uttal et al., 2002), and AOE (2001). The earlier two AOE focused on atmospheric aerosols and did not include vertical profiles of atmospheric structure or ice characteristics. The 2001 AOE experiment focused more extensively on meteorological variables (Tjernström et al., 2004). SHEBA had a larger array of meteorological instruments, observing both the cloud properties and the surface energy budget over sea ice for an entire year (Uttal et al., 2002). Before the Norwegian Young Sea Ice Campaign (N-ICE2015 or N-ICE) took place in January through June of 2015, SHEBA was the most recent experiment to observe these atmospheric properties.

Other experiments since SHEBA, such as the Arctic Clouds in Summer Experiment (ACSE) (Sotiropoulou et al., 2016), and the Mixed-Phase Arctic Cloud Experiment (Verlinde et al., 2007) have not observed winter or took place over a shorter duration than N-ICE. Prior to SHEBA, field experiments such as the Seasonal Ice Zone Experiment, Coordinated Eastern Arctic experiment, Marginal Ice Zone Exper-

iments, Arctic Ice Dynamics Joint Experiment, and the Soviet and Russian drifting stations (Vihma & Pirazzini, 2005; Kahl et al., 1999) that collected meteorological and radiation data over Arctic sea ice either covered a small area or had poor temporal resolution. However, these studies have used observations of cloud cover, albedo, and cloud properties to provide estimates of the surface energy budget. Comparing SHEBA data to these estimates showed that during transition seasons (September, October, November, March, and April), the SHEBA time period had larger incoming longwave radiation and a smaller magnitude of shortwave radiation, sensible heat flux, and latent heat flux compared to other studies. This could be caused by a higher frequency of warm air masses, an increase in cloud cover, or a combination of both (Persson, 2002).

SHEBA took place onboard a Canadian Coast Guard ice breaker, the Des Groseillers, in the Beaufort Sea north of Alaska from 1997 to 1998 (Uttal et al., 2002; Shupe & Intrieri, 2004). The ship sailed north from Alaska and was intentionally frozen into the sea ice and allowed to drift with the ice (Uttal et al., 2002). Helicopter flights also surveyed the area to document the ice conditions surrounding the ship and a tethered balloon was utilized to observe the boundary layer conditions. The primary goals of this experiment were to observe the changes occurring in the surface energy budget over sea ice as the polar regions undergo global warming with the hope that these observations can give both context to the poorly understood mechanisms occurring under these never-before-observed conditions and to provide observations to validate and improve general circulation models in the Arctic (Uttal et al., 2002). Particular focus was on ocean-ice-atmosphere feedback, such as the ice-albedo and cloud-radiation feedback during the entire annual cycle.

The ice pack SHEBA was frozen into varied in thickness from 1.8 m (October) to 2.6 m (June) and was classified as multiyear sea ice, indicating this ice pack had not completely melted the previous summer. Snowpack was also observed on the ice throughout the experiment, reaching a maximum depth in June, when 30 cm of snow fell but melted quickly in the following days (Uttal et al., 2002). Multi-year sea ice is becoming less prominent in the polar regions, and first-year sea ice is beginning to dominate the Arctic. This shift away from the conditions seen at SHEBA and toward thinner, first-year sea ice motivated N-ICE2015, which observed conditions over young sea ice and is described in Chapter 2.

During the start of SHEBA, the western Arctic had an anomalously large amount of multi-year ice. In addition, the autumn upper ocean had a lower salinity and warmer temperature than expected, indicating a larger ocean heat flux than was typical of the area during the summer. Comparing SHEBA data to estimates from other field experiments showed that during transition seasons (September, October, November, March, and April), SHEBA observed incoming longwave radiation that was 2 to 45 Wm^{-2} more than other studies. This could be caused by either an increase in the number of warm air masses over SHEBA or an increase in cloud cover (Persson, 2002). SHEBA was an important field experiment that filled many gaps in our understanding of cloud and radiation processes. One of the most important findings from SHEBA was that, even at temperatures well below freezing, mixed-phase clouds occurred often.

SHEBA took place over thick, multi-year sea ice. The Arctic is shifting toward a new regime dominated by thin, first-year sea ice, so observations over first-year sea ice are necessary to understand these increasingly more dominant conditions. Since

N-ICE, there has been one major field campaign with the goal of observing the Arctic climate system onboard an icebreaker ship (Shupe et al., 2020). The Multidisciplinary drifting Observatory for the Study of Arctic Climate (MOSAiC) was a year-long field expedition that took place in the central Arctic in 2019. Much like SHEBA, MOSAiC took place further north than N-ICE and was primarily over multi-year sea ice (Munoz-Martin et al., 2020). This shift toward an Arctic dominated by first-year sea ice and the lack of measurements over first-year sea ice are the primary motivations of N-ICE. Chapter 2 gives details of N-ICE, including instruments deployed and driving questions.

1.4 Dissertation Outline and Attributions

This dissertation aims to:

1. Compare atmospheric measurements to models (Chapter 3)
2. Investigate combinations of cloud microphysics and boundary layer physics options within WRF (Chapter 3)
3. Explore the cloud conditions seen at N-ICE (Chapter 4)
4. Investigate the effects of turbulent fluxes and clouds on young sea ice (Chapter 5 and 6)
5. Make recommendations for improving the Polar WRF model (Chapter 7)

Figure 1.1 is a flowchart showing all of the following chapters and how they tie together. Chapter 2 describes the general aspects of the N-ICE field campaign that are common to all subsequent chapters.

Chapter 3 presents model simulations performed by the Polar Weather Research Forecasting (Polar WRF) model and compares the various schemes used for the planetary boundary layer and cloud microphysical properties. The model simulations are summarized in terms of how well they compared with the N-ICE measurements. This work was completed on the Cheyenne (Computational & Laboratory, 2019) supercomputer by Murphy with guidance from Dr. Keith Hines. This chapter was written with the intention to submit as a publication to the American Geophysical Union (AGU) Journal of Advances in Modeling Earth Systems.

Chapter 4 provides detail on the measurements of cloud radiative properties during N-ICE and how they relate to the Polar WRF simulations. The analysis for this

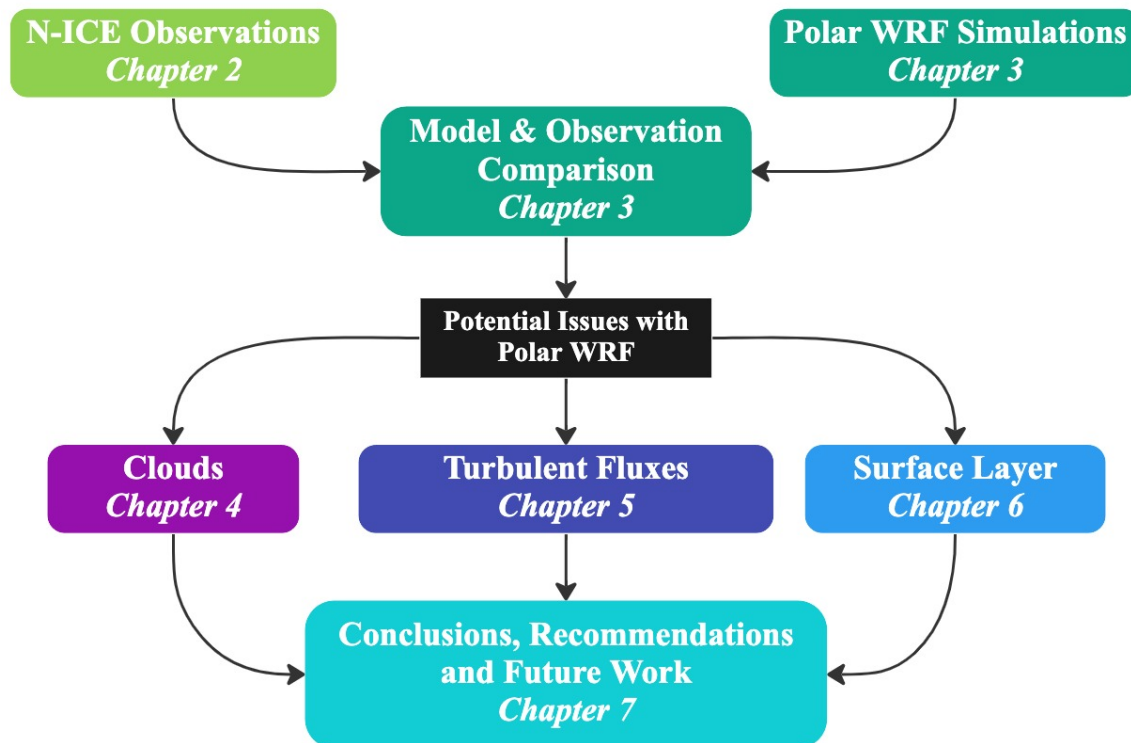


Figure 1.1: A flowchart showing how each chapter of this dissertation ties together. Boxes are colored by chapter.

chapter was completed by Murphy, with LiDAR processing and section 4.3.1 being completed by Dr. Robert Stillwell. Dr. Von Walden and Dr. Stephen Hudson were advisors on this research. This chapter was written for submission to the Journal of Geophysical Research (JGR) Atmospheres journal.

Chapter 5 compares the turbulent fluxes observed at N-ICE to fluxes calculated using the Maximum Entropy Production method and a bulk flux algorithm. These methods of calculating fluxes depend on exchange coefficients and surface stability, which are also explored in Chapter 5. All research, coding, analysis, and writing was completed by Sarah with advice from Drs. Hailong Wang and Von P. Walden. This research was done in collaboration with Pacific Northwest National Laboratory as part of the Department of Energy's Office of Science Graduate Student Research Program (DOE SCGSR).

The equations used in the Polar WRF model are described in detail in Chapter 6, comparing them to the methods of calculating flux in Chapter 5. This chapter uses the measurements described in Chapter 4, the equations explored in Chapter 5, and the modeling schemes detailed in Chapter 3 to conduct sensitivity studies to changes within WRF. This work will also be submitted to AGU's Journal of Advances in Modeling Earth Systems.

Chapter 7 wraps up this dissertation by summarizing the findings in Chapters 3 through 6. This chapter also includes suggestions for changes to the WRF model and topics for future research, including how the cloud properties could be further explored to improve radiation in the model.

In addition to the work presented in this dissertation, Murphy also completed data processing of the flux data. Appendix B documents the process of determining the

sensitivity of LiCor's EddyPro eddy covariance (EC) flux processing software results to gaps in the input datasets and a method for artificially filling these gaps in the most accurate way to represent missing data. These data were published as a dataset (Walden et al., 2017b) and in a publication (Walden et al., 2017a), in which Murphy is a co-author.

CHAPTER TWO

THE NORWEGIAN YOUNG SEA ICE FIELD CAMPAIGN

Earth system observations are an essential driver of progress in our understanding of climate change. Overall, capabilities to observe the physical climate system have continued to improve and expand. Improvements are particularly evident in ocean observing networks and remote-sensing systems.

- IPCC Sixth Assessment Report, August 2021

2.1 Introduction

The Norwegian Young Sea Ice field campaign (N-ICE2015 or N-ICE) was a 6-month field campaign conducted from January to July 2015, observing both atmospheric properties and sea ice dynamics. During this period, a Norwegian research vessel, the RV Lance, was frozen into the sea ice north of Svalbard and allowed to move with the ice floes. The ship tracks can be seen in Figure 2.1. Three times during the expedition the ice surrounding the ship broke up and the ship needed to be repositioned into the sea ice. The time it took for the ship to reposition can be seen as gaps in the data from 21 February, through 24 February, 15 March through 24 April, and again from 5 June through 7 June. The period in March and April corresponds with a trip back to Svalbard for resupply, explaining the long duration of the data gap. The dates of each ice floe are listed in Table 2.1.

This region is characterized by thin, first-year (or “young”) sea ice, as opposed to the thick, multi-year sea ice observed during SHEBA (Cohen et al., 2017). As a result, the N-ICE measurements are representative of the new regime that the polar

Table 2.1: Floe dates and approximate proximity to ice edge for the N-ICE field campaign.

| Floe | Start Date | End Date | Ice Edge Proximity | |
|------|------------------|------------------|--------------------|--------------|
| | | | Min Distance | Max Distance |
| 1 | 15 January 2015 | 21 February 2015 | 50 km | 175 km |
| 2 | 24 February 2015 | 19 March 2015 | 200 km | 325 km |
| 3 | 18 April 2015 | 5 June 2015 | 225 km | 40 km |
| 4 | 7 June 2015 | 21 June 2015 | 85 km | 10 km |

regions are moving toward as the climate warms. This expedition is of particular interest from a modeling perspective due to the magnitude of the temperature and pressure change during and after winter storm periods. This research cruise is the first to take seasonal measurements of the clouds and atmosphere since SHEBA in 1997 and 1998. These concurrent measurements of the energy budget and cloud properties

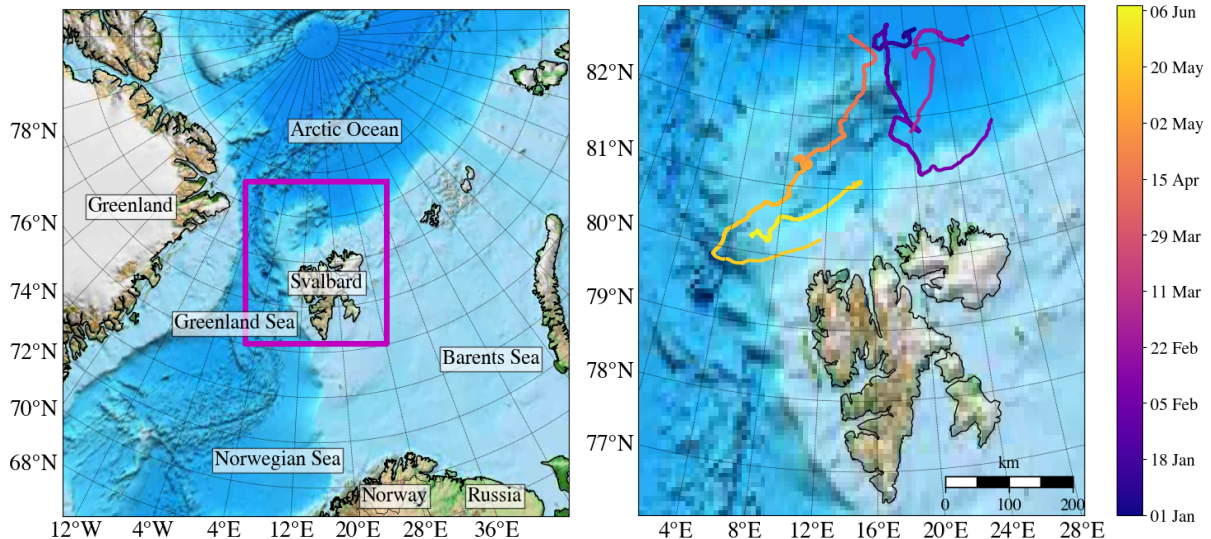


Figure 2.1: The location of the N-ICE field expedition. The right map shows a detailed view of the area indicated by the purple box on the left map. Ship location is plotted on the right figure and is colored by date.

(fraction, height, microphysical, and temperature) can give important insight into climate processes and radiative transfer (Persson, 2002; Schweiger, 2004).

Shupe & Intrieri (2004) observed mixed-phase clouds during SHEBA were consistent in temperature, liquid water path, and ice water content with previous studies over similar sea ice. NICE2015 observed more extreme storm periods than those seen at SHEBA, bringing wind speed, pressure, and temperature changes of previously unobserved magnitudes. In general, the winter during N-ICE was characterized by several significant storm periods (Cohen et al., 2017). These storms were associated with significant changes in surface temperature and humidity conditions, as well as changes in cloud properties. Springtime conditions during N-ICE were less stormy, with a gradual increase in surface temperatures and fairly constant thick cloud cover (Cohen et al., 2017).

Throughout much of N-ICE, strong temperature inversions were observed over the surface, similar to what was seen at SHEBA (Kayser et al., 2017). While these strong inversions are not unique to N-ICE2015, they are often underrepresented in Polar WRF simulations (Hines et al., 2015).

The primary objectives of N-ICE are:

1. To quantify the change in atmosphere-ice-ocean interactions as the atmosphere shifts from primarily multi-year sea ice to thin, first-year sea ice (Granskog et al., 2018, 2015).
2. To observe how changes in sea ice impact the marine ecosystem and their response (Granskog et al., 2015).
3. To provide key observations to tune and validate models (Granskog et al., 2018, 2015).

The overall conditions during the field campaign are described by Cohen et al. (2017), Kayser et al. (2017), and Walden et al. (2017a). More details about the experiment and the datasets that were collected can be found in Granskog et al. (2015). Itkin et al. (2017) describes the proximity to the sea ice edge throughout the experiment. During the majority of the experiment, the ship was stationed between 50 and 250 *km* from the ice edge during the first 3 floes. Approximate distances to the ice edge during each floe are listed in Table 2.1 (Oikkonen, 2017).

2.2 Instruments

A variety of instruments were deployed during the N-ICE campaign and provided data that will be used in this project, including radiosondes, a MicroPulse Lidar (MPL), a meteorological tower, an eddy covariance (EC) system, and broadband shortwave and longwave radiometers.

Vaisala RS92-SGP radiosondes were launched from the ice surface (Floe 1) or the ship deck (Floes 2, 3, and 4) twice daily around 1100 and 2300 UTC. The radiosondes recorded temperature, relative humidity, wind speed and direction, pressure, and geopotential height as high as 30 *km*. Data were recorded by the radiosondes every two seconds and were transmitted to the ground using a Vaisala MW31 ground station (Kayser et al., 2017; Cohen et al., 2017). More information and analysis of the radiosondes can be found in Kayser et al. (2017).

Data from the MPL were recorded every 14 seconds up to a height of 18 *km*. The MPL records backscattered light from clouds and operates at 532 *nm*. The range resolution is 15 m, with an 18 km maximum cloud base height. Distance uncertainties are $\pm 2\%$ due to timing uncertainties within the instrument. This instrument is more sensitive to water particles than ice, so some cloud types may be biased toward

higher percentages of water than ice within the cloud. The MPL is easily attenuated by optically thick clouds. In some instances when a low water cloud is detected, it is possible that more cloud layers exist above this layer that cannot be measured by the MPL.

A meteorological tower was deployed on the ice 300 to 400 *m* away from the ship. This tower was set up within a few days of anchoring to each new floe and recorded relative humidity and temperature (Vaisala HMP155), and wind speed and direction (Lufft Ventus V200A-UMB) at 2, 4, and 10 *m* heights. Pressure (RM Young 61302 V) was measured at 1.5 *m*. All measurements were collected by a Campbell Scientific CR30000 data logger at 1-second resolution. Periods of missing tower data were reconstructed using temperature and wind information from the ship (sensors mounted 22 to 24 *m* above the surface). More information about the meteorological measurements, temperature, and wind reconstruction using the ship data, a diagram of the meteorological tower setup, and a comparison of the meteorology to SHEBA can be found in Cohen et al. (2017).

Radiometers (Kipp and Zonen CMP22 and CGR4) were set up 1 to 1.2 *m* above the surface near the meteorological tower to measure upward and downward components of longwave and shortwave radiation. Kipp and Zonen CVF4 ventilation units were used to heat and ventilate the radiometers to avoid riming and frosting of the radiometer domes. More information about the radiometers and an analysis of the surface energy budget can be found in Walden et al. (2017a).

Turbulent flux data were collected by a closed path EC flux system (Campbell CPEC200) mostly at 20 *Hz* (but occasionally 10 *Hz*). This system contains a sonic anemometer and a closed-path, infrared gas analyzer. These instruments allow ob-

servation of the heat and moment exchanges and the water vapor and carbon dioxide mixing ratios, respectively. This system was set up next to the meteorological tower over a snow-covered surface. Further information about the EC Flux system can be found in Walden et al. (2017a).

2.3 Atmospheric components of the surface energy budget over young sea ice

Walden et al. (2017a) detailed the turbulent and radiative fluxes over thin sea ice during N-ICE. Snow albedo was around 0.85 in the winter and between 0.72 and 0.80 in the spring and summer. Stable stability was found in the winter, followed by unstable conditions in the spring, and approximately neutral stability in the summer (once the skin temperature reached $0^{\circ}C$). Latent and sensible heat flux values ranged between -10 to $+10\text{ W m}^{-2}$ and -100 to $+100\text{ W m}^{-2}$, respectively, in both the winter and spring. Shortwave radiation was not seen at the field site until March, at which time the sun rose and shortwave radiation increased until downward values reached almost 800 W m^{-2} mid-day near the end of the experiment. Downward longwave radiation ranged from 110 to 125 W m^{-2} during clear-sky times, and reached around 300 W m^{-2} under cloudy conditions. Positive values of net radiation and turbulent fluxes indicate flux into the surface.

Murphy's contribution to Walden et al. (2017a) was to solve several problems with the flux dataset collected during the N-ICE campaign and to process the data through the EddyPro software. The most restrictive data problem was the number of data gaps throughout 30-minute data files, which was caused by a programming error in the datalogger. In some cases, the amount of missing data made the file unable to be processed. To fix this, the data were filled by taking the section of data

before it (or after, in the case that the missing data was too close to the start of the dataset) and replicating it for the time period with no recorded data. To ensure that this method of data filling was acceptable, data from the Barrow, Alaska DOE ARM site (<https://www.arm.gov/capabilities/observatories/nsa>) was used to compare the post-processed data of a complete dataset with the post-processed results from the same dataset after (artificially added) gaps had been filled. Analysis of both the difference in sensible heat fluxes and the turbulent spectra from before and after the data filling were examined and determined the filling method appropriate for the type of gaps in the N-ICE data. Details of this gap-filling study were written as a report for a course on flux measurements. This report can be seen in Appendix B.

CHAPTER THREE

SIMULATION OF ATMOSPHERIC CONDITIONS OVER FIRST-YEAR SEA ICE USING THE POLAR WEATHER RESEARCH AND FORECASTING MODEL

The polar regions, notably the Arctic and maritime Antarctic, are experiencing impacts from climate change at magnitudes and rates that are among the highest in the world, and will become profoundly different in the near-term future (by 2050) under all warming scenarios (high confidence).

- IPCC Sixth Assessment Report, August 2021

3.1 Introduction

The Arctic has experienced large changes and dramatic loss in sea ice throughout the twenty-first century (Hines et al., 2015), signifying a transition in the Arctic from primarily thick, multi-year ice to thin, first-year sea ice. Increases in thin, first-year sea ice and open water have resulted in climate modeling errors not only in the polar regions but elsewhere on Earth (Hines et al., 2015; Royer et al., 1990; Francis et al., 2009).

The Polar Meteorology Group at the Ohio State University Byrd Polar Research Center developed a series of enhancements to the Weather Research and Forecasting Model (WRF). These modifications include enhanced mechanisms to allow prescribed sea ice thickness (default in non-polar WRF is 3 m), as well as sea ice fraction and snow depth (Hines et al., 2015). These mechanisms are primarily implemented as sea ice enhancements in the land surface model (Noah LSM), but also include

the heat transfer and thermal diffusivity through the snow and ice, albedo, snow density adjustments, and skin temperature calculations (Tastula et al., 2012; Hines et al., 2015). This model was developed as the successor to the Polar fifth-generation Mesoscale Model (MM5) with advanced physical parameterizations (Bromwich et al., 2009). It has been used extensively for weather forecasting in Antarctica (Powers et al., 2012) and has been tested over ice and land in the Arctic (Tastula et al., 2012; Bromwich et al., 2009).

In spite of Polar WRF being available for over 10 years, the model has only undergone limited testing in the Arctic with no testing over young thin sea ice. This chapter uses the data collected from a comprehensive suite of instruments deployed during the Norwegian Young Sea Ice field campaign in 2015 (N-ICE) to test and evaluate the performance of Polar WRF over young thin sea ice.

3.2 Observations and Model Setup

In this modeling study, observations from the N-ICE were used to evaluate the Polar WRF model. The model was run for a 6-month period (1 January 2015 to 1 July 2015) for selected combinations of planetary boundary layer (PBL) and cloud microphysics (CM) schemes; this time period overlapped with the entire N-ICE campaign. Three case study periods were selected for further analysis using idealized model runs using radiosonde soundings taken during N-ICE as input.

3.2.1 Observations

Details about the N-ICE field campaign can be found in Chapter 2. Most notable for the analysis presented here are the atmospheric radiation measurements, taken by Kipp and Zonen (CMP22 and CGR4) radiometers mounted 1 to 1.2 *m* above the

ground. Granskog et al. (2015) and Walden et al. (2017a) include a complete analysis of the radiative fluxes during N-ICE, which includes a description of how surface temperatures were calculated. Walden et al. (2017a) also showed that the radiative fluxes during N-ICE were primarily influenced by wind, advection, and cloud cover.

3.2.2 Model Setup

The WRF model version 4.1.4 was run with polar optimizations created by researchers at The Ohio State University. WRF with polar optimizations is often referred to as Polar WRF. WRF is a mesoscale weather model developed with both numerical weather prediction and research applications in mind. It is maintained by the NCAR’s Mesoscale and Microscale Meteorology Laboratory (MMM). As of 2021, WRF had over 57,800 registered users. The model allows users to select many options, such as domain size, temporal and spatial resolution, and input datasets (Skamarock et al., 2019).

A 2-way nested, two-domain (parent and nested domain) setup was used and can be seen in Figure 3.1. The nested domain (d02) used 3 km by 3 km grid cells, located just north of Svalbard and encompassing the entire spatial extent of the N-ICE field campaign. The larger domain, or the parent domain, used 9 km by 9 km grid cells.

The European Centre for Medium-Range Weather Forecasting’s Interim Re-Analysis (ERA-Interim) was used for boundary and initial conditions (Dee et al., 2011), Pan-Arctic Ice Ocean Modeling and Assimilation System (PIOMAS) was used for snow depth, ice thickness, and albedo (Zhang & Rothrock, 2003), and Special Sensor Microwave/Imager (SSMI) was input for ice extent information (DiGirolamo & Zwally., 2022; Schweiger, 2011). The initial conditions set the conditions at the start of the model as close to reality as possible. Boundary conditions bring synoptic-scale

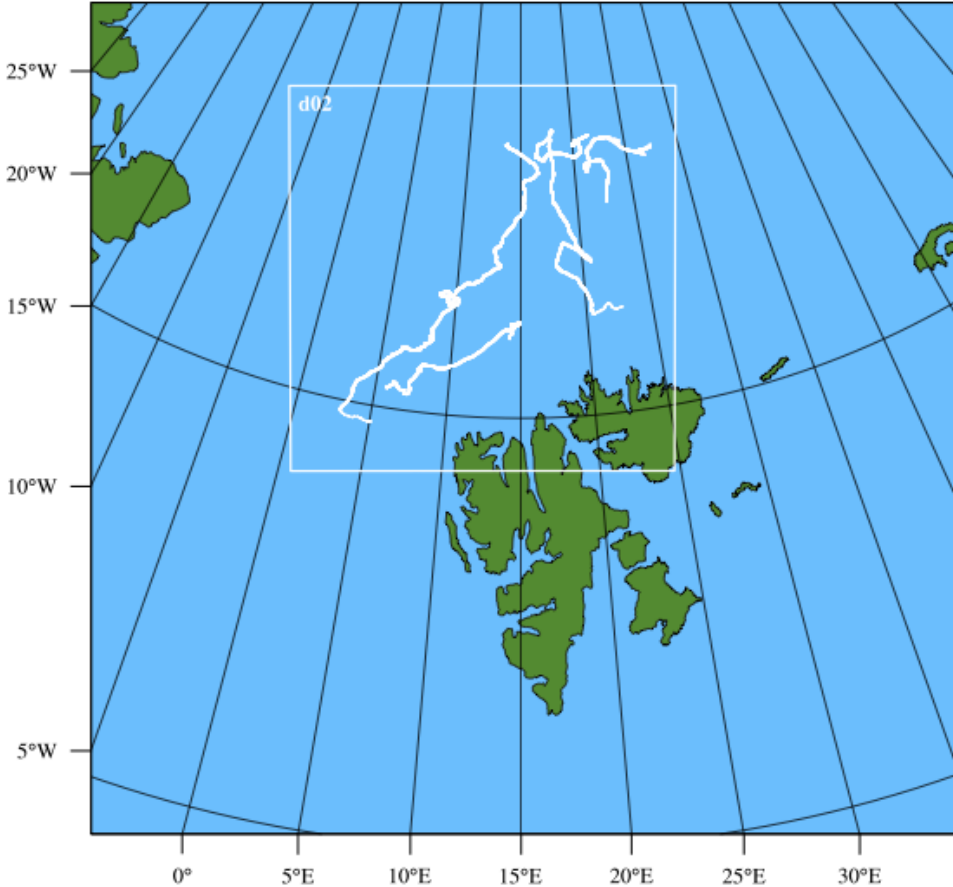


Figure 3.1: The WRF model domain (parent) with N-ICE domain (d02) in a 2-way nested configuration. The N-ICE ship tracks are in white.

weather systems into the model at the domain edges. Graham et al. (2017b) includes a comparison of the ERA-Interim dataset and the measurements taken during N-ICE. While Graham et al. (2017b) found that ERA-Interim accurately portrayed the cloudy and clear states, there were still issues with the cloud liquid water path being underestimated, which should be taken into consideration when looking at the WRF results. Large-scale synoptic systems, however, were simulated well, limiting the error possibly due to incorrect advection.

Table 3.1: Input datasets and settings used for all Polar WRF simulations. ETA Similarity surface layer scheme was only used in cases with the MYJ PBL scheme.

| Dates | |
|---|---------------------------------|
| Winter | 1 January - 1 April 2015 |
| Spring | 1 April - 1 July 2015 |
| Input Datasets | |
| Boundary and initial conditions | ERA-Interim |
| Snow depth, ice thickness, and ice extent | PIOMASS and SSMI |
| Polar WRF Settings | |
| LW and SW Radiation Scheme | RRTMG |
| Surface Layer Scheme | Revised MM5 or ETA Similarity |
| Land Surface | Unified Noah Land Surface Model |

The model was run for two periods: winter (January through March) and spring (April through June). Comparison with the N-ICE measurements for these periods start on 15 January and 18 April, resulting in 15+ days of spin-up time of the Polar WRF model before analysis. The simulations were completed using the Cheyenne supercomputer (Computational & Laboratory, 2019). More details about model settings are shown in Table 3.1.

In addition to the choice of input datasets and the underlying models used, one can select from a variety of different schemes to control different physical processes in the atmosphere and at the surface. This study focuses on the evaluation of different PBL and CM schemes because of their importance to Arctic conditions. The schemes used here were selected after a thorough literature review of previous WRF studies of both polar and non-polar applications. Various PBL schemes were selected to determine which of them most accurately represents the strong near-surface inversion

in the Arctic. Clouds also have strong radiative importance in the Arctic, so a variety of CM schemes were selected to determine which provide accurate representations of Arctic clouds, including the presence of mixed-phase (water and ice) and supercooled water clouds. All other schemes, with the exception of the surface layer scheme, were kept constant throughout all simulations. Table 3.2 shows all PBL and CM schemes chosen for this study and the abbreviations used to refer to each model run.

In addition to the PBL and CM schemes, a radiation scheme, surface layer scheme, and land surface model (LSM) must be selected. Unified Noah Land Surface Model (Noah LSM) was selected as the LSM. The Noah LSM has been tested and improved over polar regions, and its tuning is a key strength of Polar WRF (Mukul Tewari et al., 2004; Hines et al., 2015; Tewari et al., 2004). Further exploration of the Noah LSM can be found in Chapter 6. The Rapid Radiative Transfer Model (RRTMG) was selected to handle longwave and shortwave radiation (Mlawer et al., 1997) and the Revised MM5 surface layer scheme was used for all model simulations except those with the Mellor–Yamada–Janjic (MYJ) PBL scheme (Jiménez et al., 2012). The ETA Similarity surface layer scheme is required by the model to use the MYJ PBL scheme (Janić, 2001). Figure 3.2 is a flowchart showing the key physics schemes, variable exchanges, and relevant calculations in the model.

The most commonly used PBL schemes found in the literature were the Yonsei University (YSU) scheme (Hong et al., 2004) and MYJ scheme. The Mellor–Yamada Nakanishi Niino (MYNN) scheme (Olson et al., 2019) is a modified version of the MYJ scheme (Mesinger, 1993). The MYNN scheme has been tested over Svalbard, a location close to the N-ICE domain but with different surface conditions (Pilgug et al., 2018). Development of the MYNN scheme focused on large eddy diffusion

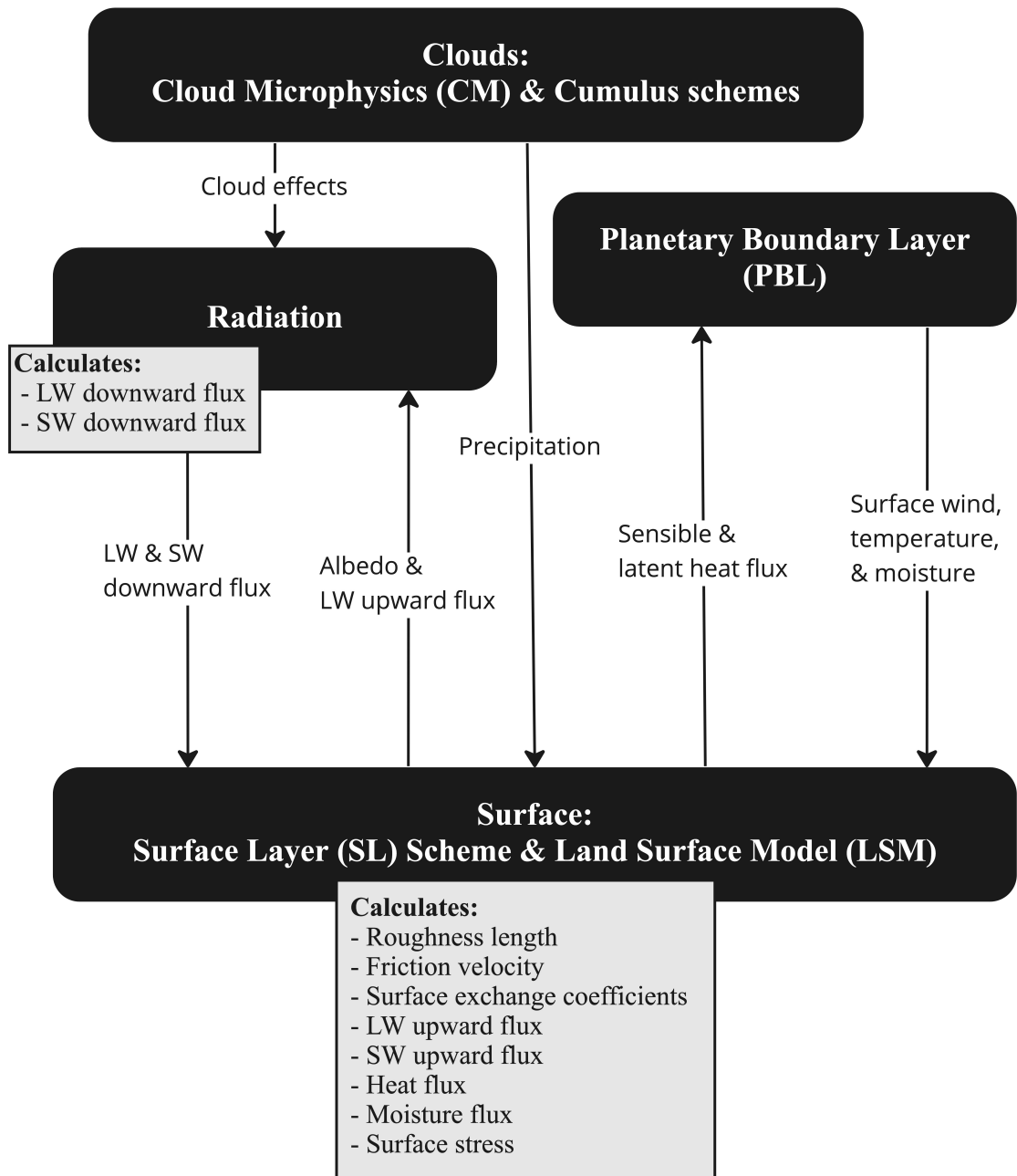


Figure 3.2: The relevant WRF model physics schemes, variables exchanges, and calculations used in this study.

Table 3.2: Cloud microphysical (CM) and planetary boundary layer (PBL) schemes used for Polar WRF model simulations with corresponding abbreviations used to refer to each model run.

| | | CM Schemes | | | |
|-------------|------|------------|-------------|--------------------|-------------------|
| | | Goddard | WRF 5-Class | Predicted Particle | Morrison 2-Moment |
| PBL Schemes | YSU | G-YSU | | P3-YSU | |
| | MYJ | G-MYJ | 5-MYJ | P3-MYJ | 2-MYJ |
| | MYNN | G-MYNN | 5-MYNN | | 2-MYNN |

(Cohen et al., 2015), while the MYJ scheme is focused more on stable flows (Janjic, 1994; Mellor & Yamada, 1982). MYJ is a 1.5-order closure scheme and MYNN is a 2nd-order closure scheme (Pilguy et al., 2018). Higher order closure indicates that fewer assumptions are made in calculating turbulence. Closure in modeling turbulent fluxes is an issue that arises in Monin-Obukhov similarity theory due to need for estimations in the equations to calculate the fluxes. A higher-order closure will give more accurate results at a higher computational expense.

The Goddard (G) scheme (Tao et al., 1989) and WRF Single-Moment 5-Class (5) scheme (Hong et al., 2004) are the two most commonly used CM schemes found from the literature search regardless of the location being modeled. The Predicted Particle Properties (P3) scheme is a newly released scheme with advancements to the Morrison Two-Moment (2) scheme (Milbrandt & Morrison, 2016; Morrison & Milbrandt, 2015). This scheme was not designed for the polar regions but is of particular interest due to the way it parameterizes ice particle density. Many CM schemes use bins to classify different cold cloud particle sizes and densities, leading to assumptions that can potentially lead to large errors. The P3 scheme eliminates the conversion between categories by using one set of parameters that evolve throughout

the lifecycle of the cloud particles. This reduces the simplifications often made when using the binning approach for ice particles (Morrison et al., 2005). However, this scheme has a particle size cutoff, eliminating smaller particles, which may prove to be problematic in the dry polar regions.

3.3 Results

Atmospheric conditions at the grid cell containing the ship were selected from the model output. Time series of the pressure, temperature, sensible and latent heat fluxes, components of longwave and shortwave flux, and cloud fraction in the model grid cell at the ship location can be seen in Figure 3.3. While it is difficult to see fine details in these panels, the P3-YSU scheme stands out during both the winter and spring, with particularly low values of temperature, upward longwave flux, and downward longwave flux. Additionally, cloud fraction values are greatly varied between model runs, and are often not in agreement with the observations. Further analysis of each variable is included in the following subsections.

The sea level pressure, shown in the top panel of Figure 3.3, shows several pressure drops in the winter associated with storms passing over the area. Many of the model simulations predict the pressure patterns fairly accurately. The first period of low pressure, from 3 February to 8 February, was a strong storm (Cohen et al., 2017) that the model accurately predicted the onset of, but no simulations correctly predicted how long the storm persisted over the area. Other than the end of this storm period, the modeled pressure compares well with the measurements. In the spring and summer, the simulations accurately predict the pressure although strong synoptic-scale storms are less frequent. This suggests that model simulates the large-scale synoptic pressure patterns well during these seasons.

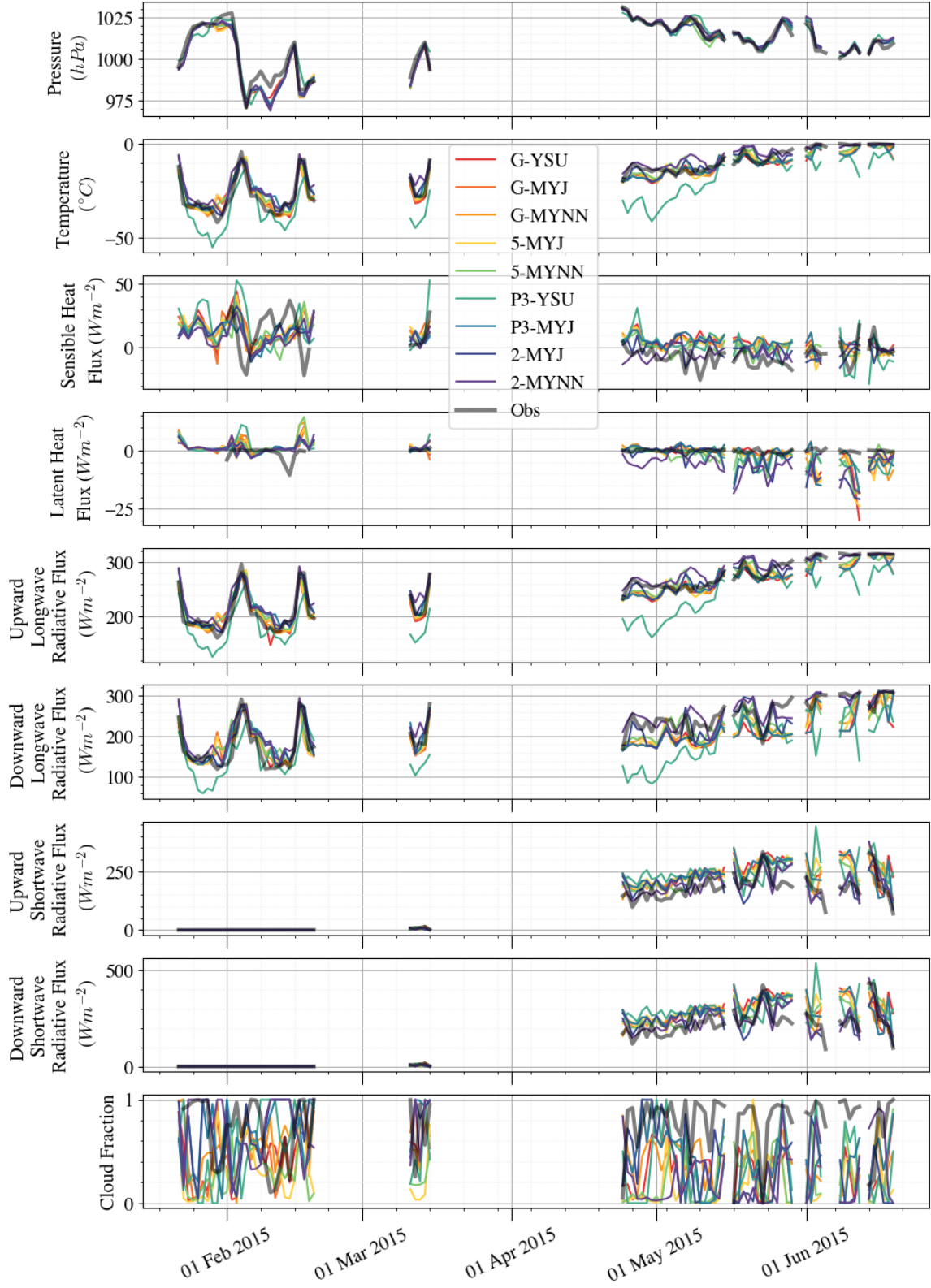


Figure 3.3: Daily averages of pressure (top), temperature (second from top) sensible heat flux (third), latent heat flux (fourth), upward and downward longwave flux (fifth and sixth), upward and downward shortwave flux (seventh and eighth), and cloud fraction (bottom). Measurements are shown in black and each model simulation is a different color, identified by the abbreviations defined in Table 3.2.

Eq. 3.1 was used to calculate mean model biases from the time series for skin temperature (K), latent heat flux (Wm^{-2}), sensible heat flux (Wm^{-2}), net longwave flux (Q_{sw} , Wm^{-2} , Eq. 3.2), and net shortwave flux (Q_{sw} , Wm^{-2} , Eq. 3.3) and are shown in Table 3.3 for winter (top) and spring (bottom). In this equation, y_{mod} is the modeled value and y_{obs} is the observed value.

$$Mean\ bias = \frac{1}{n} \sum_{i=1}^n (y_{mod} - y_{obs}) \quad (3.1)$$

$$Q_{lw} = Q_{lw\downarrow} - Q_{lw\uparrow} \quad (3.2)$$

$$Q_{sw} = Q_{sw\downarrow} - Q_{sw\uparrow} \quad (3.3)$$

Bias values were only calculated for times when measurements were available. Negative (positive) model biases indicate the model is producing values lower (higher) than those observed. The mean bias was selected as a way to determine model accuracy as it allows for a quick summary of how much the modeled time series disagrees with the measured values, although it can hide compensating biases at different times or under different conditions. The primary goal of this study is to determine which schemes perform well and which combinations of schemes give unreasonable values.

3.3.1 Skin Temperature

G-MYJ had the smallest mean temperature bias in winter. For spring, 2-MYJ had the smallest model bias. Figure 3.4 shows the distribution of skin temperature from each model run with the measurements shown in black. P3-YSU has colder temper-

Table 3.3: Mean model bias (left) and mean model flux (right, in parentheses) for temperature (K), latent heat flux (Wm^{-2}), sensible heat flux (Wm^{-2}), net longwave flux (Net LW) (Wm^{-2}), and net shortwave flux (Net SW) (Wm^{-2}). Acronyms in the left-hand column represent the CM and PBL schemes and are defined in Table 3.2. Rows are ordered by CM scheme and colored by PBL scheme for ease of use.

| | Winter | | | | |
|---------------|--------------|-------------|---------------|---------------|-------------|
| | Temperature | Latent Heat | Sensible Heat | Net LW | Net SW |
| G-YSU | 0.3 (-24.7) | 2.5 (1.7) | 4.1 (13.7) | 2.9 (-26.8) | |
| G-MYJ | -0.1 (-25.1) | 1.9 (1.1) | 3.4 (13.0) | 4.4 (-25.3) | |
| G-MYNN | 0.2 (-24.8) | 2.8 (2.1) | 1.8 (11.4) | 5.1 (-24.5) | |
| 5-MYJ | 0.7 (-24.3) | 2.3 (1.6) | 3.7 (13.4) | 3.4 (-26.3) | |
| 5-MYNN | 2.0 (-23.0) | 2.7 (2.0) | -0.8 (8.9) | 8.5 (-21.2) | |
| P3-YSU | -7.5 (-32.5) | 2.6 (1.8) | 5.8 (15.4) | -2.5 (-32.2) | |
| P3-MYJ | 3.1 (-21.9) | 1.1 (0.4) | -2.0 (7.6) | 12.9 (-16.8) | |
| 2-MYJ | 2.2 (-22.8) | 1.6 (0.8) | -0.9 (8.7) | 10.2 (-19.5) | |
| 2-MYNN | 4.5 (-20.5) | 1.5 (0.7) | -2.1 (7.5) | 12.0 (-17.7) | |
| | Spring | | | | |
| | Temperature | Latent Heat | Sensible Heat | Net LW | Net SW |
| G-YSU | -2.6 (-10.7) | -1.7 (-2.0) | 11.3 (4.1) | -34.7 (-57.4) | 10.7 (54.4) |
| G-MYJ | -2.4 (-10.5) | -1.3 (-1.6) | 11.5 (4.4) | -33.7 (-56.3) | 9.2 (52.9) |
| G-MYNN | -1.7 (-9.9) | -2.1 (-2.5) | 9.4 (2.2) | -28.5 (-51.2) | 7.8 (51.5) |
| 5-MYJ | -1.9 (-10.0) | -2.1 (-2.5) | 9.3 (2.2) | -30.3 (-53.0) | 10.6 (54.3) |
| 5-MYNN | -0.6 (-8.7) | -2.8 (-3.1) | 6.9 (-0.3) | -22.5 (-45.2) | 6.4 (50.1) |
| P3-YSU | -9.2 (-17.3) | -2.8 (-3.1) | 6.8 (-0.3) | -32.4 (-55.0) | 10.0 (53.7) |
| P3-MYJ | -2.4 (-10.5) | -1.3 (-1.6) | 11.5 (4.4) | -33.7 (-56.3) | 9.2 (52.9) |
| 2-MYJ | -0.1 (-8.1) | -4.4 (-4.8) | 5.5 (-1.6) | -14.0 (-36.6) | 1.4 (45.1) |
| 2-MYNN | 2.1 (-6.0) | -5.8 (-6.1) | 3.4 (-3.8) | -5.0 (-27.6) | -0.4 (43.2) |

Table 3.4: Mean model absolute error for temperature (K), latent heat flux (Wm^{-2}), sensible heat flux (Wm^{-2}), net longwave flux (Net LW) (Wm^{-2}), and net shortwave flux (Net SW) (Wm^{-2}). Acronyms in the left-hand column represent the CM and PBL schemes and are defined in Table 3.2. Rows are ordered by CM scheme and colored by PBL scheme for ease of use.

| | Winter | | | | |
|--------|-------------|-------------|---------------|--------|--------|
| | Temperature | Latent Heat | Sensible Heat | Net LW | Net SW |
| G-YSU | 4.4 | 3.7 | 17.6 | 15.9 | |
| G-MYJ | 4.3 | 3.7 | 18.1 | 16.6 | |
| G-MYNN | 4.3 | 3.5 | 16.4 | 17.5 | |
| 5-MYJ | 4.3 | 3.6 | 17.7 | 15.8 | |
| 5-MYNN | 5.0 | 3.6 | 18.3 | 19.8 | |
| P3-YSU | 10.3 | 3.2 | 19.3 | 22.2 | |
| P3-MYJ | 4.8 | 3.2 | 16.2 | 17.1 | |
| 2-MYJ | 4.5 | 3.0 | 15.9 | 16.8 | |
| 2-MYNN | 5.9 | 3.1 | 15.8 | 17.7 | |
| | Spring | | | | |
| | Temperature | Latent Heat | Sensible Heat | Net LW | Net SW |
| G-YSU | 3.4 | 3.7 | 13.3 | 37.4 | 20.6 |
| G-MYJ | 3.3 | 3.6 | 13.8 | 37.3 | 21.1 |
| G-MYNN | 2.9 | 4.1 | 11.9 | 33.8 | 20.7 |
| 5-MYJ | 2.8 | 3.9 | 13.0 | 34.6 | 18.7 |
| 5-MYNN | 3.1 | 4.3 | 10.8 | 28.4 | 16.9 |
| P3-YSU | 9.5 | 3.6 | 12.9 | 37.2 | 20.3 |
| P3-MYJ | 3.3 | 3.6 | 13.8 | 37.3 | 21.1 |
| 2-MYJ | 2.6 | 5.6 | 10.9 | 22.1 | 17.5 |
| 2-MYNN | 2.9 | 6.4 | 8.7 | 18.1 | 15.0 |

atures than the measurements and all model runs throughout the entire experiment and, as a result, has the largest biases in skin temperature in both seasons.

Some of these disagreements between the model and measurements can be attributed to inaccurate surface albedo and a lack of cloudiness. The model simulated the surface albedo to be around 0.2 less than the measured surface albedo for the entire campaign (0.6 compared to 0.8 measured at N-ICE). This is likely due to the default albedo of the model being set too low. The model surface temperature reaches the freezing point earlier than the observations. The transition season is when the model had the most difficulty in simulating the skin temperature, but in the summer, when the temperature reaches freezing, all of the model simulations agree well with

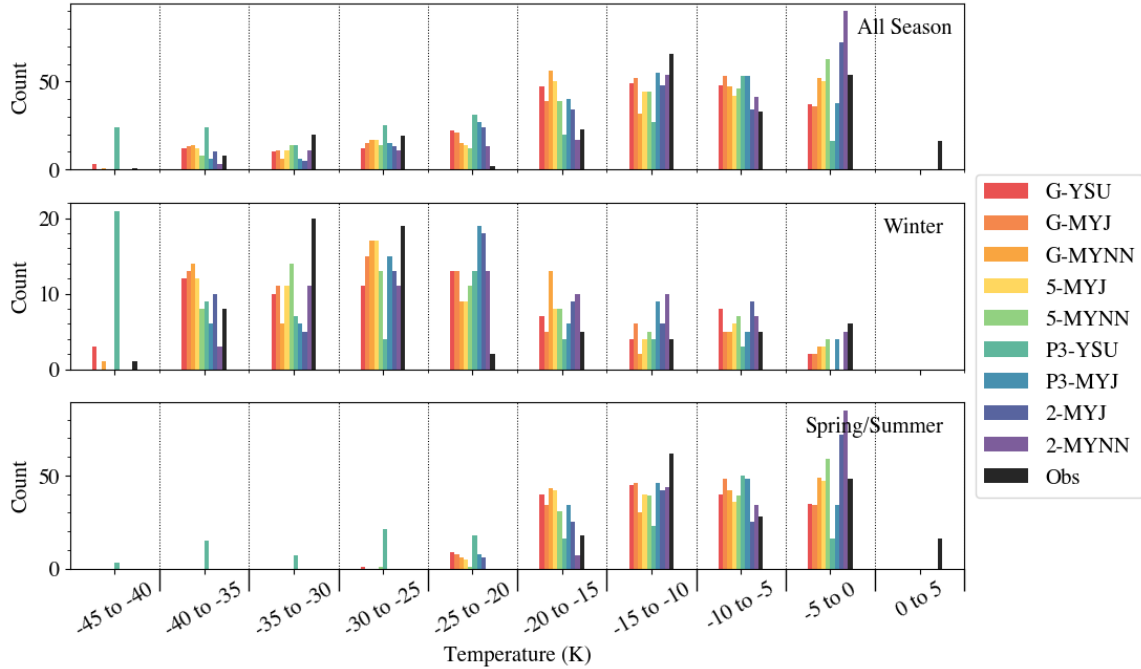


Figure 3.4: Temperature for the entire observational period (top), winter (middle), and spring/summer (bottom) for each of the Polar WRF runs. Measurements are shown in black and each model simulation is a different color, identified by the abbreviations defined in Table 3.2.

the observations.

3.3.2 Longwave and Shortwave Fluxes

In the winter, P3-YSU had the lowest bias in longwave flux. All other model simulations produced a positive bias in the winter. This suggests that the low bias in longwave flux is likely due to the strong negative temperature bias compensating for the overestimation of longwave flux occurring within the model. These fluxes often have compensating errors, too, as the bias in the upward component could compensate for a bias in the downward component. The P3-YSU net longwave bias in the winter is an example of this. The mean bias (Table 3.3) is quite low, with an overall bias of -2.5 Wm^{-2} . However, the mean absolute error (Table 3.4) is the largest of any simulations, indicating that there is a compensating underestimation in the components of longwave flux. This can also be seen in the time series in Figure 3.3 panels 5 and 6, when the P3-YSU scheme clearly underestimates both the upward and downward components of longwave radiation.

In winter, the distributions shown in Figure 3.5 show two peaks in the observations (black bars). One peak shows a maximum between -60 and -40 Wm^{-2} and corresponds to clear sky conditions. These conditions are most accurately modeled by G-YSU. This is further corroborated by the low biases seen in Table 3.3 and low mean absolute error in Table 3.4. A second peak occurs around -10 Wm^{-2} and is related to cloudy conditions, which is most accurately captured by 5-MYJ. Overall, the lowest net longwave biases were seen with the G-YSU and P3-YSU simulations, indicating that the YSU boundary layer scheme is producing the best surface-layer temperature structure during the winter at N-ICE.

Spring and summer longwave flux values were more largely negative in all model

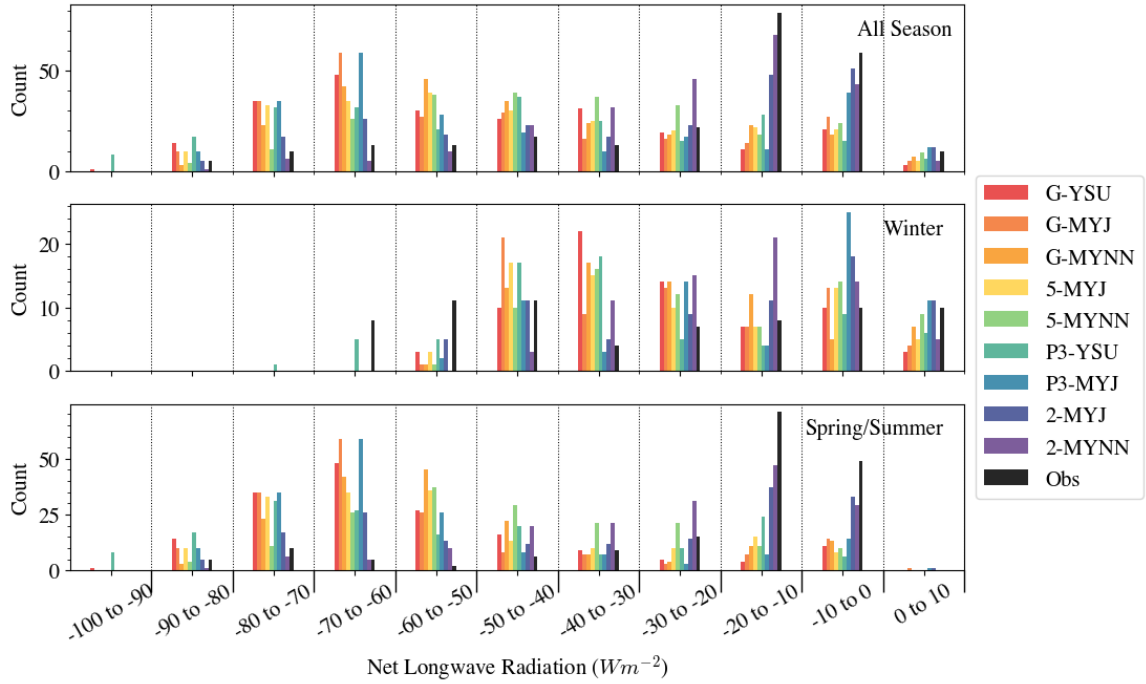


Figure 3.5: Net longwave flux at the surface for the entire observational period (top), winter (middle), and spring/summer (bottom) for each of the Polar WRF runs. Measurements are shown in black and each model simulation is a different color, identified by the abbreviations defined in Table 3.2.

runs compared to the measurements. This indicates that the surface was losing more longwave flux than it was gaining, which is likely due to clouds in the models being either too cold or thin to produce the downward longwave flux required to balance out the amount of longwave being lost from the surface. In the spring, the downward longwave is clearly dominated by the CM schemes, as the schemes show vastly different results. The WRF 2-Moment CM scheme has the lowest net longwave biases in the spring by almost 20 Wm^{-2} in some cases (Table 3.3). The 2-MYNN scheme has the lowest mean net longwave bias for spring, which indicates that this scheme may be producing clouds closest to what was actually observed. While the

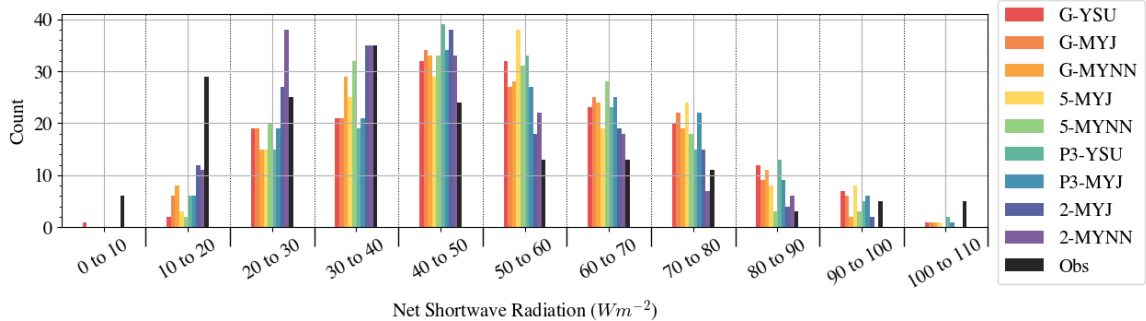


Figure 3.6: Net shortwave flux at the surface for the entire observational period (top), winter (middle), and spring (bottom) for each of the Polar WRF runs. Measurements are shown in black and each model simulation is a different color, identified by the abbreviations defined in Table 3.2.

2-MYNN does well with the spring and summer net longwave flux, this simulation had the largest biases in the net shortwave flux, which indicates that there may be some compensating errors in the turbulent fluxes.

Net shortwave flux (Figure 3.6) is only shown and calculated for spring and summer. The N-ICE location experienced 24-hour darkness in the winter until the sun rose in early March, at which time the hours of daylight increased until late April, when the field site experienced 24 hours of sunlight (Walden et al., 2017a). The net shortwave flux is slightly larger in the model runs than in the measurements. The distributions from the model runs peak between 40 and 60 Wm^{-2} . These values are 10 to 20 Wm^{-2} higher than the measurements, with the peak of the distributions correlating with the CM scheme used.

The observations display two peaks. A second peak, which is not well replicated in the model distributions, can be seen in the measurements between 10 and 20 Wm^{-2} . This is likely a result of the low modeled albedo. The low sun angle, in combination with high early spring albedo, could result in these low net SW values. Shortwave flux

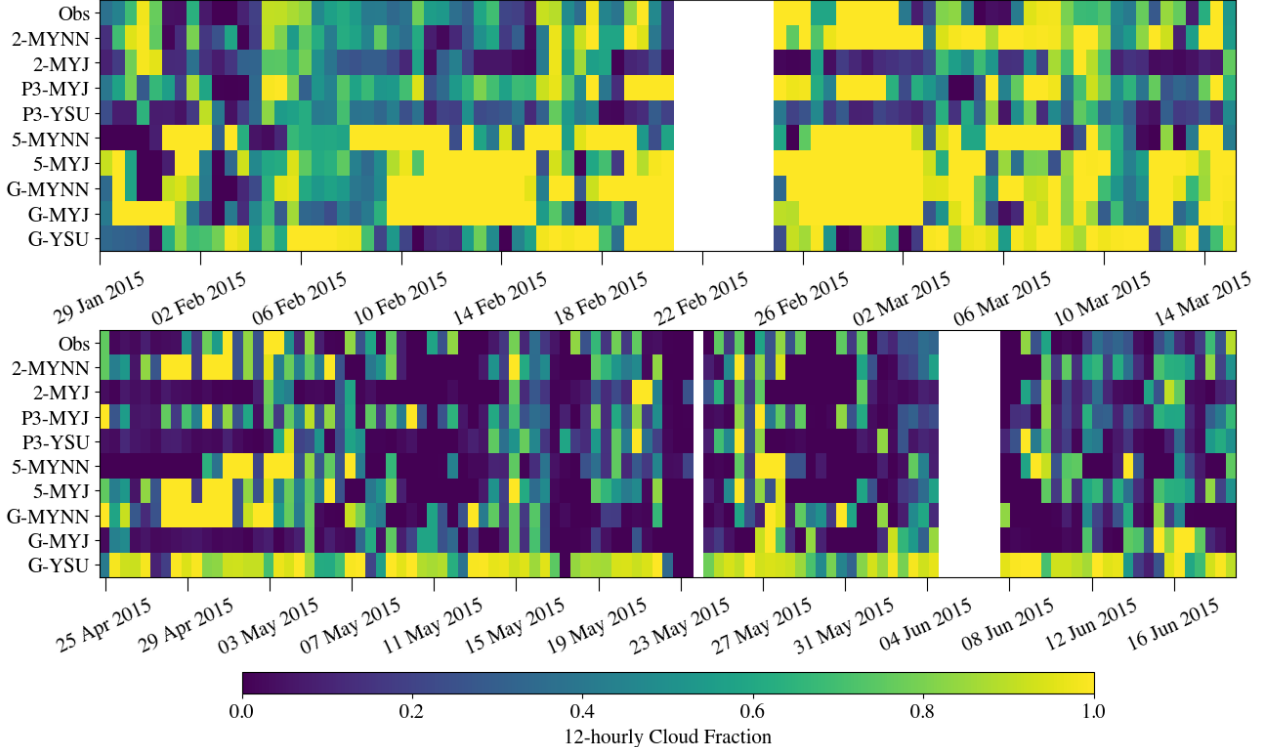


Figure 3.7: Cloud fraction from each Polar WRF run and the measurements in winter (top) and spring (bottom). Cloud cover is indicated by color, with yellows representing more cloud cover and purples less. Dark purple represents no cloud cover. Areas of white indicate no measurements. Polar WRF simulations are indicated on the left side of the figure by acronyms defined in Table 3.2 and observations represent what actually observed at N-ICE.

was best represented in the G-MYJ and P3-MYJ schemes. These simulations also had the largest net longwave biases, so errors in the shortwave (and the sensible and latent heat fluxes) are compensating for the earth's radiation balance and are attempting to compensate for errors in other variables. Additionally, upward shortwave flux was hindered by an unreasonably low surface albedo in all model simulations.

Cloud cover was consistently present, particularly in spring and summer. However, the radiative fluxes in the model show that either the cloud fraction was not large

enough or the clouds were not optically thick enough in any of the simulations. Figure 3.7 shows the 12-hourly average cloud fraction in the grid cell corresponding to the ship location for each model run. The row labeled “Obs” (bottom) on each panel is a 12-hourly vertical cloud fraction. This represents the frequency of occurrence of clouds in the entire column. While these are different metrics of calculating cloud fraction, they can give valuable insight into what the cloud cover was each day. For example, in the spring, at least 75% cloud cover was present almost the entire time with only one day (23 May 2015) classified as “clear sky.” This day can be seen by a blue stripe in Figure 3.7. Figure 3.7 also shows that the cloud cover was less consistent in winter.

One period of extended clear sky in the winter (9 February to 12 February) was captured best by model runs using the Goddard and WRF Single-Moment 5-Class CM schemes, with little apparent correlation to PBL scheme. The third major storm period at N-ICE (M3, 15 February to 21 February), which occurred from 15 February to 21 February, can be seen in the measurements as a period of 100% cloud fraction almost the entire storm period. None of the simulations capture the high cloud fraction at the beginning of this storm period, but near the end of the storm period simulations using the P3 scheme and the Morrison 2-Moment scheme captured the cloudiness. Later in the winter, however, the M4 storm (2 March to 4 March) is captured in its entirety quite well by both the P3 scheme and Morrison 2-Moment.

The WRF simulations during spring show a significant underestimation of cloud cover (Figure 3.7, bottom panel). The single clear day observed at N-ICE (23 May) was simulated by all of the model runs. However, this is not surprising because all of the simulations produced low cloud fractions throughout the entire spring. This

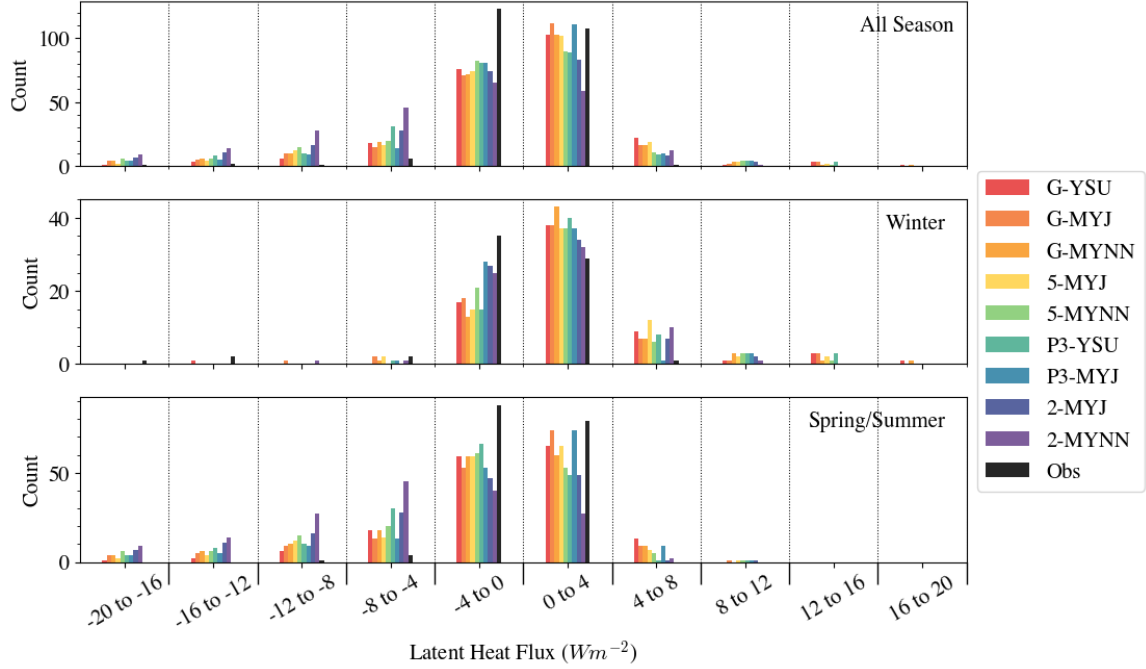


Figure 3.8: Latent heat flux for the entire observational period (top), winter (middle), and spring (bottom) for each of the Polar WRF runs. Measurements are shown in black and each model simulation is a different color, identified by the abbreviations defined in Table 3.2.

agrees with results seen by Hines et al. (2011) over Arctic land. Hines et al. (2011) showed that there were significant model uncertainties in spring and that simulations did not accurately represent cloudy conditions measured in the Arctic.

3.3.3 Turbulent Fluxes

Figures 3.8 and 3.9 show the latent and sensible heat flux, respectively. The magnitudes of the latent heat flux measurements were close to zero throughout the entire period (Walden et al., 2017a), but modeled values ranged from -20 to $+20 \text{ Wm}^{-2}$. All model simulations produced inaccurate latent heat flux values as they all calculated a much larger range of values about 0 Wm^{-2} . This indicates more phase change was

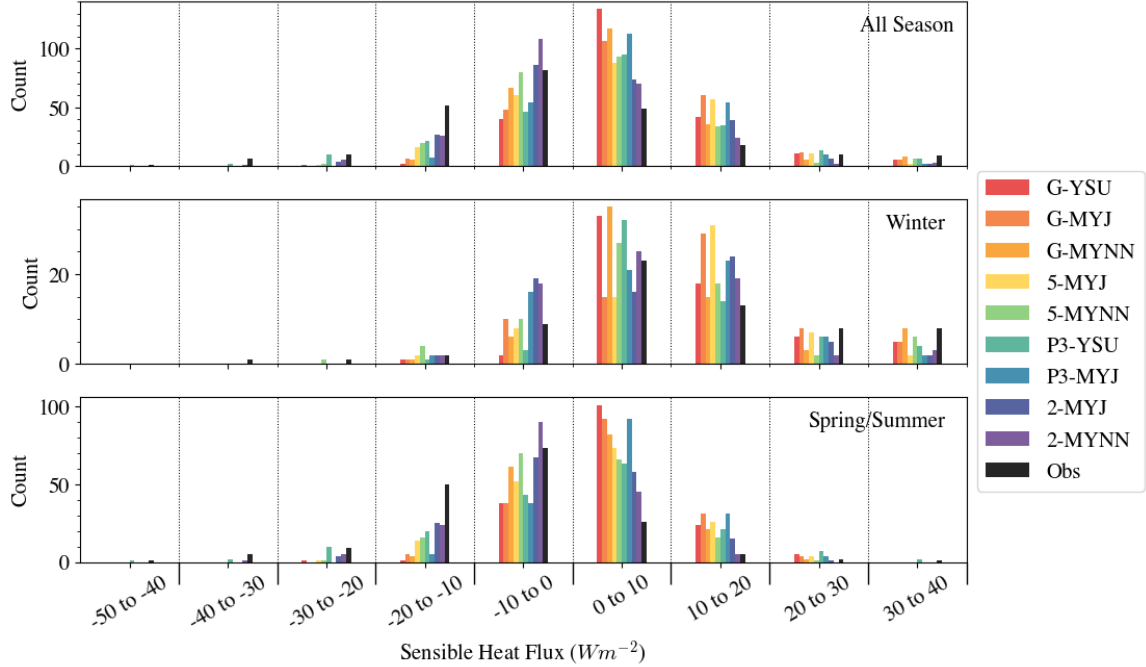


Figure 3.9: Sensible heat flux for the entire observational period (top), winter (middle), and spring (bottom) for each of the Polar WRF runs. Measurements are shown in black and each model simulation is a different color, identified by the abbreviations defined in Table 3.2.

occurring in the simulations than was actually observed. The wide range of values in the model compared to the measurements indicates this model is producing more deposition/sublimation and freezing/melting than is actually occurring.

In the spring, the calculations of the latent heat flux were similar in all the model simulations but varied more largely than the measurements. The measurements peaked at zero with limited spread, slightly favoring the negative values (melting, sublimation, or evaporation). All the model simulations, however, overestimated the amount of melting/sublimation/evaporation that was occurring by overestimating the amount of negative latent heat flux.

While there is the possibility of measurement error, the large disagreement in

latent heat flux values may be a result of the model's inability to resolve sub-grid level surface heterogeneities. The land surface type at the ship location was always sea ice, but this does not account for the potential of open leads on smaller scales close to the ship. These open leads could be a moisture source that increases water vapor advecting over the ship location that is not resolved in the model, reducing the ability for latent heat exchange. The impact of the sub-grid surface heterogeneity is an important topic for further study and a potential source of error in the modeled turbulent fluxes and surface albedo.

In the winter, the calculation of sensible heat flux is incorrect in all of the model simulations and is most influenced by the PBL scheme. The YSU PBL scheme shows a peak between 0 and 10 Wm^{-2} , but a smaller spread than the measurements, indicating that this scheme is not accurately representing the near-surface temperature structure. The MYJ PBL scheme, however, has the opposite problem, with a larger range of values. Neither scheme accurately represents the distribution of the measurements, which is less steep at positive flux values. The runs using the MYNN PBL scheme had the lowest flux bias values.

The sensible heat fluxes in spring peak just below 0 Wm^{-2} in the measurements, but were slightly positive in the model simulations, indicating that the model predicted the atmosphere was warmer than the surface and flux was going into the surface. The MYJ PBL scheme predicted a small secondary peak slightly negative that was also captured in the measurements, but the shape, value, and magnitude of this peak were incorrectly simulated by the model. The sensible heat flux calculations by the MYJ PBL scheme compare well to the measurements; the MYNN PBL scheme performs worse. The measurements and the 2-MYNN simulation both show a large

spread with slightly more negative sensible heat fluxes than the other simulations. This indicates that there is a greater flux out of the surface in the 2-MYNN scheme and in the measurements, as the surface temperature is less than the air temperature.

3.3.4 Case Studies

Cohen et al. (2015) described synoptic events (major and minor storms) during N-ICE that caused short-term changes in the local weather conditions. A winter and a spring case study are described below to determine how well the WRF simulations were able to capture these short-term events.

Case 1 - A Winter Cold Frontal Passage, 5 February 2015

A cold front passed through the ship location just after midnight on 5 February, bringing a temperature drop of approximately 25°C . Cohen et al. (2017) indicated this was during the second major storm that passed over the ship during the observation period. This storm also brought the most snowfall observed during the winter (Cohen et al., 2017). The model simulations do not accurately capture the timing or magnitude of the temperature change associated with the cold front. The pressure, however, in many of the model simulations indicates that the synoptic setup was modeled accurately. All simulations, with the exception of the P3-YSU, produced accurate sea level pressure in the days 24-hours leading up to the temperature drop (Figure 3.10, top panel), indicating the larger-scale storm system is moving into the area at the right time, but the fluxes and surface temperature are lagged behind the observations.

Prior to the frontal passage, observed temperatures were warmer than those forecasted by WRF (top panel, Figure 3.10). Additionally, after the front passes, the

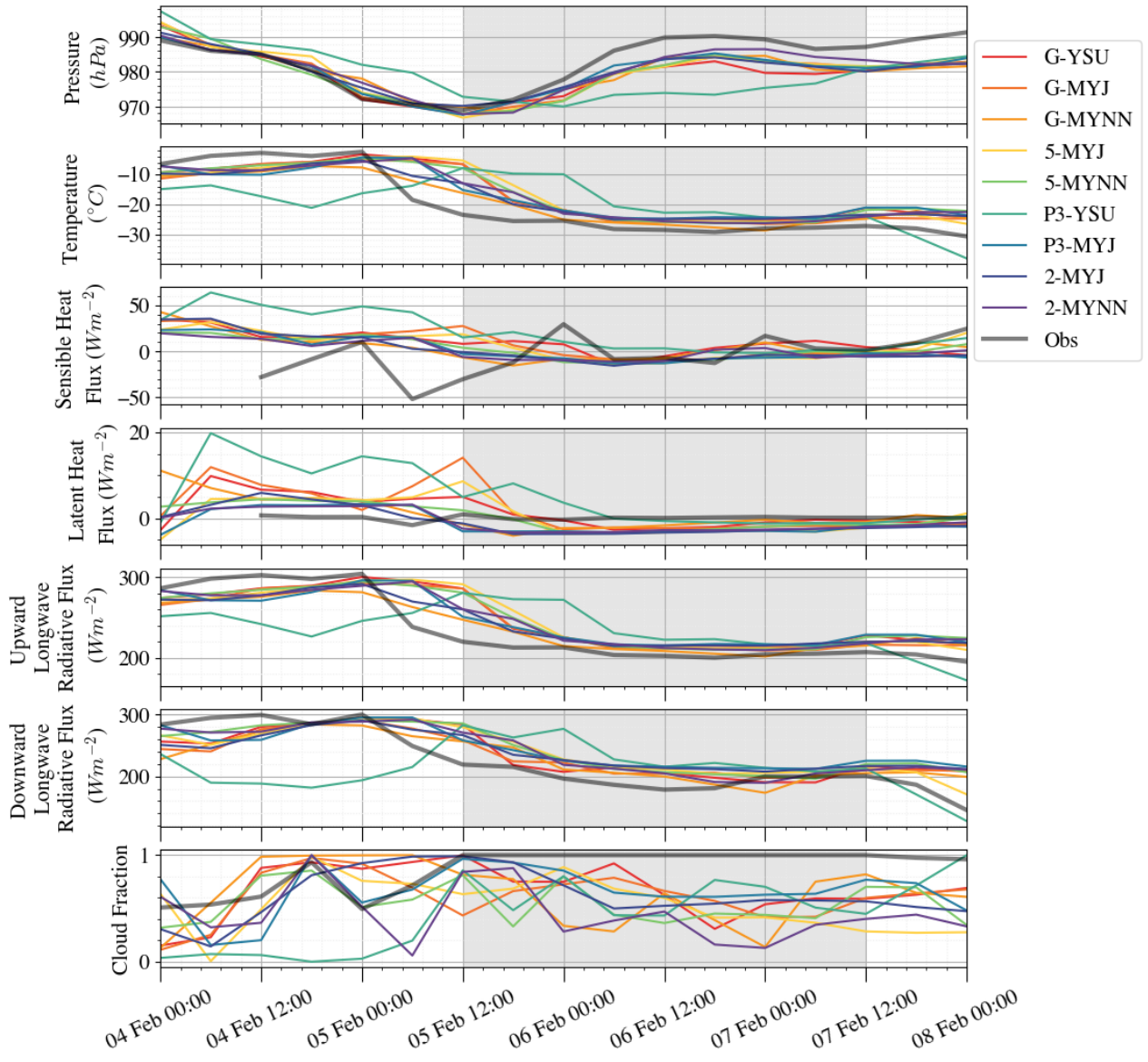


Figure 3.10: 6-hourly values of WRF modeled output (rainbow, acronyms in legend defined in Table 3.2) and observations (black) for sea level pressure, temperature, sensible heat flux, latent heat flux, downward longwave flux, upward longwave flux, and cloud fraction during the cold-frontal passage from 4 Feb to 8 Feb 2015.

modeled temperature is, at times, around $10^{\circ}C$ higher than the measured temperature. This can also be seen in both components of the longwave flux (Figure 3.10, 5th and 6th panel from the top). P3-YSU performed particularly poorly during this period; this run had the lowest pre-frontal temperature and took the longest time for temperatures to fall after the passage of the front. Walden et al. (2017a) showed the precipitable water vapor in Figure 11 panel c. Precipitable water vapor reaches a peak during the passage of the cold front, coinciding with the sharp decrease in temperature, and drops shortly after. The delayed longwave flux and temperature response in the model might be due to an inaccuracy in the amount of water vapor within the column. The decrease in precipitable water vapor was likely delayed, resulting in this delayed response in temperature, latent heat flux, and components of longwave radiation.

A possible explanation for the P3-YSU scheme performing so poorly with temperature and longwave flux is the lack of cloud cover before the front. This scheme consistently produced close to zero cloud cover ahead of the front. While the observations did not see complete cloud cover until just after the front passage on 5 February at 12:00 (indicated by gray shading in Figure 3.10), the ship still experienced some cloud cover, at times approaching 100% over the six-hour averaging period. The P3-YSU scheme did not produce any cloud cover ahead of the front, and cloud cover reduced quickly after the frontal passage, which was not seen in the measurements.

During the first half of this case, the sensible heat flux values in the measurements were negative, indicating that the surface was warmer than the atmosphere. The model, however, produced positive sensible heat flux values during this time for all combinations of PBL and CM schemes. Latent heat flux is also largely positive in

the model simulations during this time, while the observations consistently observed latent heat flux values near zero.

The two simulations using the Morrison 2-Moment CM scheme performed the best in this case. These simulations consistently had cloud cover that compared well to the measurements during the first half of this case. They also performed the best for each of the other variables shown in Figure 3.10 throughout the entire case study regardless of the reduction in cloud fraction each experienced during the second half of the case. The ability of the model to simulate the fluxes, in this case, seems to depend on how well the simulations can reproduce the cloud fraction.

Case 2 - A Spring Clear-Sky Day, 23 May 2015

Clouds occurred nearly continuously during the spring at N-ICE, however, the only 24-hour period of clear skies occurred on 23 May. Observations and WRF output variables during this time period can be seen in Figure 3.11. In contrast to the winter cold-front case, the Morrison 2-Moment schemes seem to be performing worse than the other schemes during this case study. Temperatures in the simulations using the Morrison 2-Moment scheme were higher than the other simulations, with temperatures almost 20°C above the observations during the 10 hours of clouds seen on the 22nd prior to the start of the clear-sky period. Many of the schemes simulated the clear-sky period correctly with the exception of the P3-YSU model run, which produced some clouds mid-day on the 23rd. This run also had difficulties with the downward longwave throughout this period, with large swings between 190 and 250 W m^{-2} .

Model runs using the Goddard CM scheme performed the best during the clear-sky period, with latent heat fluxes close to zero and longwave radiative fluxes closest to

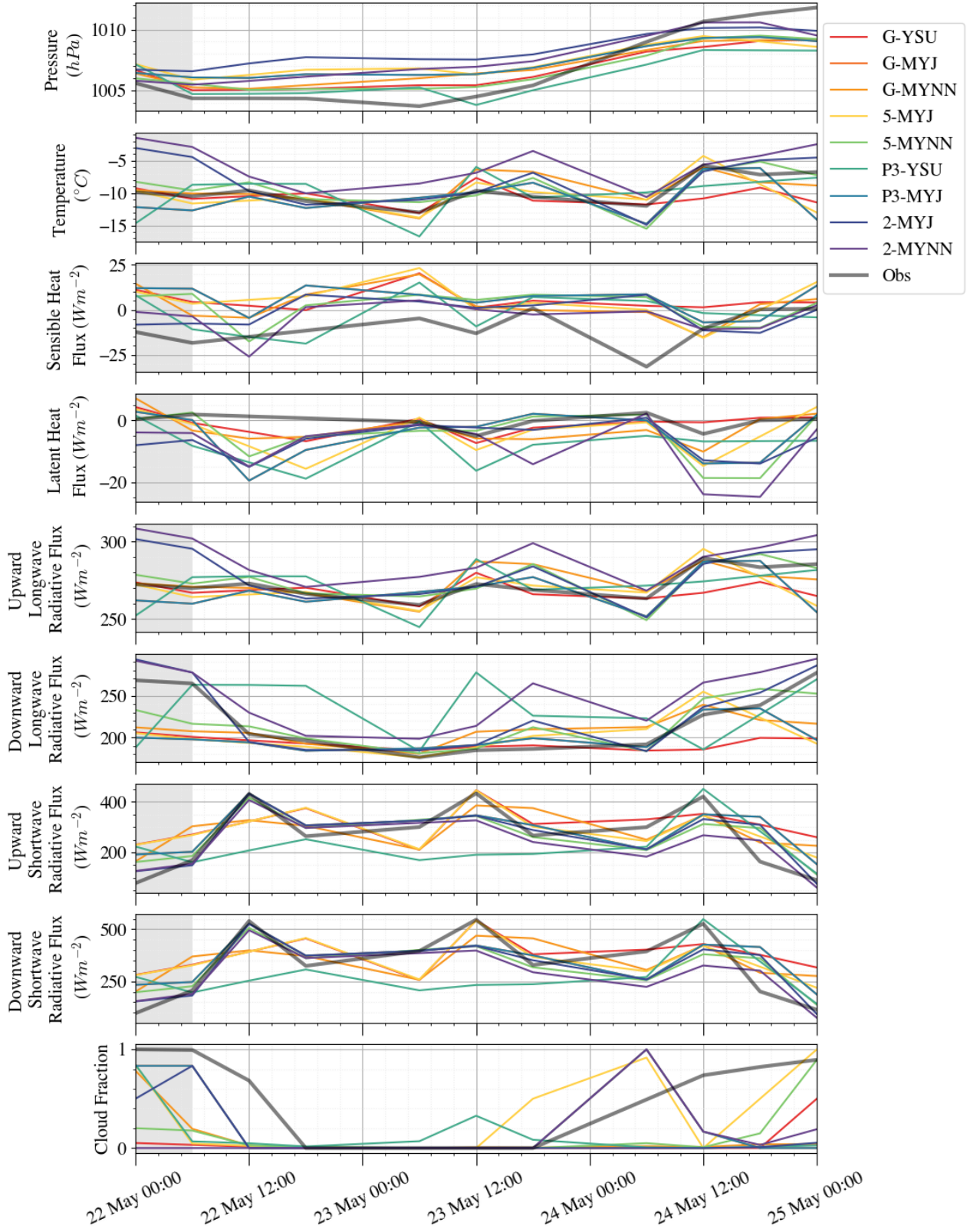


Figure 3.11: 6-hourly values for WRF modeled output (rainbow, acronyms in legend defined in Table 3.2) and observations (black) for sea level pressure, temperature, sensible heat flux, latent heat flux, downward longwave flux, upward longwave flux, downward shortwave flux, upward shortwave flux, and cloud fraction during the spring clear-sky period from 22 May to 25 May 2015. 46

the measurements. These schemes also had the most accurate surface temperatures.

This period immediately followed a storm period. In the previous case study, the model accurately predicted the onset of the storm but did not predict the strength or duration well. While this storm period was weak, it is possible that the model in some of the simulations did not accurately predict the end of that storm period, resulting in an earlier onset of clear conditions as is seen in many of the model runs.

3.4 Conclusions

In this study, Polar WRF was used to simulate surface fluxes over first-year sea ice from January to June 2015. Model results were compared to observations taken during the N-ICE field campaign. A collection of CM and PBL schemes were selected based on a literature survey of previous modeling studies both in the Arctic and elsewhere.

The schemes using the Morrison 2-Moment CM had the lowest biases in latent heat flux in the winter overall and performed best in the winter cold front case study. However, the overall temperature biases from these schemes were the largest in the winter, indicating that these schemes perform best under conditions like those seen in the winter case study, when the model did accurately forecast temperatures. The P3 CM scheme performed the worst in the winter, with the highest biases in both longwave flux, sensible heat flux, and temperature.

In the spring, latent and sensible heat fluxes produced by simulations using the Morrison 2-Moment scheme had the largest biases. Additionally, schemes using the MYNN PBL scheme had larger biases than simulations with other PBL schemes, generally producing a larger sensible heat flux than was observed. This indicates that, particularly in the spring, the MYNN PBL scheme is not producing the correct

near-surface temperature structure. Some model error can be attributed to an over-simplification of the ice surface, as the 3 km by 3 km grid size in the model was not small enough to resolve some open leads and melt ponds.

The time of year and the near-surface atmospheric temperature structure are important to consider when selecting CM and PBL schemes. In the winter when surface inversions are more likely to be present, the MYNN scheme produces the most accurate sensible heat flux estimations. However, the MYJ scheme appears to perform best for the latent heat flux and temperature. In the spring, when mixed-phase clouds are more common and the surface is starting to melt, the MYJ scheme still excels at estimating the latent heat flux and has some of the lowest biases.

The next chapter will describe the cloud conditions at N-ICE to give perspective into the conditions the model is trying to simulate. Cloud radiative forcing from the model is also calculated and explored for the 2-MYNN and G-YSU model simulations, as these had some of the lowest overall biases in winter and spring/summer, respectively. Chapter 5 looks at the equations used to calculate the sensible and latent heat fluxes and examines them independently of the model to determine if these equations could be at fault for some of the inaccuracies in the model output. The chapter 5 also explores alternative ways of calculating the stability equations and the fluxes themselves in an attempt to improve modeled fluxes. Chapter 6 will conduct sensitivity studies to determine if improvements can be made to the model. To conclude, Chapter 7 uses lessons learned in the previous chapters to make recommendations for changes in Polar WRF over first-year sea ice.

CHAPTER FOUR

CLOUD MACROPHYSICAL AND RADIATIVE PROPERTIES

OBSERVED DURING THE NORWEGIAN YOUNG SEA ICE FIELD

CAMPAIGN

The combined effect of all climate feedback processes is to amplify the climate response to forcing (virtually certain). While major advances in the understanding of cloud processes have increased the level of confidence and decreased the uncertainty range for the cloud feedback by about 50% compared to AR5, clouds remain the largest contribution to overall uncertainty in climate feedbacks (high confidence).

- IPCC Sixth Assessment Report, August 2021

4.1 Introduction

The global climate is heavily influenced by processes that occur in the Arctic. However, the Arctic environment is currently experiencing rapid change (Overland, 2011; Stroeve et al., 2007). Due to a lack of observations, it has been difficult to fully understand atmospheric processes in the polar regions (Persson, 2002). The atmospheric circulation in the Arctic is modified by changes in the overall climate, which, in turn, impact cloudiness and radiation at the surface (Zhang et al., 2008). The Advanced Very High-Resolution Radiometer (AVHRR) has observed that wintertime cloud cover over the Arctic Ocean is decreasing by 5% per decade. Meanwhile, in spring, increases as large as 15% per decade have been observed, which can likely be attributed to changes in atmospheric circulation (Schweiger, 2004). A decreasing trend in Arctic sea ice of 2.9% to 9.1% per decade was seen from 1979 through 2006 (Stroeve et al., 2007). Measurements of the energy balance and cloud properties

(fraction, height, microphysical, and temperature) can give important insight into climate processes and radiative transfer but are rarely measured together (Persson, 2002; Schweiger, 2004; Miller et al., 2017).

Clouds change the surface temperature by modifying both the shortwave and longwave radiation reaching the surface. Cloud microphysics, such as phase and particle size, as well as macrophysics, including fractional coverage, cloud height, and thickness, can influence the amount of radiation reaching the surface and, in turn, influence the impact of the cloud-radiation feedback (Uttal et al., 2002). This relationship is nonlinear and depends on both cloud and sea ice characteristics (Intrieri et al., 2002).

Clouds, as stated above, can modify both the radiation budget and impact the ice-albedo feedback. The influence of clouds is magnified by the high surface albedo and the lack of atmospheric moisture (Shupe & Intrieri, 2003). While we do have some estimates on how much the clouds can impact these feedbacks, more information is needed to quantify the exact influence. Sledd & L'Ecuyer (2019) states that the clouds are the most important driver in changes in top-of-atmosphere albedo over the entire globe, including at the poles, regardless of the high surface albedo. Cloud characteristics were shown to directly impact the ice thickness in studies by Curry & Ebert (1992); Beesley (2007).

The impact of clouds is often quantified using cloud radiative forcing (CRF). The CRF describes how clouds modify the radiation at the surface by taking the difference between the observed all-sky radiation and the estimated clear-sky radiation (Ramanathan, 1989). When positive radiative forcing is observed, there is a surplus of net radiation at the surface under cloudy skies, and they drive warming. When the

CRF is negative, cooling occurs at the surface under clouds. During clear skies, CRF should equal zero, as the actual radiation should be the same as the estimation of clear-sky radiation. Clear-sky radiation is often calculated from a radiative transfer model or estimated using observed clear-sky times.

Net cloud radiative forcing is a balance of surface warming and cooling due to modifications in radiation as a result of cloud cover. Curry & Ebert (1992); Intrieri et al. (2002) found that in the Arctic, clouds warm the surface over the entire year (have a positive cloud radiative forcing) except for in mid-July, when the sun is high above the horizon and the surface albedo is relatively low. This nearly year-round warming is due to the small amount of shortwave radiation. When there is solar radiation present, the low sun elevation angle and high surface albedo reflect much of the shortwave radiation away. In addition, the low-level clouds are often emitting longwave radiation at warmer temperatures than the ice surface due to surface temperature inversions (Shupe & Intrieri, 2003) and are always emitting more effectively than the clear sky.

The Norwegian Young Sea Ice Experiment (N-ICE2015, or N-ICE) (Granskog et al., 2018) is the first experiment to make comprehensive measurements of clouds and the surface energy balance from winter to summer since the Surface Heat Budget of the Arctic Ocean Experiment (SHEBA) in 1997 and 1998 (Walden et al., 2017a; Uttal et al., 2002). While N-ICE was conducted north of Svalbard in the Arctic Ocean, SHEBA took place north of Alaska in the Beaufort and Chukchi Seas, measuring the components surface energy budget (Persson, 2002; Andreas et al., 2010; Grachev et al., 2007), cloud properties (Turner, 2005; Turner et al., 2002; Intrieri et al., 2002; Shupe & Intrieri, 2004), and the resulting surface properties (Intrieri et al., 2002; Shupe &

Intrieri, 2004).

SHEBA was conducted almost two decades before N-ICE. Measurements were taken further into the ice pack (Cohen et al., 2017) and in thicker ice conditions. In addition, the meteorological conditions were different; detailed comparisons of N-ICE and SHEBA during the winter can be found in (Graham et al., 2017b). There were a few warm events during N-ICE caused by synoptic storms when temperatures reach 0 °C; these events were much warmer than any of the warm periods experienced during SHEBA. During the warm periods at N-ICE, the cloud properties were quite variable, suggesting that some of the changes in the surface energy balance could be the result of changes in cloud macrophysical and/or microphysical properties. Throughout SHEBA, mixed-phase clouds were observed 41% of the time. Graham et al. (2017b) states that in the winter, extreme radiative cooling events were more frequent during the N-ICE period than during SHEBA. More information about N-ICE can be found in Chapter 2.

Due to their importance to the surface energy budget over the Arctic Ocean, it is important to investigate the properties and radiative forcing of clouds during N-ICE and to compare the results to those observed during SHEBA. These results will provide useful constraints for models that traditionally have had difficulty simulating radiation at the surface of Arctic sea ice. Proper modeling of Arctic clouds in all seasons is essential for simulating accurate values of the surface energy budget, which is critical for modeling the seasonal cycle of sea ice. A critical parameter that was identified during SHEBA (Inoue et al., 2008; Tjernström et al., 2005) and other Arctic field experiments (Hines & Bromwich, 2017; Listowski & Lachlan-Cope, 2017; Hines et al., 2019) is the fraction of mixed-phase clouds. Graham et al. (2019) showed that

six atmospheric reanalyses have difficulty simulating Arctic clouds.

This paper uses various observations obtained during the N-ICE2015 field campaign to document the cloud macrophysical properties, the shortwave (SW) and longwave (LW) radiation, and the net cloud radiative forcing (CRF) at the surface of young Arctic sea ice. Section 2 describes the various measurements that were made during N-ICE to estimate CRF. Section 3 describes the methods to calculate CRF, which involved combining N-ICE measurements with radiative transfer modeling. Section 4 describes the seasonal transition of CRF from winter to summer. Section 5 compares the calculated CRF to modeled CRF in two model simulations. Section 6 presents the conclusions of this study.

4.2 Measurements

N-ICE was conducted during the six-month transition from winter to summer (January - June 2015) in the Arctic Ocean north of Svalbard. All of the instruments were either deployed onboard the Norwegian research vessel Lance or on the sea ice near the Lance. The instruments used in this study were a Vaisala CL-25 ceilometer, a Micropulse Lidar (MPL), twice-daily Vaisala RS92-SGP radiosondes, and Kipp and Zonen shortwave and longwave broadband radiometers. More information about N-ICE can be found in Chapter 2.

The synoptic context of the N-ICE field campaign is described by Cohen et al. (2017). The storms designated in Table 2 of Cohen et al. (2017) are of particular interest to this study. Six major and three minor storms occurred in winter (between 21 January and 14 March), while two major and seven minor storms occur in spring and summer (from 23 April through 11 June). The winter was characterized by a succession of particularly strong storms (as compared to climatology), while the

spring conditions were typical of that region of the Arctic (Graham et al., 2017a). The winter storms were accompanied by large increases in the integrated water vapor and changes in wind direction (Kayser et al., 2017) that influenced cloud properties.

A list of the meteorological instrumentation deployed during N-ICE is given in Table 1 of Cohen et al. (2017). A thorough description of the Vaisala RS92-SGP radiosondes launched during N-ICE is given by Kayser et al. (2017). A brief description of the meteorological measurements is given here as they pertain to this study.

Radiosondes were launched from the ice surface (Floe 1) and from the ship deck (Floes 2, 3, 4) to measure vertical profiles of temperature, relative humidity, wind speed and direction, pressure, and geopotential height up to a maximum altitude of 30 km. More information and analysis of the radiosondes can be found in (Kayser et al., 2017). Here the radiosonde profiles were combined with the surface and tower meteorological measurements to create input files for a radiative transfer model (section 3.2).

A MPL was used to measure backscattered radiation and depolarization from aerosols and clouds along the vertical path of the lidar beam (Spinhirne et al., 2007) throughout the N-ICE field campaign. The MPL was mounted on the upper deck of the R/V Lance and was approximately 10-12 meters above the sea ice surface. The MPL (Campbell et al., 2002) is a Sigma Space Version 4 polarization-sensitive lidar (532 nm) that was provided by the U.S. Department of Energy's (DOE) Atmospheric Radiation Measurement (ARM) Program. Raw MPL data was collected at 5-second temporal resolution and 15-meter spatial resolution up to an altitude of 18 km above the surface. The uncertainty in the base height of clouds (derived from MPL measurements) is \pm 2 % due to timing uncertainties within the instrument. The lidar beam

is attenuated more by water droplets than ice particles, so our determination of the cloud fractions of water and ice clouds is biased toward a higher percentage of water than ice. In addition, the MPL signal is highly attenuated by optically thick clouds, so when a low thick water cloud is detected, it is possible that additional cloud layers may exist above this layer that is not detected by the MPL. In these cases (which occur often in spring and summer), we assume that the low thick cloud layer is solely responsible for the cloud radiative forcing at the surface. Post-processing of the MPL measurements is described below in section 4.3.1 and is based on the analysis methods of Campbell et al. (2002), Flynnna et al. (2007), and Stillwell et al. (2018).

Broadband radiometers were deployed at 1 to 1.2 *m* above the surface near the meteorological tower to measure upward and downward components of longwave (Kipp and Zonen CGR4) and shortwave (Kipp and Zonen CMP22) radiation. Kipp and Zonen CVF4 ventilation units were used to heat and ventilate the radiometers to avoid frosting of the instrument domes during periods of high relative humidity. The surface skin temperature was calculated from the upwelling and downwelling longwave radiation, assuming a broadband surface emissivity of 0.99 (Grenfell & Warren, 1999); the surface skin temperature was used as input for radiative transfer modeling. More information about the radiometers, including analysis of the surface energy budget, can be found in Walden et al. (2017a).

In spite of deploying a relatively comprehensive instrument suite over sea ice during N-ICE2015, there are some caveats regarding these measurements. Most importantly, when the optical depth of the overlying clouds is large, the MPL is unable to penetrate completely through the clouds. This is especially true when liquid water clouds are present, which occur often in spring and summer and occasionally in win-

ter. Thus, the cloud macrophysical properties that are reported here represent only the lowest layer of cloud cover in many cases. It would have been preferable to also deploy a cloud radar, which is less sensitive to liquid water, that would have profiled clouds above any liquid layers. Other additional instruments would have been useful for measuring the liquid water path (microwave radiometer) and cloud microphysical properties (infrared spectrometer, cloud radar). So given the instruments that were deployed, we report on both the cloud macrophysical properties (within the capability of the MPL) and cloud radiation, with a focus on surface cloud radiative forcing, which is most sensitive to the lowest cloud layer.

4.3 Methods

In this study, the macrophysical and radiative properties of clouds are described throughout the N-ICE2015 field campaign. Below we explain how cloud base height, temperature, fraction, and cloud radiative forcing are derived from the instruments deployed during the field campaign.

4.3.1 *Cloud Macrophysical Properties*

Measurements from the MPL and routine radiosonde launches during N-ICE provide estimates of three macrophysical cloud properties: cloud fraction, temperature, and phase. Raw data from the MPL were corrected for pulse pileup (saturation) and background light (from sky and/or detector dark noise), creating “background-subtracted raw counts”. Several additional corrections are then applied: afterpulse calibration, daily normalization to the median laser pulse energy, and an overlap correction to remove the effect of range-dependent collection efficiency of the fiber-coupled receiver (Campbell et al., 2002; Mendoza & Flynn, 2006). Both signal-to-

noise (SNR) and speckle filtering was then performed on the data.

Two lidar parameters are then calculated for our analysis: backscatter ratio and polarization. The backscatter ratio is the ratio of total backscattering to molecular backscattering (Klett, 1981). The molecular backscattering is estimated using twice-daily radiosonde data. The radiosonde profiles of pressure, temperature, and water vapor were interpolated in time and space to approximate molecular particle number density. Molecular backscattering was then calculated using the Rayleigh scattering approximation (Bohren & Clothiaux, 2006; Bohren & Huffman, 2008; Placzek, 1934).

In this study, the backscatter ratio for each lidar volume pixel is used to distinguish clear air from liquid or ice hydrometeors. A volume pixel, or voxel, is a lidar measurement at a particular time and altitude range. Backscatter ratios greater than 7.5 were considered cloudy voxels, while ratios less than 7.5 were identified as clear voxels (including aerosols). The cloud-base height is the lowest altitude a cloud is detected, and the cloud top is the highest. As mentioned above, if the optical depth of the lowest cloud is large, the MPL will only accurately detect the base of the lowest cloud. Once the cloud base is determined, the cloud temperature can be estimated by interpolating the twice-daily radiosonde profiles to the particular time and altitude of the cloud base. The cloud fraction (occurrence) for a given time period is then determined by calculating the fraction of time when a cloud is present vertically overhead.

The polarization of the MPL is calculated using equations 1.4 (depolarization ratio) and 1.5 (depolarization) of Flynn et al. (2007). These parameters, plus the error in the depolarization ratio, are used to classify the cloudy voxels into three categories: liquid, ice, and unclassified cloud. Cloudy voxels with depolarization

ratios greater than 0.1 are classified as ice, while voxels with depolarization ratios lower than 0.1 are liquid. Cloud voxels cannot be classified as mixed-phase and are categorized as liquid versus ice as done in previous lidar studies (e.g., Intrieri et al. (2002)). The classification is further refined using the error in depolarization ratio, requiring this error for liquid and ice to be less than 10 %. If the depolarization-ratio error is greater than 10 % for the initial classification of liquid or ice, the cloud voxel is classified as an “unclassified cloud”.

Once each voxel is classified, a column cloud mask is created for comparing the range-resolved lidar measurements with the column measurements made by the broadband radiometers. If the atmospheric column above the lidar lacks clouds at any altitude, the column is considered clear, otherwise, the column is cloudy. Columns containing liquid voxels at any altitude are considered liquid. This implies that a single liquid voxel can override numerous ice voxels. This is done because liquid clouds in the Arctic typically have large optical depths (e.g., Curry et al. (1996)) relative to ice clouds.

4.3.2 Cloud Radiative Properties

The all-sky net radiation at the surface Q_{all} is calculated using 1-hour average radiation measurements from the four Kipp and Zonen radiometers, where the Q_{all} is defined in Eq. 4.1. Q_{all} is equal to Q_{net} for observations.

$$Q_{all} = Q_{net} = (Q_{lw\downarrow} - Q_{lw\uparrow}) + (Q_{sw\downarrow} - Q_{sw\uparrow}) \quad (4.1)$$

$Q_{lw\downarrow}$, $Q_{lw\uparrow}$, $Q_{sw\downarrow}$ and $Q_{sw\uparrow}$ are the components of downward longwave, upward longwave, downward shortwave and upward shortwave radiation. In this paper, pos-

itive net radiation is defined as into the surface (Miller et al., 2015).

Cloud radiative forcing is defined in Eq. 4.2, 4.3, and 4.4 (Ramanathan, 1989; Miller et al., 2015).

$$CRF = Q_{all} - Q_{clear} \quad (4.2)$$

$$\begin{aligned} CRF = & [(Q_{lw\downarrow} - Q_{lw\uparrow}) + (Q_{sw\downarrow} - Q_{sw\uparrow})]_{all} \\ & - [(Q_{lw\downarrow} - Q_{lw\uparrow}) + (Q_{sw\downarrow} - Q_{sw\uparrow})]_{clear} \end{aligned} \quad (4.3)$$

$$\begin{aligned} CRF = & [(Q_{lw\downarrow} - Q_{lw\uparrow})_{all} - (Q_{lw\downarrow} - Q_{lw\uparrow})_{clear}] \\ & + [(Q_{sw\downarrow} - Q_{sw\uparrow})_{all} - (Q_{sw\downarrow} - Q_{sw\uparrow})_{clear}] \end{aligned} \quad (4.4)$$

The clear-sky values for both downward longwave and shortwave radiation in Eq. 4.4 are calculated using the Rapid Radiative Transfer Model (RRTM) (Mlawer et al., 1997) because there were too few clear-sky cases during N-ICE2015 to properly estimate the clear-sky flux using the radiation measurements. For SW calculations, it is important to specify the atmospheric concentrations of N_2 and O_2 for molecular scattering and H_2O , O_3 and O_2 for molecular absorption. The surface albedo must also be specified as a function of the surface type and solar zenith angle. For LW calculations, the vertical temperature structure must be specified, as well as the concentrations of the primary infrared greenhouse gases (H_2O , CO_2 , O_3 , CH_4 , N_2O , CO).

It is important to specify a vertical grid in RRTM that resolves the near-surface temperature structure because near-surface temperature inversions occurred during N-ICE (Kayser et al., 2017). Here we use three layers (surface, 2 m, 4 m) below 10

m , then increasing spacing above $10\ m$: $10\ m$ spacing from 10 to $100\ m$, $100\ m$ from $100\ m$ to $1\ km$, $1\ km$ from 1 to $30\ km$, and $5\ km$ from 30 to $60\ km$. RRTM was run hourly for the entire field campaign.

Here the concentrations of N_2 and CO_2 are assumed to be uniformly mixed vertically, while the seasonal variability of the CO_2 concentration is accounted for by using monthly averaged measurements from Summit Station, Greenland made by the Global Monitoring Division (GMD) from National Oceanic and Atmospheric Administration (NOAA). The profiles of O_2 , CH_4 , N_2O , and CO are from the sub-Arctic winter standard atmosphere (McClatchey, 1972). The profiles of O_3 were measured at Ny-Ålesund, Svalbard, and were interpolated to hourly profiles. The profiles of temperature and humidity were constructed using: 1) the sensors at $2\ m$ and $4\ m$ on the meteorological tower, 2) the radiosondes from $10\ m$ to the altitude of the balloon burst, and 3) values from the sub-Arctic winter standard atmosphere from the maximum altitude of the radiosonde to $60\ km$. On a few occasions, the termination height of the radiosonde was low (below $10\ km$). In these cases, the monthly average sonde profiles were used from the maximum altitude of the sonde through 24 to $30\ km$ depending on the month. The surface skin temperature was derived from the longwave radiation (Walden et al., 2017a) and assumed a surface snow emissivity of 0.99 (Persson, 2002; Grenfell & Warren, 1999).

The meteorological tower data were compared to the lowest $10\ m$ measured by the radiosondes as a quality check because of the strong dependence of longwave CRF on the near-surface temperature structure. The difference between the $2-m$ temperature measured on the meteorological tower and the temperature interpolated between radiosondes exceeded $1^{\circ}C$ in only 1.2% of the hourly profiles. The other

levels (2, 4, and 10 m) exceeded a $1^{\circ}C$ difference of less than 0.5% of the time. To ensure the lower profiles were as accurate as possible, the tower temperatures and surface temperatures calculated from LW fluxes were used when available but did not change the lower levels of the profiles significantly. Linear interpolation between the tower and sonde measurements was sufficient to represent the lower atmosphere because the altitude range of these temperature adjustments was small (<10 m).

The shortwave spectral surface albedo was estimated using the snow albedo model described by Wiscombe & Warren (1980); see their Eq. 4. This model depends on properties of the snow (single-scattering albedo (ω) and asymmetry factor (g)), as well as the solar zenith angle (θ). The single-scattering albedo was determined for each day using noontime albedo measurements from Walden et al. (2017a). A fixed

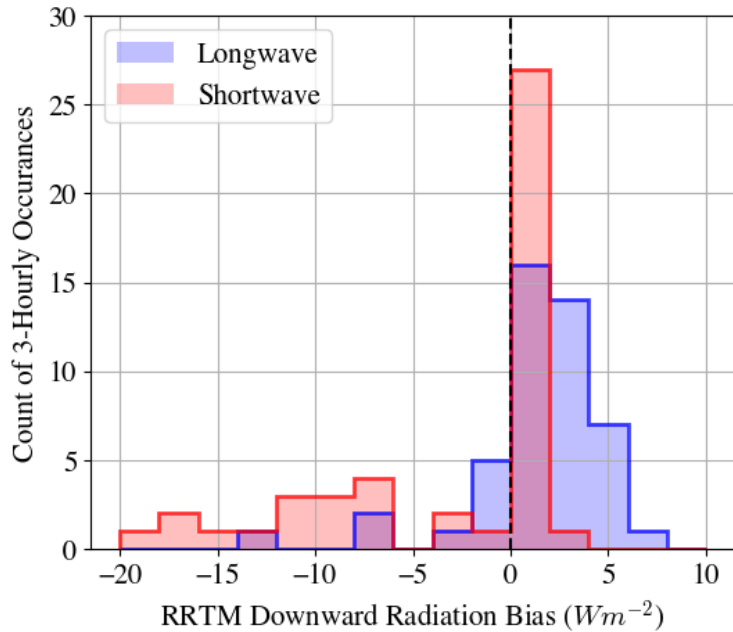


Figure 4.1: RRTM modeled downward longwave flux bias (RRTM - observations) in blue and downward shortwave flux bias in red. Three-hourly values during clear-sky times only are shown.

value of $g = 0.9$ was used. These values were then used along with the hourly solar zenith angle to calculate the albedo throughout the day. The cloud cover also greatly affects the surface albedo, and the reduction in direct radiation in favor of diffuse was parameterized using a diffuse fraction. Cloud fraction for the two-hour period surrounding the time of the albedo calculation was used to determine the percent reduction required to account for the diffuse fraction. Percent reductions in albedo were scaled linearly from 6 to 0%, with full cloud cover having a 6% reduction imposed, and clear sky remaining unchanged.

Uncertainties are introduced into RRTM shortwave and longwave calculations from uncertainties in the albedo estimates, atmospheric profile construction and interpolation, and the various measurements. Despite this, the RRTM calculations agree well with the few clear-sky SW and LW measurements from N-ICE2015. Figure 4.1 shows a histogram of the differences in SW and LW radiation (modeled minus measured) for clear days. The mean SW bias is -2.5 Wm^{-2} with a standard deviation of 9.6 Wm^{-2} , while the mean LW bias is 1.3 Wm^{-2} with a standard deviation of 3.6 Wm^{-2} . Thirteen three-hour periods that appeared clear in the data were removed as they were at the start of an observation period (the beginning of a floe). These periods had significant differences but, because these were some of the first measurements during their respective floes, they were removed due to the potential for instrument error.

4.4 Results and Discussion

The conditions observed at N-ICE were unique not only because it observed the transition season for the first time since SHEBA. Winter storm periods were measured that brought extremely large and rapid transitions of cloud properties that coincide

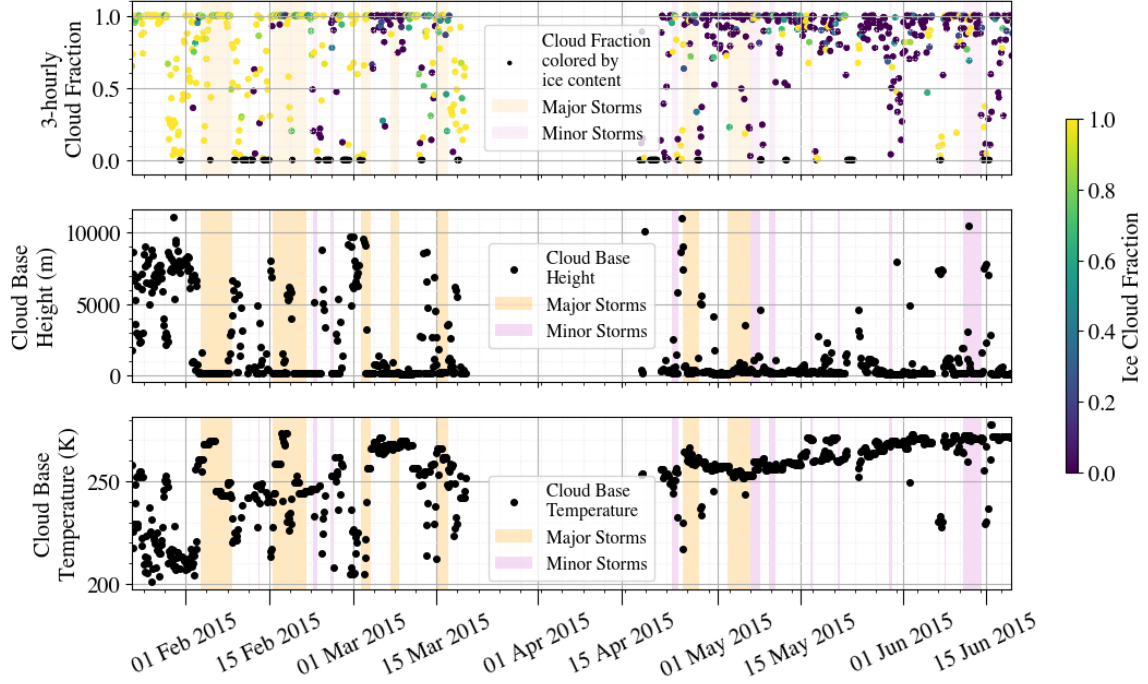


Figure 4.2: Vertical cloud fraction and ice content within the cloud are shown in the top figure. Ice content is defined as the percentage of the cloud that can be determined to be ice particles (yellow represents more ice and purple less). The middle panel shows the mean cloud base height and the bottom panel shows the cloud base temperature. All values are 3-hourly averages. Storm periods are shaded in orange (major) and pink (minor) shading.

with changes in turbulent fluxes documented by Walden et al. (2017a) and Graham et al. (2017b).

The upper panel of Figure 4.2 shows the frequency of cloud occurrence, or the percentage of a three-hour period that cloud was observed over the MPL, indicated by colorful dots. The color indicates the ice cloud fraction or the percentage of the observed clouds that could be definitively categorized as ice. During the first half of the experiment in winter, it was common for days to have cloud fractions below 50%, with 16 out of the 61 days prior to the long break in observations having less

than 50% cloud cover. After the break, however, there are only 12 days out of the 89 days that are below 50% cloud cover. The mean cloud fraction during the first half of the experiment is 70% (standard deviation of 30%), and after is 75% (standard deviation of 28%). Climatologically, a decrease in clear days has been seen for this region, contributing to a long-term warming trend (Kayser et al., 2017). The entire experiment, including a large number of cloudy days, is put into climatological context by Graham et al. (2017a) and Kayser et al. (2017). For the purpose of this study, there was significantly less cloud cover in winter than in the spring and summer, and the clouds observed during winter had larger ice content than those observed during spring.

During Floes 1 and 2 (winter), every day has at least some ice cloud present. Most of the days have primarily ice clouds with the exception of a week in early March, which corresponds to a period when the cloud base was low (Figure 4.2, middle panel) and cloud temperature was near freezing (265 - 270 K, Figure 4.2, bottom panel). Some days have a small percentage of unknown cloud fraction, but this category only exceeds 20% of the daily cloud existence once during the first half of the experiment.

The fraction of water clouds greatly increases during Floes 3 and 4 (spring and summer). These results are not surprising, as increasing temperature and increasing water fraction are expected. There are still ice clouds present nearly every day through the end of the experiment, many of which are high, thin clouds. The water clouds, however, were primarily thick and close to the surface. Some of the ice can be attributed to mixed-phase clouds with both water and ice through the mid-troposphere. Low-level ice clouds were not common during this period.

Cloud base heights (Figure 4.2, middle panel) in the first month of the experiment

are, on average, higher than the rest of the experiment. Once Floe 3 starts cloud base heights are almost always below 2 km. Figure 4.3 shows the frequency of cloud base heights for each month throughout the experiment with lines indicating the mean cloud base height. The mean height for January, which includes only a 15-day, relatively quiescent period, is 6.45 km, while the rest of the months' mean cloud heights are below 2 km. Mean cloud heights decrease throughout the experiment, with the lowest mean cloud base height present in May at just below 1 km. During the second half of the experiment, the majority of the clouds have a low cloud base height

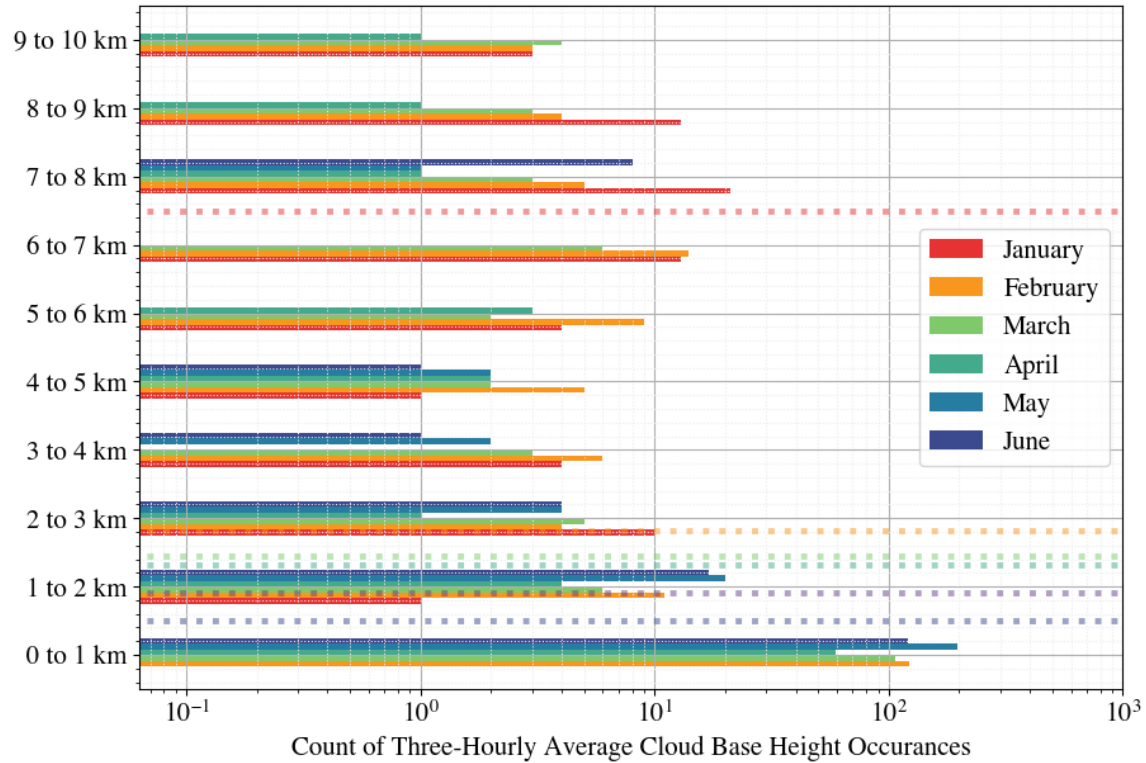


Figure 4.3: Binned cloud base height by month. Frequency distributions are shown as bars colored by month. The monthly mean cloud height is shown by the horizontal line in the corresponding color. Note the x-axis is shown as a log scale to make differences more clear.

and a high percentage of water present. These clouds had large enough optical depths that they caused complete attenuation of the micropulse lidar beam, resulting in an inability to view clouds above them. As mentioned above, this inhibits the ability to report on higher-level clouds but does not impact the ability to understand the surface energy budget, as these low-level clouds are the most radiatively important.

Cloud base temperature closely mimics the cloud base height for the majority of the experiment. During the second two floes, the cloud base temperature gradually approaches freezing while the cloud base height stays fairly consistently near the surface. This slow increase in cloud base temperature reflects the increase in atmospheric temperature as more solar radiation reaches the Arctic.

4.4.1 *Cloud Radiative Properties*

This section describes the variations in shortwave and longwave fluxes measured throughout N-ICE2015. These fluxes are used to calculate the shortwave, longwave, and net CRF throughout the campaign as defined by Eq. 1.3 above. These measurements are then categorized according to the cloud macrophysical properties described above.

Figure 4.4 shows the time series of the shortwave (upper panel), longwave (middle panel), and net (lower panel) radiative fluxes. During Floe 1 (January and February), net flux (also, net longwave flux) dips to around -50 W m^{-2} during non-storm periods (unshaded) and approaches 0 W m^{-2} during storm periods (shaded). During major winter storms, downward longwave flux increases from between 100 and 150 W m^{-2} to around 300 W m^{-2} , sometimes within only a few hours. Upward longwave flux mirrors these changes decreasing from -200 to -300 W m^{-2} . During non-storm periods, the upward flux is around -200 W m^{-2} while the downward flux is just over $+100 \text{ W m}^{-2}$,

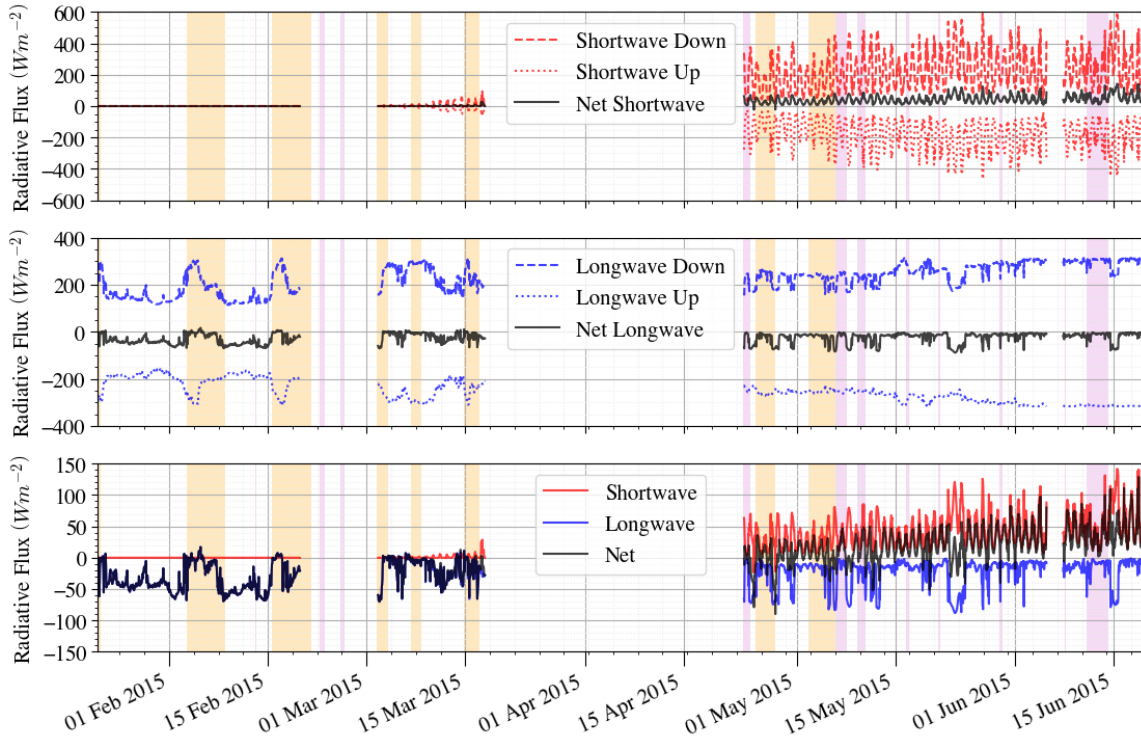


Figure 4.4: Shortwave (top), longwave (middle), and net (bottom) components of radiative flux. Black lines represent net flux, dotted indicating upward flux, and dashed downward. Major and minor storm periods are shown by the orange and pink shading, respectively.

resulting in negative net flux. When the net flux approaches zero, as it does during storm periods, it indicates that clouds are relatively low and warm and have a large enough optical thickness to balance the longwave flux coming from the surface.

In March (Floe 2), the downward and upward longwave fluxes more closely balance each other. This is due to a generally higher downward longwave flux from warmer cloud base temperatures and higher optical thicknesses from a greater fraction of liquid water clouds (Figure 4.3, top panel). During non-storm periods, the net longwave flux reaches a minimum just below $-50 Wm^{-2}$ but is more frequently around $-25 Wm^{-2}$. Storm periods continue to bring the net flux near $0 Wm^{-2}$, as

lower and warmer clouds predominate. Small amounts of shortwave flux exist during the end of this floe (net $< 50 \text{ W m}^{-2}$) as the sunlight returns to these latitudes, but has little influence on net flux due to a large amount of reflected shortwave flux from the surrounding snow.

During Floe 3 (spring), the net longwave flux reaches as low as -70 W m^{-2} but is more often around 0 W m^{-2} . This is the result of increased and consistently high downward longwave flux. This is when the atmosphere is in an opaquely cloudy state (Stramler et al., 2011; Graham et al., 2017b). As the experiment transitioned from winter into spring, cloud base height decreased and cloud occurrence increased. The decrease in cloud height and warming of the atmosphere results in an increased downward longwave flux from the clouds. In addition, during this period, the floe drifted into warmer ocean water (Kayser et al., 2017) and the net shortwave flux increased, which increased the atmospheric temperature above the ice and the magnitude of the upward longwave flux. Upward longwave radiation is fairly consistent throughout this floe, starting around -225 to -250 W m^{-2} in late April and steadily increasing in magnitude to around -300 W m^{-2} in June. During this period, the upward longwave flux does not mirror the downward longwave flux as closely as it does during winter, especially as the surface temperature approaches freezing ($Q_{LW\uparrow} \approx 316 \text{ W m}^{-2}$).

The net shortwave flux during Floe 3 generally fluctuates between 0 and 100 W m^{-2} , with only 6 days exceeding 100 W m^{-2} . The total net flux follows the daily pattern of the net shortwave flux and is primarily greater than 0 W m^{-2} . During the start of this floe, net flux drops below 0 W m^{-2} during the two major storm periods. These drops are caused by both a decrease in net shortwave flux (due to increased cloud optical thickness) and a decrease in net longwave flux (higher cloud base and

lower cloud base temperature, Figure 4.2). After this, there are a few more occurrences in which the flux decreases below 0 Wm^{-2} , which coincide with decreases in the net longwave radiation, indicating higher cloud bases and/or lower cloud fractions (Figure 4.2). It is important to note that the clear-sky modeled radiation was estimated to be slightly less than the measured radiation, resulting in clear-sky periods being slightly negative in some cases. This can be seen in the first floe when the upward longwave CRF is slightly below zero, creating a negative CRF. This does not mean that clouds were cooling the surface at this time but is a result of the modeled clear-sky uncertainty.

June (Floe 4) experienced the greatest magnitude of net flux. During a storm period from 11 June to 14 June, net longwave flux decreases from 50-75 to about 0 at the same time as an increase in cloud base height from near the surface to around 10 km (Figure 4.2, middle panel). This is the largest decrease in net flux in June. During this time, optically thick clouds block shortwave radiation from reaching the surface. After the storm cloud base height increases, cloud base temperature decreases, and cloud fraction decreases (Figure 4.2) indicating that, after the storm passed, clouds became high and more scattered.

Cloud radiative forcing at the surface is shown in Figure 4.5. Longwave CRF dominates throughout the field campaign. During Floes 3 and 4, the shortwave CRF has an increasing influence on the net CRF, but only decreases it by a small amount. Upward and downward shortwave CRF counteract each other due to the high albedo of the snow cover on the sea ice, resulting in net shortwave CRF between -50 and 0 Wm^{-2} . (Walden et al. (2017a) report values of the surface albedo during N-ICE2015.)

Due to the positive CRF throughout almost the entire field campaign, clouds are

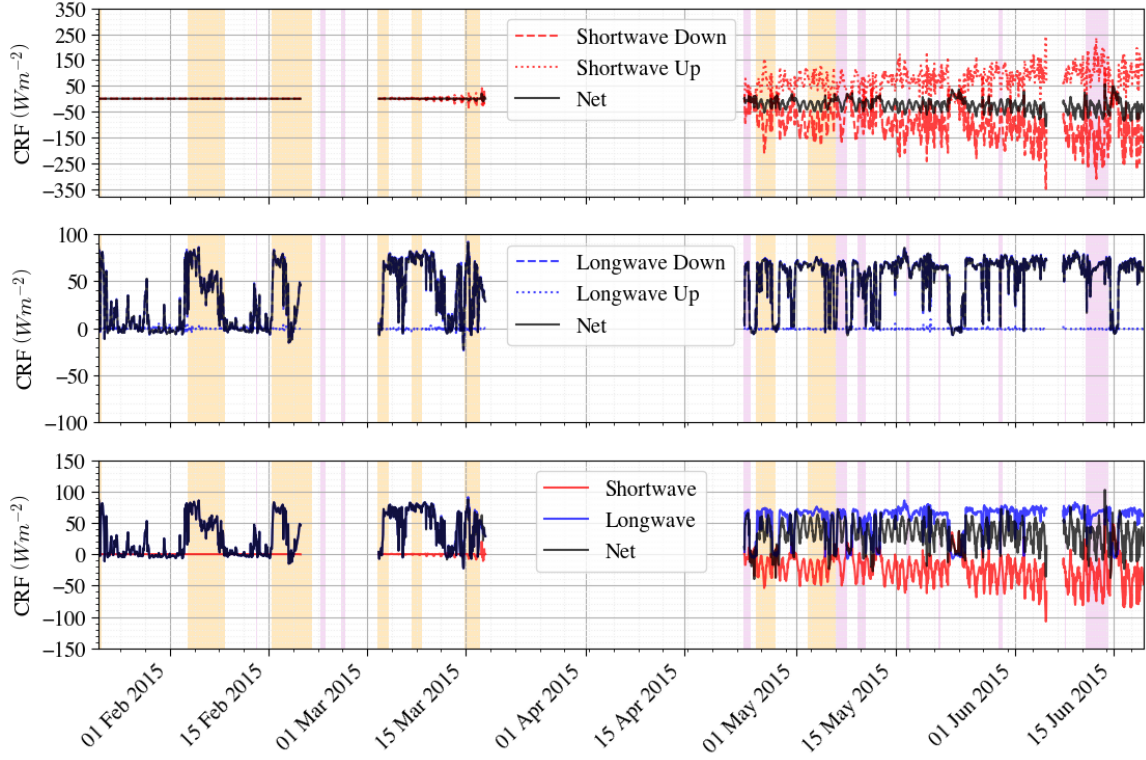


Figure 4.5: Shortwave (top), longwave (middle), and net (bottom) components of cloud radiative forcing. Black lines represent net flux, dotted indicating upward CRF, and dashed downward. Major and minor storm periods are shown by the orange and pink shading, respectively.

generally warming the surface. During SHEBA and other studies (Schweiger, 2004; Cogley & Henderson-Sellers, 1984; Walsh & Chapman, 1998; Curry et al., 1996) clouds were found to warm the surface throughout the entire year except in mid-summer when the solar zenith angle was high and albedo low. The length of this cooling period was highly dependent on albedo estimations (Intrieri et al., 2002). As N-ICE did not continue through the entire summer, it is impossible to say if there would be a period of negative cloud radiative forcing later in the summer in this region, when further melt drove the albedo lower. It is true, however, that the net CRF decreased with increasing solar radiation near the end of the campaign.

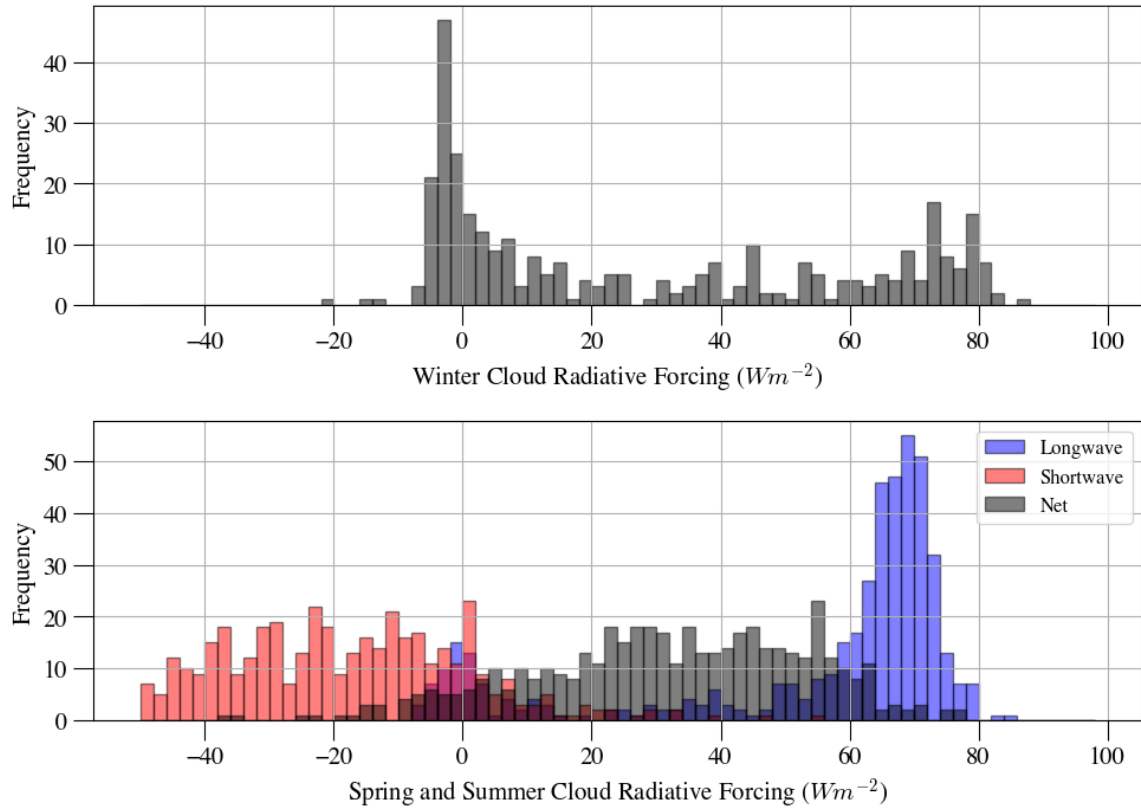


Figure 4.6: Histograms of cloud radiative forcing for winter (top, Floes 1 and 2) and spring/summer (bottom, shortwave radiation indicated in red, longwave in blue, and net in black). Spring/summer is defined as Floes 3 and 4.

Histograms of the longwave, shortwave, and net CRF, shown in Figure 4.6, are divided by floe. Winter is defined as Floes 1 and 2 and spring/summer is Floes 3 and 4. Shortwave values were very low during the winter floes and are not displayed here. In winter (top panel), the histogram (LW only) shows a slightly bimodal distribution, with one large peak near $0 Wm^{-2}$ and another small peak between about 50 and $80 Wm^{-2}$. (Note that the negative value of the large peak at $3 Wm^{-2}$ may be due to the slight overestimation in the clear-sky flux as the estimated bias is just under $3 Wm^{-2}$ for shortwave radiation.) These two modes describe clear ($0 Wm^{-2}$)

and cloudy (75 Wm^{-2}) conditions. A range of cloud radiative forcing values is seen leading up to the peak of the distribution at about 85 Wm^{-2} due to the range in cloud properties (fraction, phase, height) and their associated radiative impacts during the winter. The winter had quite variable cloud conditions compared to those in summer in terms of height, temperature, and daily fraction. The highest winter CRF occurred during the storm periods when cloud fraction was large, clouds were primarily close to the surface and composed of ice, and the cloud base and surface temperatures both increased.

In the spring/summer (Figure 4.6, bottom panel), the range of net CRF is smaller relative to winter. This is due to the negative shortwave CRF (cooling) that counteracts some of the positive longwave CRF. Longwave CRF in summer is between about 0 Wm^{-2} and 80 Wm^{-2} , with the latter (cloudy) peak being the larger of the two (unlike winter). The majority of clouds during summer result in from 50 to 80 Wm^{-2} of longwave CRF. Shortwave CRF ranges between just above zero to -30 Wm^{-2} , with a few values as low as -50 Wm^{-2} . SW CRF values are the result of the uncertainty in the clear-sky estimations. The result of these two competing components of CRF is a slightly bimodal distribution of net CRF, with a small peak near 0 Wm^{-2} and a larger peak between 30 to 70 Wm^{-2} . The peak near 0 Wm^{-2} is small due to the limited number of clear-sky days seen during the summer. Clouds were consistently low and thick throughout the spring and summer, resulting in more uniform net CRF values throughout these two seasons than in winter.

Figures 4.7 and 4.8 display how the net cloud radiative forcing depends on the cloud's macrophysical properties. Figure 4.7 is for winter (Floes 1 and 2), and Figure 4.8 is for spring and summer (Floes 3 and 4). During the winter, cloud base height,

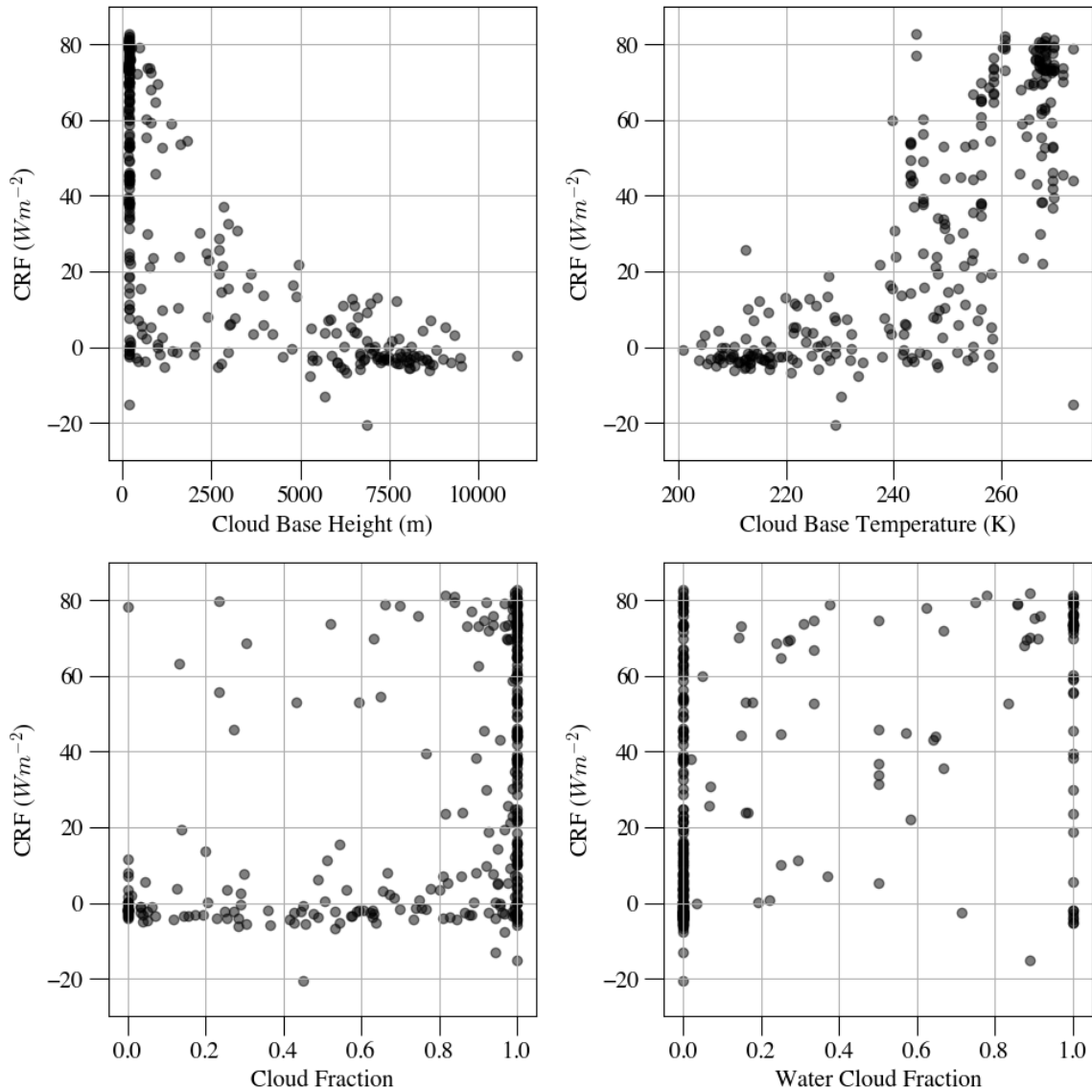


Figure 4.7: Cloud radiative forcing vs cloud base height (top left), cloud base temperature (top right), mean cloud fraction (bottom left), and water cloud fraction (bottom right) for the winter season (Floes 1 and 2). All panels are 3-hourly values. Net cloud radiative forcing is only comprised of longwave radiation during this time of year, so black dots represent both the net longwave CRF and the net CRF.

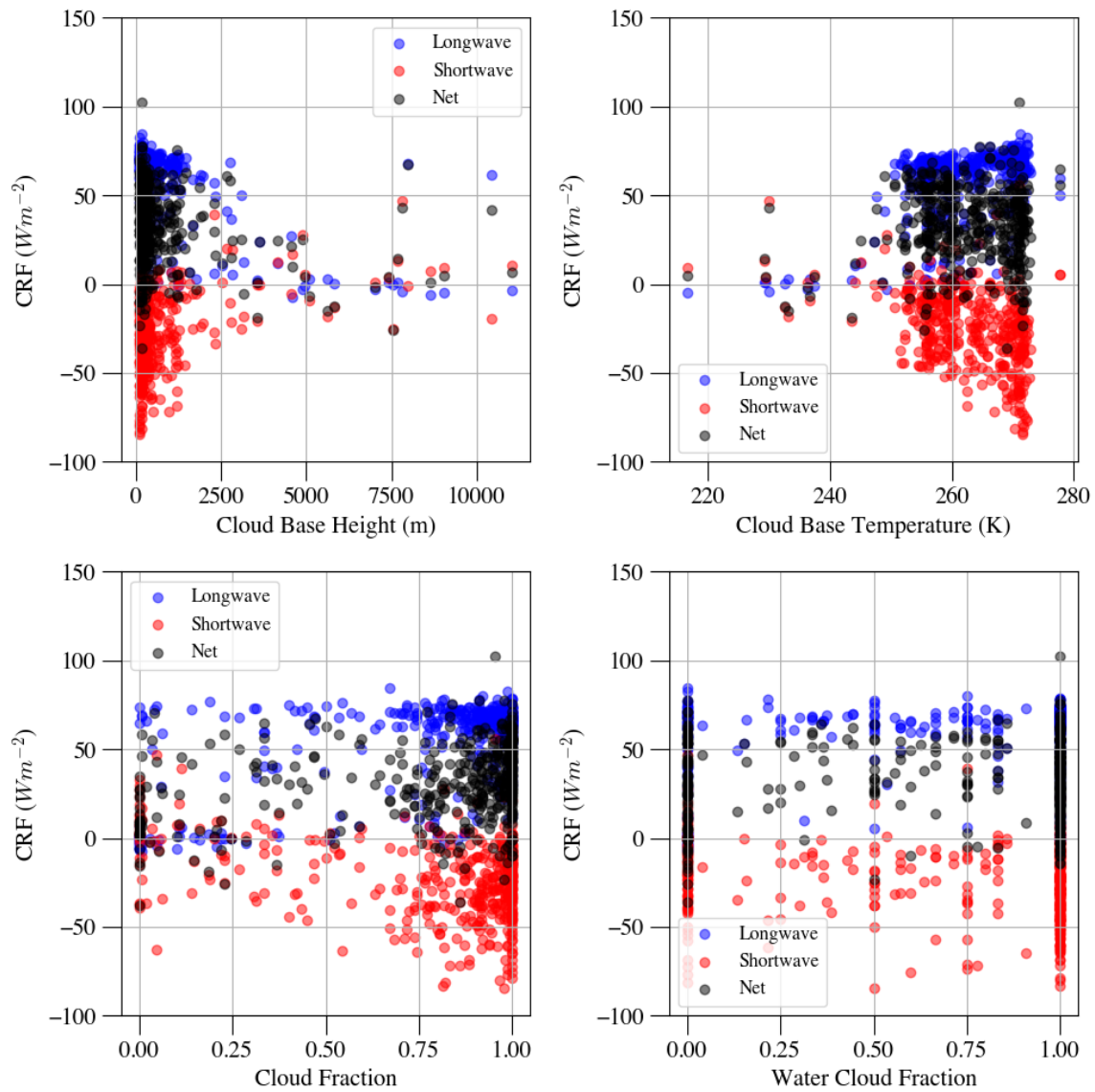


Figure 4.8: Cloud radiative forcing vs cloud base height (top left), cloud base temperature (top right), mean cloud fraction (bottom left), and water cloud fraction (bottom right) for the spring/summer season (Floes 3 and 4). Longwave radiation is represented by blue dots, shortwave by red dots, and net by black dots in each scatter plot.

and cloud base temperature have the most effect on the net CRF. This is no surprise as the free atmosphere is warmer close to the ground, resulting in low clouds having a larger longwave influence on the surface. Shupe & Intrieri (2004) found that clouds with temperatures cooler than 243 K (-30°C) often had similar longwave radiative properties to clear sky conditions. In winter at N-ICE, there is a transition in radiative values around 235 K . Winter clouds with base temperatures greater than 235 K had a larger spread in cloud radiative forcing values of about 60 W m^{-2} . Values lower than this still had variation in CRF, but were within 20 W m^{-2} of clear-sky conditions and were more sensitive to changes in cloud base temperature. In the summer, this transition occurred closer to the 243 K cutoff reported by Shupe & Intrieri (2004). However, due to the limited number of high, cold clouds, there were not many clouds below this threshold. In summer the LW CRF was close to zero for these lower temperatures, in better agreement with the results from Shupe & Intrieri (2004).

Mean cloud fraction (Figure 4.7 and 4.8, lower left panels) does not have as clear of a correlation with mean surface CRF.; In the winter, periods with below 50% cloud fraction have less than 10 W m^{-2} of CRF, while periods with cloud fraction greater than 50% can have CRF values that range from around 0 to just under 80 W m^{-2} . These slight trends were also seen by Shupe & Intrieri (2004) during the SHEBA experiment.

In spring and summer, the relationships between cloud base height and cloud base temperature are less obvious. This is due to the lack of variety in cloud characteristics during this period and the dependence on solar zenith angle. Most clouds were below 2 km with cloud base temperatures above 250 K . Periods of higher, cooler clouds were present only during a few storm periods, one near the end of the experiment.

These clouds had a higher ice fraction than the other summer clouds, likely due to their height.

There is no apparent correlation between the fraction of cloud that is water and the amount of CRF in either season. Schweiger et al. (1999) stated that the relationship between particle size and the amount of longwave CRF is not significantly different for liquid and ice particles. They did report a significant difference, however, in shortwave CRF, as the different shapes have different influences on shortwave scattering. However, results from N-ICE do not show differences in water and ice clouds. This is likely due to the inability to determine the thickness of the cloud, as the lidar pulse will attenuate near the base of optically thick clouds, and the wide variety of solar zenith angles that were experienced during the transition to summer.

The cloud macrophysical and radiative effects seen here could be representative of conditions that are becoming more prominent with climate change. A thorough understanding of the cloud influence on the surface is vital both for forecasting local impacts, such as ice melt or change in surface fluxes, and for use in larger climate circulation models for a more accurate understanding of global climate change. Cloud properties (such as height, phase, and temperature) have a large influence on longwave radiation.

4.5 Cloud Radiative Forcing modeled by Polar WRF

Cloud radiative forcing from the Weather Research and Forecasting model (WRF) with polar enhancements (described in Chapter 3) is shown in Figure 4.9. Two model simulations were selected based on their performance in spring and summer during N-ICE. The model run using the Morrison Bulk Two-Moment cloud microphysics (CM) scheme and the Mellor–Yamada Nakanishi Niino (MYNN) planetary boundary

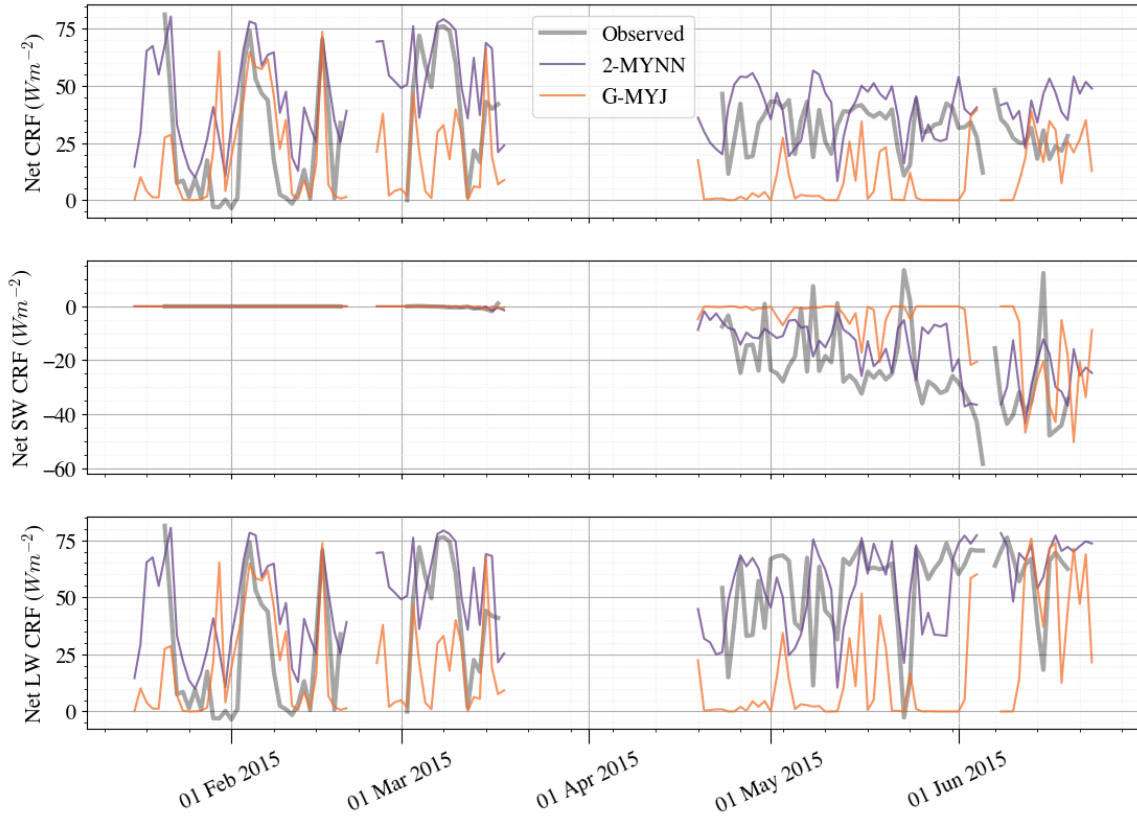


Figure 4.9: 6-hourly net (top), longwave (bottom), and shortwave (middle) CRF from the N-ICE measurements (gray) and modeled by Polar WRF using the Morrison Two-Moment CM scheme with MYNN PBL scheme (purple) and the Goddard CM scheme with the MYJ PBL scheme (orange).

layer (PBL) scheme (2-MYNN, purple) had the lowest biases in latent and sensible heat fluxes in the winter. In the spring, the run with the Goddard CM scheme and Mellor–Yamada–Janjic PBL scheme (G-MYJ, orange) had the lowest biases in latent and sensible heat fluxes and net shortwave flux. For more details about the model setup and the strengths/weaknesses of the PBL and CM schemes, see Chapter 3.

The 2-MYNN simulation slightly overestimates CRF throughout much of the N-ICE period. In the winter, CRF is estimated well during times when high CRF values

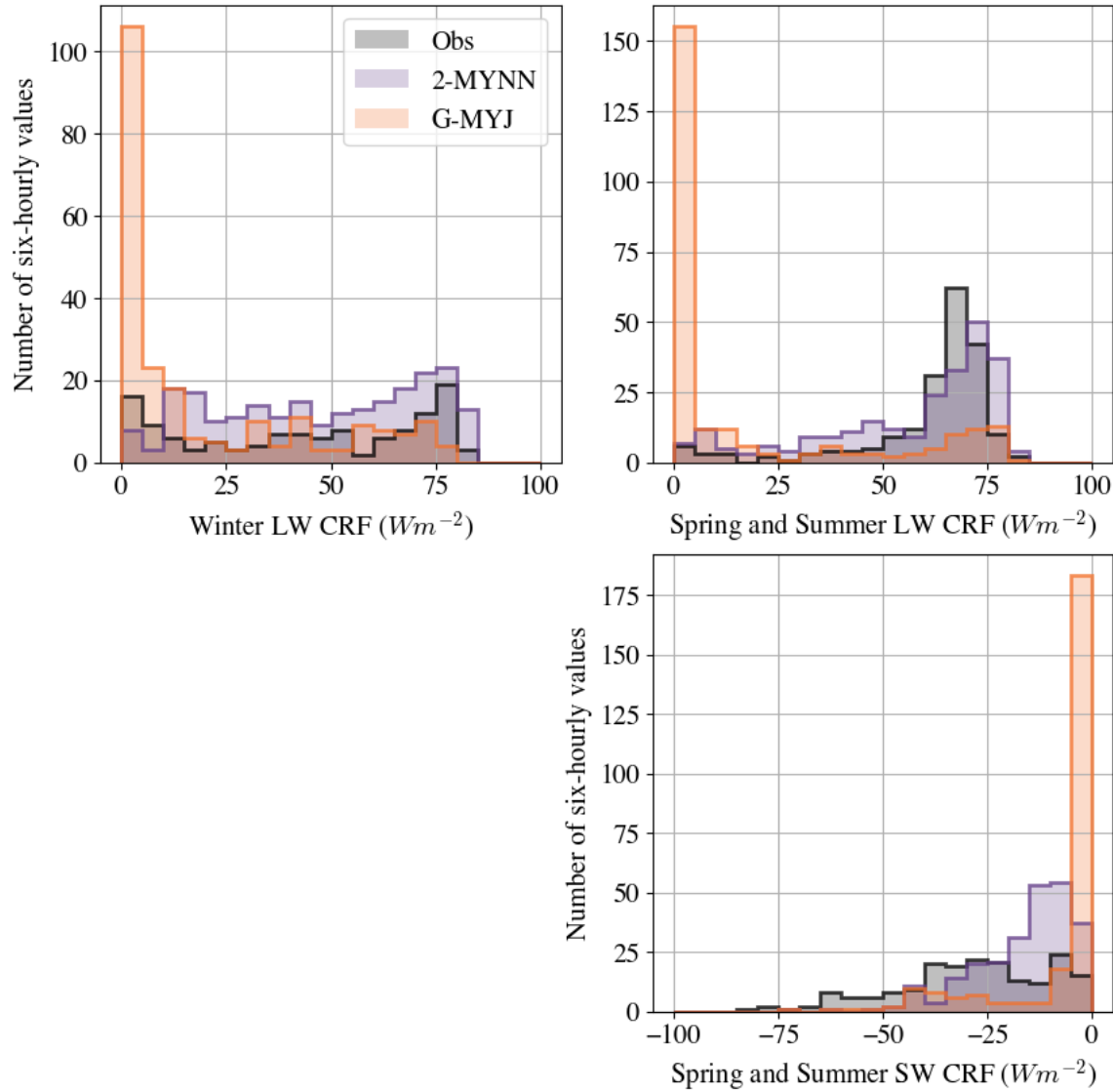


Figure 4.10: Longwave (top), and shortwave (bottom) CRF in the winter (left) and spring/summer (right). N-ICE measurements are shown in black. Polar WRF simulated CRF from the Morrison Bulk Two-Moment CM scheme with MYNN PBL scheme (2-MYNN) and the Goddard CM scheme with the MYJ PBL scheme (G-MYJ) are shown in purple and orange.

were observed. The model does well with the low, thick clouds that produce high CRF values in the winter. However, in the spring and summer, this scheme underestimates the compensating shortwave CRF, resulting in net CRF values that are too high, regardless of how well the 2-MYNN scheme is reproducing the longwave forcing. The distribution of net longwave forcing can be seen in the top panels of Figure 4.10 and the shortwave in the bottom panel.

The 2-MYNN scheme had the lowest longwave bias in the spring. However, the net shortwave bias was the largest with this scheme. Longwave CRF from 2-MYNN did capture some CRF peaks well in the spring, and much of the error in spring CRF is a result of the shortwave CRF. This indicates clouds at N-ICE had a greater influence on the shortwave radiation than those simulated by Polar WRF with the 2-MYNN configuration.

The G-MYJ simulation had the lowest sensible and latent heat flux biases in spring, but greatly underestimates all components of CRF. The G-MYJ simulation displays large net longwave biases. In the spring, the G-MYJ simulation significantly underestimated CRF until the last floe in June. Near the end of June, both model runs began to produce larger CRF values in both the longwave and shortwave. While this increase in longwave and shortwave CRF also increased the net CRF in the 2-MYNN scheme, it balances out to be around 25 Wm^{-2} of net CRF in the G-MYJ scheme, which is similar to CRF values from the N-ICE measurements.

Even the schemes with the lowest biases in the turbulent fluxes simulate large inaccuracies in the modeled CRF. The modeled clouds are not producing the CRF required to replicate the measurements, indicating that the cloud properties are not simulated correctly. This could be caused by some combination of these properties:

1) too few clouds, 2) clouds are not warm enough, or 3) the clouds are not optically thick enough. It is most likely that the cloud fraction is too low because the shortwave flux during the transition from winter to spring is low, especially in the G-MYJ simulation. Figure 3.7 in Chapter 3 supports this interpretation, showing cloud fraction in the G-MYJ simulation was consistently lower than the measurements, especially in the spring. This figure also shows that the 2-MYNN scheme underestimated cloud fraction throughout the entire spring period.

4.6 Conclusions

The N-ICE field campaign observed unique Arctic atmospheric conditions during the transition from winter to summer over first-year sea ice. As the Arctic continues to move toward ice-free conditions in summer, the need for observations over first-year sea ice becomes increasingly important. There is a need for sufficient measurements to provide valuable comparison datasets for models. Often, models' weaknesses lie in cloud properties. Particularly in the polar regions, where we have fewer observations for validation, the cloud properties are often unknown.

This study aimed to characterize the macrophysical and microphysical properties of the clouds at N-ICE. The cloud phase, base height, and base temperature were explored extensively both for the entire experiment, seasonally, and for a particularly uniquely strong storm-period.

In the winter, the cloudy and clear conditions described in Graham et al. (2017a) were clearly visible in the peaks in the distribution of longwave CRF around 0 W m^{-2} (clear) and again around 75 W m^{-2} (cloudy). Spring longwave CRF showed similar results, with an obvious clear and cloudy state. Shortwave CRF in the spring was negative for a lot of the season, with a few positive values in June. Spring and summer

were characterized by low, primarily water clouds. Average cloud base height for each month in the spring and summer was below 3 km . Winter cloud base heights were higher, particularly those observed in January, when the average cloud base height was over 6 km above the surface.

In winter, the cloud base height and temperature correlated with the CRF. Lower cloud base temperature generally indicated lower CRF values, as the clouds were higher, likely more optically thin, and colder. In the spring, the compensating effects of the LW and SW CRF can be seen. Lower cloud base heights produced increased longwave CRF (as warmer clouds increase LW radiation to the surface), but increased the magnitude of the (negative) shortwave CRF. The longwave influence dominated the CRF for the entire N-ICE experiment.

Modeled CRF values from the polar WRF model were compared to CRF observations from N-ICE. Longwave CRF was underestimated by the model simulation using the G-MYJ configuration, with the most notable differences occurring during the spring. The 2-MYNN run also underestimated SW CRF, resulting in a significant underestimation of net CRF, regardless of this model performing well with latent and sensible heat flux calculations. The 2-MYNN run, the simulation with the lowest wintertime biases in chapter 3, produced LW CRF values similar to those observed at N-ICE. However, the SW CRF was underestimated by this simulation, resulting in a larger net CRF than was observed. In the winter, the 2-MYNN accurately predicts high CRF values but overpredicts low CRF values. In the spring, the opposite is true, higher CRF values are overestimated by the model, but lower CRF value clouds are relatively well modeled.

CHAPTER FIVE

LATENT AND SENSIBLE HEAT FLUX CALCULATIONS OVER FIRST-YEAR SEA ICE

A recent review of the latent and sensible heat flux accuracies over the period 2000–2007 highlights significant differences between several gridded products over ocean, where root-mean-squared differences between the multi-product ensemble and data at more than 200 moorings reached up to 25 W m^{-2} for latent heat and 5 W m^{-2} for sensible heat. This uncertainty stems from the retrieval of flux-relevant meteorological variables, as well as from differences in the flux parametrizations.

- IPCC Sixth Assessment Report, August 2021

5.1 Introduction

It is important to fully understand the surface energy budget over sea ice because small changes in radiative and/or turbulent fluxes enact feedbacks that can result in significant climate impacts. Reductions in sea ice have been found to amplify the impacts of global warming (Wunderling et al., 2020; Arias et al., 2021). Differences in the surface features and atmospheric conditions present challenges for modeling the surface energy and water budgets (Wang & Bras, 2009).

$$R = Q_{net} + H_s + H_l \quad (5.1)$$

The energy budget of the snow-sea-ice slab can be seen in Eq. 5.1 (hereafter referred to as the surface energy budget). The net radiative flux, Q_{net} , is the combination of the shortwave and longwave radiation (downward - upward), R is the residual, a combination of the ocean heat flux and the surface heat storage (Walden

et al., 2017a). The turbulent fluxes, H_s and H_l , are the sensible and latent heat fluxes and are the focus of this chapter. Physically, the sensible heat flux represents conduction between the atmosphere and the surface that is driven by the temperature gradient near the surface. As defined here, positive sensible heat flux represents energy into the surface, which would occur when the near-surface atmospheric temperature is warmer than the surface. This is often the case during the winter when either near-surface temperature inversions occur or when warm air is advected over the frozen surface. Negative sensible heat flux values represent energy lost by the surface, which occurs when the surface is warmer than the overlying atmosphere. Latent heat flux is the heat associated with a phase change; positive latent heat flux is representative of deposition, condensation, or freezing at the surface, and negative latent heat occurs during sublimation, evaporation, or melting.

Some components of the surface energy budget, such as shortwave and longwave radiation, can be measured directly with radiometers. The sensible and latent heat flux, however, are more difficult to measure. A common approach is to use the eddy covariance (EC) technique. This is explained briefly by Walden et al. (2017a). First, high-frequency measurements of temperature, three-dimensional wind speed, and water vapor concentration are made above the surface. LiCor's EddyPro 7 (LI-COR, 2021) software is then used to process these measurements. The program conducts calibration and filtering on the raw measurements, then calculates the sensible and latent heat fluxes by analyzing the covariance of vertical wind with temperature or water vapor. The high-frequency measurements were made by a Campbell Scientific CSAT3 sonic anemometer and CPEC200 gas analyzer operated by researchers from the Norwegian Polar Institute.

The Norwegian Young Sea Ice Field Campaign (N-ICE) in 2015 and the Surface Heat Budget of the Arctic Ocean Experiment (SHEBA) in 1998 both deployed EC systems, radiometers, and meteorological towers over sea ice in the Arctic ocean. SHEBA took place over older, multi-year sea ice, and the data collected has been processed both using EC theory and using other methods not requiring the EC system. N-ICE took place over young, first-year sea ice. A description of the turbulent fluxes observed by the EC system and the radiation measured by radiometers can be found in Walden et al. (2017a), which describes the observed surface energy budget at N-ICE.

5.2 Calculating Sensible and Latent Heat Flux

In this section, the measured turbulent fluxes are compared to two methods of calculating sensible and latent heat flux: a bulk flux algorithm based on Monin-Obukhov similarity theory (Foken & Napo, 2008) and the Maximum Entropy Production (MEP) method (Zhang et al., 2021; Wang et al., 2014; Wang & Bras, 2009). Both methods estimate flux without covariance measurements and instead utilize values more commonly observed at weather stations. The bulk flux algorithm is based on Monin-Obukhov similarity theory. The MEP equation is based on the conservation of energy; a system will always move toward thermodynamic equilibrium, a state of maximum entropy dissipation (Wang & Bras, 2009; Wang et al., 2014). The following subsection will give details about how the stability is used to calculate the stability-dependant scaling parameters required by equations for both the bulk flux algorithm and the MEP method.

5.2.1 Bulk Flux Algorithm

The bulk flux algorithms are most commonly used for estimating turbulent fluxes Reeves Eyre et al. (2021) in models because they are relatively easy to calculate (depend only on meteorological variables) and are computationally efficient. The bulk flux algorithm formulations of sensible and latent heat flux used here are shown in Eq. 5.2 and 5.3 and are referred to as the “bulk flux algorithm” for the rest of this paper.

$$H_s = \rho c_p C_{Hz} w [\theta_s - \theta_z] \quad (5.2)$$

$$H_l = \rho L_v C_{Ez} w [q_s - q_z] \quad (5.3)$$

Sensible and latent heat flux depend on measurements of wind speed (w), potential temperature (θ_s and θ_z), and specific humidity (q_s and q_z) at the surface and a reference height, (for this case 2 m and 4 m). In these equations, ρ is the density of the air, c_p the specific heat of air, L_v the latent heat of vaporization, and C_{Hz} and C_{Ez} are the heat and moisture exchange bulk transfer coefficients (Foken & Napo, 2008; Andreas et al., 2003). Eq. 5.5 and 5.4 are the generally accepted functions for estimating these coefficients (Foken & Napo, 2008). Here, κ is the von Kármán constant and is equal to 0.4.

$$C_{Ez} = \frac{\kappa C_D^{\frac{1}{2}}}{[\ln(\frac{z}{z_0}) - \varphi_h]} \quad (5.4)$$

$$C_{Hz} = \kappa^2 \left[\ln \left(\frac{z}{z_0} \right) - \varphi_m \right]^{-1} \left[\ln \left(\frac{z}{z_0} \right) - \varphi_h \right]^{-1} \quad (5.5)$$

These equations are functions of φ_m and φ_h , the scaling parameters, which depend

on the surface stability; various formulations for these are discussed in section 5.2.3. They also require estimations of the drag coefficient (C_D) and the roughness length (z_0).

5.2.2 Maximum Entropy Production Method

The MEP method was developed to accurately estimate surface fluxes while limiting the number of measurement levels required. This method is based on the principle of maximum entropy and Bayesian probability theory from statistical mechanics (Wang et al., 2014). These equations are based on the theory that any system will move toward thermodynamic equilibrium, which is a state of maximum entropy production. Equations 5.6 and 5.7 are the MEP formulations for sensible (H_s) and latent (H_l) heat fluxes, respectively.

$$\left[1 + B(\theta) + \frac{B(\theta_{pc})}{\theta_{pc}} \frac{I_{wsi}}{I_0} |H_s|^{-\frac{1}{6}} \right] H_s = Q_{net} \quad (5.6)$$

$$H_l = B(\theta_{pc}) H_s \quad (5.7)$$

A constant (B) based on the phase change parameter (θ_{pc} , defined in (Wang & Bras, 2011) as Eq. 9), is defined in Eq. 5.8 and is required by both the sensible and latent heat flux calculations. Calculations of sensible and latent heat flux using this method require estimations of the thermal conductivity (Wang et al., 2014) of the surface. The thermal inertia parameter of the sea ice (I_{wsi} , Eq. 5.9) used in the MEP equation requires the air density (ρ), specific heat of dry air (c_p), and thermal conductivity of the surface (λ). Merkouriadi et al. (2017) found that the thermal conductivity of snow on sea ice during N-ICE2015 was much lower than those used in many modeling studies, so the thermal inertia parameter needs to be calculated

for our location using an appropriate thermal conductivity value.

$$B(\theta_{pc}) = 6 \left(\sqrt{1 + \frac{11}{36}\theta_{pc}} - 1 \right) \quad (5.8)$$

$$I_{wsi} = \sqrt{\rho c_p \lambda} \quad (5.9)$$

$$I_0 = \rho c_p \sqrt{C_{Ez} \kappa z} \left(C_{Hz} \frac{\kappa z g}{\rho c_p T_r} \right)^{\frac{1}{6}} \quad (5.10)$$

I_0 can be calculated by 5.10. This value is called “the apparent thermal inertia of air” by Wang & Bras (2009). It depends on the heat and moisture exchange bulk transfer coefficients (C_{hz} and C_{ez}), which are defined in the previous section. In this equation, κ is the Kármán constant, z is the measurement height (2 m for this study), g is the gravitational constant, and T_r is a reference temperature of 300 K.

This model has been used to calculate fluxes during SHEBA with some degree of accuracy, proving its ability to perform in the polar regions (Wang et al., 2014).

5.2.3 Surface Stability

Some commonly accepted sets of equations for the empirical scaling equations (φ_h and φ_m for C_{Hz} and C_{Ez}) are shown in Table 5.1. These equations use the surface-layer stability parameter (Eq. 5.11) to determine surface stability. These values depend on the Obukhov length (L , Eq. 5.12). Obukhov length requires estimations of the covariance of the vertical velocity and virtual potential temperature ($\overline{w'\theta'_v}$), friction velocity (u_*), and the virtual potential temperature (θ_v).

$$\zeta = \frac{z}{L} \quad (5.11)$$

$$L = -\frac{u_*^3}{\kappa \frac{g}{\theta_s} \overline{w' \theta'_v}} \quad (5.12)$$

Positive surface-layer stability parameter numbers indicate stable conditions and negative indicate unstable conditions. Some studies find that using an adjusted von Kármán constant (κ) can improve calculations (Businger et al., 1971; Zilitinkevitsch & Tschalikov, 1968; Dyer & Hicks, 1970; Foken & Napo, 2008), but changing this variable is outside the scope of this study, so only formulations using $\kappa = 0.4$ to calculate ζ are included in Table 5.1.

Each of the equations shown in the Table 5.1 have different ranges of stability to which they can be applied. These are formulated empirically, meaning they depend on measurements and are useful only under similar conditions (Stull, 1988; Foken & Napo, 2008). These equations were selected as they are those listed by Foken & Napo (2008) in the book *Micrometeorology* for use using the von Kármán constant equal to 0.4. One equation, the Andreas et al. (2010) formulation, was selected despite it being absent from the list in Foken & Napo (2008). Many of these equations, with the exception of Andreas et al. (2010), were created under conditions observed in mid-latitudes. Andreas et al. (2010), on the other hand, used results from the SHEBA field experiment to tune the relationships based on the Businger-Dyer-Pandolfo (BDP) relationship (Eq. 5.13 and 5.14). This relationship is generally used for neutral and unstable conditions (Foken & Napo, 2008), so it requires tuning for other locations. Additionally, the MM5 Similarity Surface-layer scheme in WRF (Paulson, 1970) used in Chapter 3 bases its estimation of these scaling parameters on this relationship. Unlike many of the equations in Table 5.1, the BDP relationship requires an extra variable, γ , which is defined empirically for each location.

Table 5.1: Scaling parameter equations from Micrometeorology (Foken & Napo, 2008) for the universal functions of momentum and heat. 'BDP' represents the Businger-Dyer-Pandolfo relationship, as seen in Eq. 5.14 and 5.13. (Foken & Napo, 2008).

| Author | Equations |
|---|--|
| Swainbank (Foken & Napo, 2008) | $\varphi_m = \begin{cases} 0.613(-\zeta)^{-0.2} & -0.1 \geq \zeta \geq -2 \\ 0.226(-1/L)^{-0.44} & -0.1 \geq \zeta \geq -2 \end{cases}$ |
| Tschalikov (Foken & Napo, 2008) | $\varphi_m = \begin{cases} 1 + 7.74\zeta & \zeta \geq 0.04 \\ 1 + 5.17\zeta & \zeta \geq 0.04 \end{cases}$ |
| Zilitinkevich and Tschalikov (Zilitinkevitsch & Tschalikov, 1968) | $\varphi_m = \begin{cases} 1 + 1.38\zeta & -0.15 < \zeta < 0 \\ 0.42(-\zeta)^{1/3} & -1.2 < \zeta < -0.15 \\ 1 + 9.4\zeta & 0 < \zeta \end{cases}$ $\varphi_H = \begin{cases} 1 + 1.31\zeta & -0.15 < \zeta < 0 \\ 0.41(-\zeta)^{-1/3} & -1.2 < \zeta < -0.15 \\ 0.95 + 8.9\zeta & 0 < \zeta \end{cases}$ |
| Businger et al. (Businger et al., 1971) | $\varphi_m \begin{cases} (1 - 19.3\zeta)^{-1/4} & -2 < \zeta < 0 \\ 1 + 6\zeta & 0 < \zeta < 1 \end{cases}$ $\varphi_H \begin{cases} 0.95(1 - 11.6\zeta)^{-1/2} & -2 < \zeta < 0 \\ 0.95 + 7.8\zeta & 0 < \zeta < 1 \end{cases}$ |
| Dyer (Dyer, 1974) | $\varphi_m \begin{cases} (1 - 15.2\zeta)^{-1/2} & -1 < \zeta < 0 \\ 1 + 4.8\zeta & 0 < \zeta \end{cases}$ |
| Skeib (Foken & Kretschmer, 1990) | $\varphi_m = \begin{cases} 1 & -0.0625 < \zeta < 0.125 \\ (\frac{\zeta}{-0.0625})^{-1/4} & -2 < \zeta < -0.0625 \\ \frac{\zeta}{0.125} & 0.125 < \zeta < 2 \end{cases}$ $\varphi_H = \begin{cases} 1 & -0.0625 < \zeta < 0.125 \\ 0.95(\frac{\zeta}{-0.0625})^{-1/2} & -2 < \zeta < -0.0625 \\ 0.95(\frac{\zeta}{0.125})^2 & 0.125 < \zeta < 2 \end{cases}$ |
| Gavrilov and Petrov (Gavrilov & Petrov, 1981) | $\varphi_m = \begin{cases} (1 - 8\zeta)^{-1/3} & \zeta < 0 \\ 1 + 5\zeta & 0 < \zeta \end{cases}$ $\varphi_H = \begin{cases} 0.65 \left[(1 - 35\zeta)^{-1/2} + \frac{0.25}{1+8(\zeta)^2} \right] & \zeta < 0 \\ 0.9 + 6\zeta & 0 < \zeta \end{cases}$ |
| Dyer and Bradley (Dyer & Bradley, 1982) | $\varphi_m = \begin{cases} (1 - 28\zeta)^{-1/4} & \zeta < 0 \\ (1 - 14\zeta)^{-1/2} & \zeta < 0 \end{cases}$ |
| Beljaars and Holtslag (Beljaars & Holtslag, 1991) | $\varphi_m = \begin{cases} 1 + \zeta + \frac{2}{3}\zeta(6 - 0.35\zeta)e^{-0.35\zeta} & \zeta < 0 \\ 1 + \zeta + (1 + \frac{2}{3}\zeta)^{1/2}(6 - 0.35\zeta)e^{-0.35\zeta} & \zeta < 0 \end{cases}$ |
| Handorf et al. (Handorf et al., 1999) | $\varphi_m = \begin{cases} 1 + 5\zeta & 0 < \zeta < 0.6 \\ 4 & \zeta > 0.6 \end{cases}$ $\varphi_H = \begin{cases} 1 + 5\zeta & 0 < \zeta < 0.6 \\ 4 & \zeta > 0.6 \end{cases}$ |
| Andreas et al. (Andreas et al., 2009) | $\varphi_m = \begin{cases} BDP(\gamma = 16) & \zeta < 0 \\ -5z/L & \zeta \geq 0 \end{cases}$ $\varphi_H = \begin{cases} \varphi_m^2 & \zeta < 0 \\ \varphi_m & \zeta \geq 0 \end{cases}$ |

$$\varphi_m(\zeta) = (1 + \gamma\zeta)^{-1/4} \quad (5.13)$$

$$\varphi_H = \begin{cases} \varphi_m & \zeta \geq 0 \\ \varphi_m^2 & \zeta < 0 \end{cases} \quad (5.14)$$

The empirically defined γ value seen in Eq. 5.13 (Paulson, 1970; Chen & Dudhia, 2001) has been calculated for N-ICE. This value was highly variable, making the selection of one number difficult. The mean γ value back-calculated for N-ICE was around -5 with a standard deviation of 41. At SHEBA, a value of 16 was calculated for γ . Because of the large range of calculated γ values at N-ICE, it is difficult to capture the fluxes well by selecting just one value.

The polar regions experience stronger surface inversions than in lower-latitude locations, and sometimes the stability seen in these locations is too strongly stable for other empirical stability functions to apply. Or if they do claim to be valid under those conditions, they may have little validation for large Obukhov lengths. Under these strongly stable conditions, some methods of estimating the scaling parameters break down. However, these are still the commonly selected scaling parameters and are applied over stable conditions regardless of their design. This paper will use the equations in 5.1 with the bulk flux algorithm and MEP equations to calculate latent and sensible heat flux over first-year sea ice. The best relationship and flux equations for use at N-ICE will be selected.

5.3 Observations

Observations from N-ICE were used to calculate heat fluxes. Atmospheric measurements of temperature, wind speed, and atmospheric water vapor at N-ICE were

measured at three levels (2, 4, and 10 m) from a meteorological tower constructed on first-year sea ice (Walden et al., 2017a). The pressure was reported at sea level, and for this study was used to calculate the pressure at 2, 4, and 10 m using the barometric equation (Lente & Ősz, 2020). N-ICE took place in the Arctic Ocean north of Svalbard from January to June 2015. More information about this field campaign can be found in Chapter 2.

Moisture was measured and reported as relative humidity and was converted to saturation vapor pressure and specific humidity using the Clausius-Clapeyron equation (Iribarne & Godson, 1981) along with the temperature at the corresponding tower height. The bulk algorithm requires two levels of temperature and specific humidity, but the MEP formulation only requires one level of temperature and specific humidity, and the surface net radiation, making it applicable for experiments that acquired measurements at only a single height. All height levels of relative humidity were converted to specific humidity so each measurement level could be used in the bulk algorithm for comparison.

5.4 Results and Discussion

5.4.1 Stability Coefficients

The stability at N-ICE was calculated using Eq. 5.11 and observations from the meteorological tower. Covariance measurements were also made for the entire time period, so we have measured Obukhov lengths for validation from EddyPro processing. Figure 5.1 shows the Obukhov length (L) calculated with 5.12 by EddyPro for the entire N-ICE study period using 20Hz measurements of wind, temperature, and atmospheric moisture measured from the Eddy Coviarance system. This initial

comparison was done to determine if any sources of error could be attributed to errors in the Obukhov length. The EddyPro estimation of Obukhov length produced slightly more negative (unstable) values than those calculated directly using Eq. 5.12.

The Obukhov length depends on the friction velocity, and the surface below N-ICE is first-year sea ice, a relatively flat surface with limited sources of mechanical turbulence. Friction velocity is a measure of the amount of wind shear (Stull, 1988). The mean friction velocity at N-ICE calculated using meteorological tower observations was 0.24 m s^{-1} with a standard deviation of approximately 0.1 m s^{-1} . Friction velocity values from Eddypro were around 0.2 m s^{-1} , with a maximum of about 1 m s^{-1} . The results from EddyPro appear to represent a surface with more wind shear than those calculated independently of EddyPro.

Table 5.2 shows the mean bias when using the MEP and bulk flux methods to calculate surface fluxes relative to the EddyPro results. Each source in the “Author” column corresponds to equations in Table 5.1. Each has a different number of hourly measurements included because each is applicable to specific ranges in stability. For example. Swainbank (Foken & Napo, 2008) is only valid for surface-layer stability

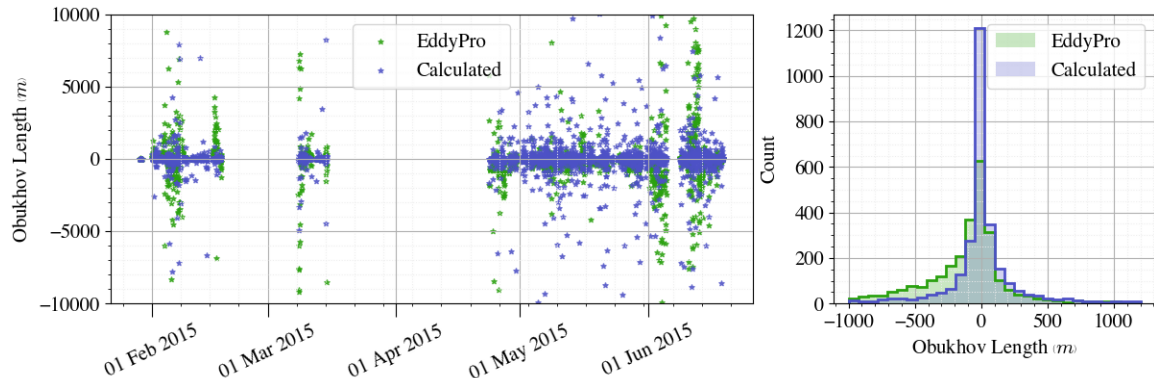


Figure 5.1: The Obukhov length measured during N-ICE and processed using EddyPro (green) and calculated using Eq. 5.12 (blue).

Table 5.2: Mean bias of sensible and latent heat flux calculations using each scaling equation listed in Table 5.1 for both the MEP equations and the bulk flux algorithm. The number of hourly measurements used and the applicable ranges are shown in the rightmost columns.

| Author | Mean Bias (Mean Value) (Wm^{-2}) | | | | N | Stability Range |
|------------------------------|--------------------------------------|--------------|-------------|---------------|------|---------------------------|
| | MEP | | Bulk | | | |
| | H_l | H_s | H_l | H_s | | |
| Swainbank | 1.8 (0.1) | -3.0 (8.3) | -0.5 (0.5) | -14.4 (8.8) | 50 | $-2 \leq \zeta \leq -0.1$ |
| Tschalikov | -1.3 (-0.0) | -7.4 (-17.4) | 0.7 (-0.1) | -49.2 (-17.4) | 312 | $0.04 \leq \zeta$ |
| Zilitinkevich and Tschalikov | 1.0 (0.1) | -3.2 (0.6) | 0.1 (0.0) | -1.7 (2.0) | 1499 | $-1.2 < \zeta$ |
| Businger et al. | 1.0 (0.1) | -2.8 (0.8) | 0.1 (0.0) | 0.3 (2.1) | 1475 | $-2 \leq \zeta$ |
| Dyer | 1.2 (0.1) | -2.3 (2.6) | 0.0 (0.0) | 6.9 (3.7) | 1277 | $-1 \leq \zeta$ |
| Skeib | 1.0 (0.1) | -2.4 (-0.1) | 0.1 (0.0) | 4.4 (1.4) | 1422 | $-2 \leq \zeta \leq 2$ |
| Gavrilov and Petrov | 0.9 (0.1) | -3.3 (0.6) | 0.1 (0.0) | -1.0 (2.0) | 1518 | all ζ |
| Dyer and Bradley | 1.7 (0.1) | -6.3 (10.5) | -0.5 (0.1) | 12.2 (10.8) | 814 | $0 \leq \zeta$ |
| Beljaars and Holtslag | -0.3 (0.0) | -0.3 (-16.0) | -2.7 (-0.0) | 137.0 (-15.0) | 814 | $0 \leq \zeta$ |
| Handorf et al. | -0.4 (0.0) | 2.6 (-16.0) | 0.7 (-0.0) | -29.5 (-14.9) | 814 | $0 \leq \zeta$ |
| Andreas et al. | 0.4 (0.1) | 0.9 (0.6) | 0.0 (0.0) | 4.3 (2.0) | 1518 | all ζ |

parameter values between -0.1 and -2, indicating this is only valid for unstable conditions, which we see rarely in the polar regions. So this formulation uses only a small number of observations for comparison. Andreas et al. (2003), on the other hand, was created using the SHEBA observations and includes all stability values. The equations created by Andreas et al. (2003) had low biases relative to other equations including strong stability.

Using the bulk flux algorithm resulted in similar errors for latent heat flux regardless of the scaling parameter relationship used with the exception of the Swainbank and Tschalikov (Foken & Napo, 2008) formulations, which had a significantly lower

Table 5.3: Mean absolute error of sensible and latent heat flux calculations using each scaling equation listed in Table 5.1 for both the MEP equations and the bulk flux algorithm.

| Author | Mean Absolute Error (Wm^{-2}) | | | |
|------------------------------|-----------------------------------|-------|-------|-------|
| | MEP | | Bulk | |
| | H_l | H_s | H_l | H_s |
| Swainbank | 1.9 | 5.7 | 1.0 | 30.2 |
| Tschalikov | 1.6 | 11.3 | 1.0 | 73.4 |
| Zilitinkevich and Tschalikov | 1.9 | 10.4 | 1.9 | 28.4 |
| Businger et al. | 1.9 | 10.0 | 1.9 | 26.9 |
| Dyer | 1.9 | 9.9 | 2.1 | 22.0 |
| Skeib | 2.0 | 10.5 | 2.0 | 25.2 |
| Gavrilov and Petrov | 1.7 | 10.2 | 1.8 | 25.7 |
| Dyer and Bradley | 2.0 | 8.6 | 2.1 | 18.0 |
| Beljaars and Holtslag | 2.5 | 15.5 | 7.7 | 187.6 |
| Handorf et al. | 1.7 | 12.6 | 1.6 | 46.2 |
| Andreas et al. | 0.7 | 12.4 | 1.6 | 14.8 |

and higher mean bias, respectively. While Swainbank (Foken & Napo, 2008) did have the lowest mean bias for the latent heat flux and one of the lowest for the sensible heat flux, it was not selected for use because of the low number of stability conditions over which it can be used.

Due to its wide range of stability values and its improved performance for latent heat flux, the Andreas et al. (2010) formulation was used for the final analysis of both the bulk flux equation and the MEP equation. The MEP equation typically uses the relations developed by Businger et al. (1971), but for our location, the Andreas et al. (2003) formulation performed better when compared to the EddyPro measurements when calculating latent heat flux. Sensible heat flux, on the other hand,

Table 5.4: Thermal conductivity (λ) and thermal inertia (I_{wsi}) for each floe during N-ICE. Conductivity values were taken as a mean from Merkouriadi et al. (2017) (Floes 1 and 2) and Gallet et al. (2017) (Floes 3 and 4) and inertia parameters were calculated using equation 5.9.

| Floe | Thermal Conductivity ($W\ m^{-1}K^{-1}$) | Thermal Inertia ($m^{-1}K^{-1}$) |
|------|---|---------------------------------------|
| 1 | 0.183 | 314.264 |
| 2 | 0.246 | 429.650 |
| 3 | 0.193 | 280.424 |
| 4 | 0.311 | 1009.816 |

was comparable between the Andreas et al. (2003) formulation and the Businger et al. (1971) formulation.

5.4.2 Thermal Conductivity

Thermal conductivity is used in the MEP method to calculate the thermal inertia parameter, as shown in Eq. 5.9. Thermal conductivity values at N-ICE were much lower than those commonly used in models (Merkouriadi et al., 2017), so special care was taken to ensure that the thermal conductivity estimate was accurate for our conditions. Using the thermal conductivity values shown in Table 5.4 with Eq. 5.9, the thermal inertia parameter was estimated for N-ICE as shown in Table 5.4.

5.4.3 Bulk Flux Algorithm

Calculating the fluxes using the bulk flux algorithm resulted in more large positive values than was seen in the EddyPro or in the MEP results. These can be seen in Figure 5.2. In spring, the sensible heat flux is consistently over-estimated by the bulk flux algorithm, indicating that the temperature difference between the surface and

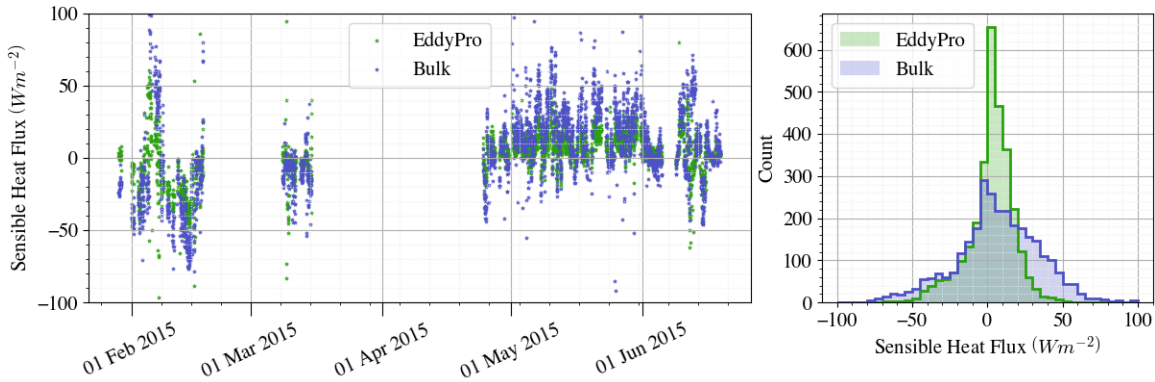


Figure 5.2: The sensible heat flux at N-ICE as calculated with EddyPro (green) and with the bulk flux algorithm method (blue).

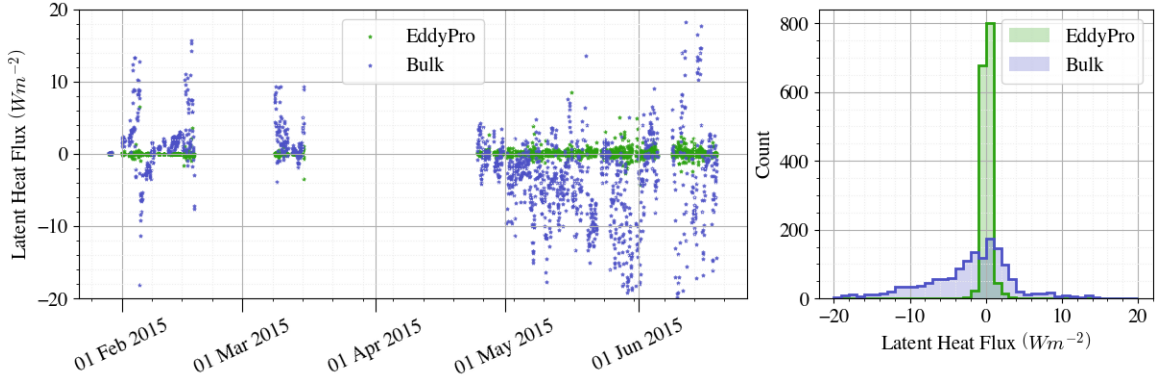


Figure 5.3: The latent heat flux at N-ICE as calculated with EddyPro (green) and with the bulk flux algorithm method (blue).

the atmosphere is too large in the calculations, and too much heat is being transferred from the surface. The latent heat fluxes, shown in Figure 5.3, were also significantly larger than the EddyPro results when using the bulk flux algorithm.

In June, there was a large decrease in the latent heat flux according to the bulk algorithm. This was mirrored by an increase in the sensible heat flux. However, this decrease (increase) in the latent heat flux (sensible heat flux) was not seen in the EddyPro results. EddyPro produced latent heat flux values consistently around zero during this time period, while the sensible heat flux became negative. This indicates

that the near-surface air was warmer than the surface and sensible heat transfer was occurring instead of a phase change. However, the bulk flux algorithm favored a phase change, likely melting, over a sensible heat flux change. At this time in the experiment, there likely was significant phase change occurring as many melt ponds were developing in the surrounding area (Walden et al., 2017a). Overall, latent heat flux values estimated by the bulk equation are more largely positive in the winter and more largely negative in the summer, indicating the bulk flux algorithm shows more melting in the spring and more freezing in the winter than the EddyPro results.

Positive latent heat flux values are, at times, almost 10 W m^{-2} greater in the bulk results than in the EddyPro results. EddyPro, once again, favors sensible heat flux changes to phase changes. However, the sensible heat flux in the bulk algorithm and in EddyPro are comparable. This indicates that EddyPro is not just favoring the heat transfer to be in the form of sensible heat flux, but it also underestimates the latent heat flux in general, even in situations when it cannot be described by an offset in the sensible heat flux.

5.4.4 Maximum Entropy Production Method

Sensible heat flux from the MEP method was calculated using Eq. 5.6. The results of this are shown in Figure 5.4. For most of the experiment, the MEP method accurately represented the sensible heat fluxes at N-ICE. In the winter, fluxes were slightly underestimated by the MEP equation, resulting in a bi-modal shape to the distribution shown on the right of the figure. In the spring, there was one occurrence lasting several days with largely negative sensible heat flux shown in the EddyPro results while the sensible heat fluxes from the MEP equation were positive.

Latent heat fluxes (Figure 5.5) were not represented as well using the MEP as

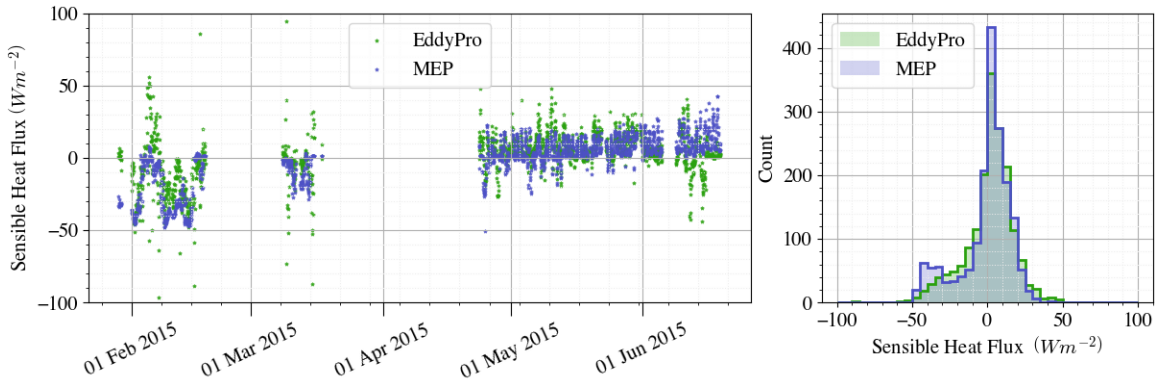


Figure 5.4: The sensible heat flux at N-ICE as calculated with EddyPro (green) and with the MEP method (blue).

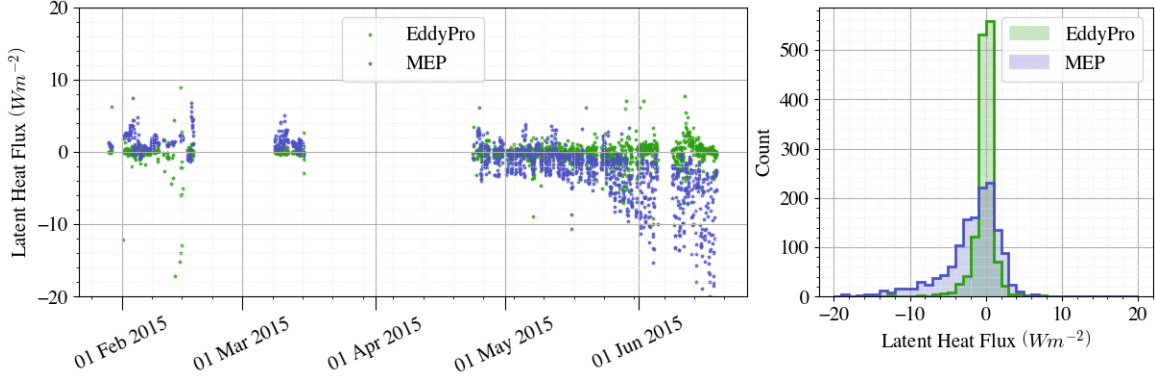


Figure 5.5: The latent heat flux at N-ICE as calculated with EddyPro (green) and with the MEP method (blue).

compared to the EddyPro results. EddyPro showed very small latent heat fluxes throughout the entire experiment. These small heat fluxes were surprising and are not captured with the MEP method. February and March values of latent heat flux are comparable between the MEP and EddyPro calculations, but during spring and entering summer, MEP values are at times $20 Wm^{-2}$ greater than those calculated by EddyPro, which are rarely greater than $10 Wm^{-2}$.

5.5 Conclusions

Sensible and latent heat flux formulations require high temporal resolution to use eddy covariance methods. Two methods of calculating sensible and latent heat flux that do not require eddy covariance measurements are explored here. The MEP method is a method utilizing thermal conductivity, net radiative flux, and stability. The bulk flux method requires measurements of moisture and temperature, wind speed, and stability at two levels near the surface. Both equations require the bulk transfer coefficients of heat and moisture, which are a function of stability and have been empirically defined for experiments over a variety of surfaces. Very few of these functions are appropriate for the strong stability conditions that often occur in polar regions. Andreas et al. (2003) developed a relationship for these functions that applies to strong stability using data from SHEBA over multi-year sea ice. This relationship was also found to be appropriate for the bulk transfer coefficients at N-ICE using both the bulk flux method and the MEP method.

The MEP method performed well when compared to the EddyPro values for both sensible and latent heat fluxes in spring and summer. In the winter, the latent heat flux values calculated by the MEP equation are much higher than those in EddyPro, indicating more phase change. The bulk method also represented the EddyPro values fairly well, although the MEP formulations seem to represent the spread of flux values better than the bulk algorithm and had the lowest mean absolute error. The latent heat flux values were also much larger than those observed during N-ICE in the bulk method. In addition to having some of the lowest biases in latent and sensible heat flux, the bulk flux algorithm also had some of the lowest mean absolute errors for turbulent fluxes, indicating that overall the MEP performed better than the bulk

method compared to the observations.

Overall, further testing is needed for the validation of the latent heat flux formulations. The latent heat flux values measured at N-ICE were much smaller than expected and smaller than those seen in other experiments, so more measurements are needed to rule out any issue with the N-ICE observations. Both sensible heat flux formulations, however, produced reasonable values over the first-year sea ice seen at N-ICE.

CHAPTER SIX

IMPROVEMENTS TO THE WEATHER RESEARCH AND FORECASTING MODEL OVER FIRST-YEAR SEA ICE

Current Arctic sea ice coverage levels (both annual and late summer) are at their lowest since at least 1850 (high confidence), and for late summer for the past 1000 years (medium confidence). Since the late 1970s, Arctic sea ice area and thickness have decreased in both summer and winter, with sea ice becoming younger, thinner and more dynamic (very high confidence).

- IPCC Sixth Assessment Report, August 2021

6.1 Introduction

Models in the polar regions have the largest uncertainties relative to other parts of the Earth (Holland & Bitz, 2003; McBean et al., 2005). Models have difficulty simulating radiation accurately during times of thick clouds. A likely reason for this is the model's inability to estimate the fraction of liquid water within the cloud (Graham et al., 2017b). A surface inversion often persists during the winter months and processes under these stable conditions are not well understood or modeled (Tastula et al., 2012). In the summer, these inversions are often elevated compared to the wintertime surface inversions (Serreze et al., 1992). Models, however, are integral for understanding the processes occurring in the polar regions, particularly the radiation. Unfortunately, few field experiments collecting data for validation exist.

Reanalysis products are often used to study Arctic climate. This poses a challenge as they are not as thoroughly verified as in other locations due to the extreme climate and harsh winter conditions preventing accurate, long-term, multi-season,

in-situ measurements. Biases in clouds result in difficulties in resolving the surface energy budget. Recent studies have shown that when compared with surface observations, reanalysis have large biases in cloud properties (liquid/ice water path, fraction). A number of field experiments have shown that mixed-phase clouds are dominant in autumn through spring in the lower levels at high latitudes (Intrieri et al., 2002; Wang & Key, 2005). Cloud micro- and macrophysics are closely tied to the surface energy budget, but cloud parameterizations are not well developed in models for the polar regions. Particularly in the Arctic, the radiative properties of clouds and how they are parameterized in models are of importance to modeling the surface energy budget.

The Norwegian Young Sea Ice Experiment (N-ICE) field campaign described in Chapter 2 was the first winter field experiment in the Arctic since the Surface Heat Budget of the Arctic (SHEBA) experiment, taking place onboard a research vessel frozen into Arctic sea ice. SHEBA's primary goals were to observe the surface energy budget, ice mass balance, and ocean-ice-atmosphere interactions in the Arctic during a year-long period from October 1997 to October 1998. Much like N-ICE, SHEBA was motivated by changes in the Arctic and the need for a better understanding of physical processes in the polar regions (Randall et al., 1998). A secondary objective of SHEBA was to improve model simulations of the Arctic for use in global climate models (Uttal et al., 2002). Both the ice-albedo feedback and the cloud-radiation feedback were extensively studied using datasets collected during this field experiment. However, this experiment occurred 18 years prior to N-ICE and in a different location of the Arctic, influenced by different synoptic conditions.

As described in Chapter 3 of this dissertation, results showed that WRF-Polar does not accurately simulate conditions observed at N-ICE, regardless of the boundary-

layer and cloud microphysics scheme selected. Chapter 4 explored the cloud radiative forcing and found that mixed-phase clouds were present throughout much of the observation period. This chapter also compared the calculated cloud radiative forcing to that observed at N-ICE and found that the cloud influence on radiation was not accurately represented in the model, particularly in the shortwave. Chapter 5 expanded on the previous chapters by looking specifically at how well equations to estimate flux do under the conditions at N-ICE. This chapter was motivated by the previous two chapters with the goal of determining if the error in the model could be reduced by improving the equations used to estimate flux. Fixing the cloud-induced error in the latent and sensible heat flux equations is impossible without first knowing how much error the equation itself introduces when the correct radiation is input.

This chapter focuses on improving two parts of the model: the use of more appropriate surface properties for thin sea ice and the equations used to estimate flux in the land surface model. Two separate sensitivity studies are presented here. The first explores the sensitivity of surface properties by changing values within a lookup table used by the WRF model related to the land surface. This study uses the N-ICE observations to select improved values for thin sea ice. The second sensitivity study uses the turbulent flux equations described in Chapter 5 to compare different methods for estimating sensible and latent heat fluxes. This chapter concludes by making recommendations as to which flux equations perform the best for simulations over young, thin sea ice.

6.2 Methods

The idealized version of the Weather Research and Forecasting model (Skamarock et al., 2019) was used to test the sensitivity of the model to changes in the set of

parameters found in the model’s land use table, LANDUSE.TBL. The idealized version of WRF is different from the “real” version used in Chapter 3 and in forecasts. The idealized version simplifies the model by removing the effects of advection and topography. Idealized model simulations are used only in research as they create an “idealized” atmosphere at a point in space. These simulations are not as computationally expensive or as time-consuming as running the full WRF model and are used to isolate specific parts of the model for sensitivity testing (Guide, 2019).

The LANDUSE.TBL file is one of three tables used in WRF to set constants. This file specifies constants that pertain to the surface-atmosphere interface within the model, including the surface albedo, surface moisture availability, surface emissivity, surface roughness, thermal inertia constant, snow cover effect, and surface heat capacity. There are different “sections” within this table with values estimated or calculated from differing data sources. Much like choosing different physical schemes based on expected conditions, these sections each have sets of values that were determined from various experiments, and the sections typically specify values for summer and winter separately.

The values in this table are generally empirically derived or directly measured from field experiments. The classification for sea ice is very general as it encompasses all permanent or seasonal snow and ice surfaces and uses one set value for each variable defined in this table for all snow surface conditions. The only exception to this is the albedo. The user has the option to specify the albedo in the file used to start the model. However, doing this will only specify one albedo value. The LANDUSE.TBL values generally give different values for summer and winter, so there is an advantage to letting LANDUSE.TBL set these values during long runs.

Table 6.1: Current settings for snow and ice in the LANDUSE.TBL file used by WRF.

| Section | Season | Albedo (%) | Surface Heat Capacity ($Jm^{-3}K^{-1}$) | Roughness Length (m) | Category |
|---------------------------------|--------|------------|---|----------------------|------------------------|
| OLD | Summer | 55 | 9×10^{25} | 5 | Permanent Ice |
| | Winter | 70 | 9×10^{25} | 5 | |
| USGS | Summer | 55 | 9×10^{25} | .1 | Snow or Ice |
| | Winter | 70 | 9×10^{25} | .1 | |
| MODIFIED IGBP MODIS NOAH | Summer | 55 | 9×10^{25} | .1 | Snow or Ice |
| | Winter | 70 | 9×10^{25} | .1 | |
| SiB | Summer | 55 | 9×10^{25} | 5 | Ice Cap and Glacier |
| | Winter | 70 | 9×10^{25} | 5 | |
| MODIS | Summer | 55 | 9×10^{25} | 1 | Snow and Ice |
| | Winter | 55 | 9×10^{25} | 1 | |
| SSIB | Summer | 55 | 9×10^{25} | .1 | Snow or Ice |
| | Winter | 70 | 9×10^{25} | .1 | |
| NLCD40 | Summer | 60 | 9×10^{25} | 1.2 | Permanent Snow and Ice |
| | Winter | 60 | 9×10^{25} | 1.2 | |
| LW12 | All | 70 | 9×10^{25} | 5 | Snow and Ice |

Table 6.1 shows all sections in the LANDUSE.TBL file for any type of snow or ice surface. This table does not include the surface moisture availability, the thermal inertia constant, the surface emissivity, or the snow cover effect, as these were held constant at 95%, 5, 95, and 0, respectively. Snow cover effect for this land type is always zero, as the surface is already assumed to be snow covered. These have not been included in this table as they are not the focus of this study and were kept constant. The section of this table that the model reads is specified within the model setup file. Previous modeling studies (Chapter 3) used the USGS section of this table,

Table 6.2: Average albedo measured at N-ICE. Floe 1 is not included as albedo was calculated using shortwave radiation measurements, and the sun had not yet risen on Floe 1.

| Floe | Albedo (%) |
|------|------------|
| 2 | 86 |
| 3 | 82 |
| 4 | 78 |

so this study also uses this section.

6.2.1 Setting Surface Parameters

Albedo

Albedo values specified in Table 6.1 do not exceed 70%, but even the lowest albedos measured at N-ICE were above 70%. Increasing the albedo would increase the amount of shortwave radiation being reflected away from the surface, changing the shortwave energy balance. In addition, less energy is being absorbed into the surface than is occurring in the model. This could result in errors elsewhere (for example, in the latent heat flux) as the energy budget in the model attempts to balance itself. The albedo values in Floe 2 can be taken to represent the winter albedo, and an average of all values in Floes 3 and 4 (81%) was used for the summer albedo.

Surface Heat Capacity

The surface heat capacity of sea ice is shown in Eq. 6.1. In this equation, c is the heat capacity in $\frac{J}{kgK}$. To calculate the surface heat capacity, the salinity of the ice (S , ppt), the sea ice temperature (T , °C), the heat capacity of fresh ice (c_0 , $2054 J/kg K^{-1}$), the latent heat of fusion (L_i , $3.340 \times 10^5 J kg^{-1}$), and the ocean

freezing temperature constant (μ , $0.054 \text{ } ^\circ C \text{ ppt}^{-1}$, selected considering salinity) must be specified. The heat capacity of dry snow and ice is approximately equal as the amount of air within the snow changes the heat capacity by a negligible amount.

$$c = c_0 + \frac{L_i \mu S}{T_{ice}^2} \quad (6.1)$$

Ice cores were taken at N-ICE to measure ice temperature and salinity. Mean sea ice surface temperatures for winter and spring were $-22.77 \text{ } ^\circ C$ and $-4.09 \text{ } ^\circ C$, respectively. In the winter, ice surface temperature had a large range and varied as much as $30 \text{ } ^\circ C$ in a month. In the spring, surface temperatures were much more consistent, and showed a slow increase up to freezing.

The salinity varied from 2 g kg^{-1} to 11 g kg^{-1} during both winter and spring, with little difference in the seasonal averages. The mean salinity was 6.08 g kg^{-1} for the entire experiment. Using Eq. 6.1 with these values yields a surface heat capacity of approximately $1.83 \times 10^6 J m^{-3} K^{-1}$. Accounting for the snow density, the surface heat capacity is, on average, approximately 6.4×10^5 . These values are all several orders of magnitude smaller than what is specified in LANDUSE.TBL. The sensible heat flux in the model has been set to an essentially infinite value over water, snow, and ice.

Roughness Length

Roughness length (z_0) is defined in Eq. 6.2 and requires wind speed (w_1 and w_2) at two heights (z_1 and z_2), the von Kármán constant (0.4), and the friction velocity (u^*).

Wind speed was measured at three heights during N-ICE. For this application,

we will be using the 2 m measurement as w_1 and the 10 m measurement has w_2 . Calculations were also done using 2 m and 4 m with similar results, so 10 m was used for z_2 . Friction velocity estimations from EddyPro were used to calculate the mean roughness length for N-ICE.

$$z_0 = \frac{(z_2 - z_1)}{[\exp(\frac{\kappa w_2}{u_*}) - \exp(\frac{\kappa w_1}{u_*})]} \quad (6.2)$$

The mean roughness length for N-ICE is 0.00124 m when calculated using Eq. 6.2. EddyPro defines the roughness length as 0.15 times the canopy height. Since our canopy height has been entered into the program as 0, EddyPro also calculates our roughness length values to be 0.001 m for the entire experiment. The section in Table 6.1 being used already has the lowest friction velocity of all sections, but it is still higher than that calculated from observations taken at N-ICE.

6.2.2 Turbulent Flux Equations

In Chapter 5, two methods were discussed on how to calculate the sensible and latent heat flux over first-year sea ice: the bulk flux algorithm (Foken & Napo, 2008) and the Maximum Entropy Production (MEP) method (Zhang et al., 2021; Wang et al., 2014; Wang & Bras, 2009). Both methods require assumptions and scaling parameters that are generally formulated empirically and that are based on the atmospheric stability near the surface.

In the WRF model, the heat and moisture fluxes are calculated in the surface layer (SL) scheme and land surface model (LSM). These schemes also calculate the upward longwave and shortwave radiation (Dudhia, 2014; Skamarock et al., 2019). The downward components of shortwave and longwave radiation are calculated in the

radiation scheme. In this study, we focus on the components that were formulated in the SL scheme and land surface model.

The Polar WRF sensitivity study described in Chapter 3 used either the Revised MM5 scheme (Paulson, 1970; Dyer & Hicks, 1970; Webb, 1970; Beljaars & Viterbo, 1994) or the ETA Similarity scheme for the SL scheme, depending on the boundary layer (PBL) scheme selection. In fact, the ETA Similarity SL scheme was only used with the Mellor–Yamada–Janji PBL scheme, as this is required by the model. In this chapter, we take a deeper look into the Revised MM5 SL scheme. In general, SL schemes calculate the surface exchange coefficients (Eq. 6.3, using Eq. 6.4 and Eq. 6.5), roughness length, and friction velocity (Dudhia, 2014). Monin-Obukhov similarity theory is used in every SL scheme currently available in the model.

$$\varphi_m = \varphi_h = \begin{cases} 0 & R_b > 0.2 \\ -5\frac{z_1}{L} & 0.2 > R_b > 0 \\ 0 & R_b < 0 \end{cases} \quad (6.3)$$

The scaling parameters defined in 6.3 depend on the near-surface stability. The model uses the bulk Richardson number (R_b , Eq. 6.5) to define three stability regimes for which different relationships apply. These equations use the Richardson number (R_i , Eq. 6.6, Obukhov length (L), vertical wind sheer (S_i), wind speed at 2 m above the ground (V_1), the roughness length (z_0), and potential temperature (θ_s , θ_1 , $\theta_{i+0.5}$ and $\theta_{i-0.5}$) at the ground level, the first level, halfway between the ground and first level, and halfway between the first level and second level (z_s , z_1 , $z_{i+0.5}$ and $z_{i-0.5}$).

$$\frac{z_a}{L} = \begin{cases} 0 & R_b > 0.2 \\ \frac{R_b}{1-5R_b} \ln\left(\frac{z_1}{z_0}\right) & 0.2 > R_b > 0 \\ R_i(z_1) & R_b < 0 \end{cases} \quad (6.4)$$

$$R_b = \frac{gz_1}{\theta_1} \frac{\theta_1 - \theta_s}{(w_1)^2} \quad (6.5)$$

$$R_i = \frac{g}{\theta_a S_i^2} \frac{\theta_{i+.5} - \theta_{i-.5}}{z_{i+.5} - z_{i-.5}} \quad (6.6)$$

The Noah LSM (Chen & Dudhia, 2001) was used in all model runs in Chapter 3 and is the LSM used for this study. Polar WRF modifies the Noah LSM for optimized use over the Arctic, including improvements to the surface energy balance and sea ice (Hines et al., 2015; Bromwich et al., 2009). The LSM uses atmospheric information from the SL scheme and precipitation/radiation from the cloud microphysics (CM) and convective schemes to calculate the vertical transport, turbulent fluxes (sensible and latent heat fluxes shown in Eq. 6.7, 6.11) in the lowest layers of the atmosphere, as well as the friction velocity (Eq. 6.9) and roughness length (Eq. 6.2). The Noah LSM does this using 4 soil temperature and moisture layers (Dudhia, 2014; Skamarock et al., 2019). This particular LSM, with the polar improvements created by The Polar Meteorology Group at the Ohio State University Byrd Polar Research Center implemented, includes fractional snow cover, with snow cover thicknesses allowed to vary throughout the simulation Chen & Dudhia (2001). These Polar improvements also enable the user to specify the sea ice thickness and sea ice albedo (Hines et al., 2015).

$$-H_s = \rho c_p u^* \theta_* = \rho c_p C_{hs} \delta \theta \quad (6.7)$$

$$C_{hs} = \frac{\kappa u^*}{\ln(\frac{z}{z_0}) - \varphi_h} \quad (6.8)$$

$$u_* = \frac{\kappa V_r}{\ln(\frac{z_r}{z_0}) - \varphi_m} \quad (6.9)$$

$$\theta_* = \frac{\kappa \delta \theta}{\ln(\frac{z_r}{z_{0h}}) - \varphi_h} \quad (6.10)$$

$$-H_l = \rho u^* q_* \quad (6.11)$$

$$q_* = \frac{\kappa \delta q}{\ln(\frac{z_r}{z_{0q}}) - \varphi_h} \quad (6.12)$$

To calculate the sensible heat flux, the model must also calculate the surface scaling parameter (φ) and the transfer equation (C_{hs} , Eq. 6.8). Additionally, values must be specified for the air density (ρ), and the heat capacity at constant pressure for dry air (c_p), and the temperature roughness length (z_{0h}). Knowledge of the moisture roughness length (z_{0q}) is required for the latent heat flux and is calculated within the model. Note that the flux equations use r as a subscript indicating the reference height, while the stability equations apply across layers.

6.3 Results

6.3.1 Sensitivity to Surface Properties

The idealized version of WRF was run twice, once with the default LANDUSE.TBL options (Table 6.1, USGS section) and once with values calculated from N-ICE observations. Table 6.3 shows the values calculated above that were used in the modified LANDUSE.TBL. Everything else was held constant and the European Cen-

Table 6.3: Recommended changes to the LANDUSE.TBL file for simulations over first-year sea ice. Original LANDUSE.TBL file settings for snow/ice can be seen in Table 6.1

| Section | Season | Albedo (%) | Roughness Length (m) | Surface Heat Capacity ($J m^{-3} K^{-1}$) |
|---------|--------|------------|----------------------|--|
| NICE | Winter | 70 → 86 | 0.1 → .001 | $9 \times 10^{25} \rightarrow 6 \times 10^5$ |
| NICE | Summer | 55 → 81 | 0.1 → .001 | $9 \times 10^{25} \rightarrow 6 \times 10^5$ |

tre for Medium-Range Weather Forecasting's (ECMWF) Interim Re-Analysis (ERA-Interim) dataset was used as input. The WRF model code is written in FORTRAN and has different files for each scheme. The FORTRAN code for the SL scheme was translated to a Python code, allowing for easy modifications and running of the code.

The first case study period was from 4 February to the end of the day on 6 February. This was during a cloudy period in the winter and has been named the

Table 6.4: Mean model biases (left) and mean flux (right, in parentheses) ($W m^{-2}$) for each idealized case study with both the modified (top of each case) and original (middle of each case) runs. Differences in biases (modified - original) are shown in the last row of each case labeled “Change in Bias.” Positive differences indicate an increase in error and negative indicate a decrease in error when table modifications are implemented.

| | | Latent | Sensible | LW Down | LW Up | SW Down | SW Up |
|---------------|----------------|-------------|-------------|---------------|---------------|---------------|--------------|
| Winter Cloudy | Original | 13.1 (10.3) | 43.5 (50.8) | 2.5 (243.3) | -1.3 (245.0) | | |
| | Modified | 11.7 (8.9) | 35.2 (44.8) | -0.2 (240.6) | 6.5 (252.7) | | |
| | Change in Bias | -1.4 | -8.3 | -2.7 | 7.7 | | |
| Spring Cloudy | Original | -0.2 (-0.5) | -9.8 (-2.3) | 0.3 (240.8) | -19.1 (235.7) | 50.2 (210.7) | 33.2 (168.6) |
| | Modified | 1.6 (1.6) | -4.2 (3.4) | -54.8 (185.6) | -11.7 (243.2) | 111.1 (271.6) | 82.0 (217.3) |
| | Change in Bias | 1.7 | -5.6 | 55.2 | -7.4 | 60.9 | 48.8 |
| Spring Clear | Original | 5.0 (10.3) | 0.5 (15.5) | -8.2 (200.0) | -13.3 (254.5) | 13.4 (339.3) | 15.0 (271.4) |
| | Modified | 4.2 (9.2) | -2.0 (11.0) | -36.2 (172.0) | -5.6 (262.2) | 50.4 (376.3) | 48.4 (304.8) |
| | Change in Bias | -0.8 | 2.4 | 28.0 | -7.7 | 37.0 | 33.4 |

“Winter Cloudy” case. The downward and upward latent heat fluxes can be seen in Figure 6.1 (second and third panels). The modeled values do not capture the timing or sharp decrease in longwave radiation on 5 February. The modifications in the LANDUSE.TBL file do not significantly impact these fluxes, but it can be seen in Table 3.3 that the modifications do reduce the mean bias in the downward longwave radiation but increase the bias in the upward longwave radiation.

The modification in the land use table also improved latent and sensible heat flux biases. Table 3.3 shows the sensible heat flux bias was reduced by almost 10 W m^{-2} in the simulations with the modified values. Latent heat flux was also improved. The modifications to the land use table do reduce the values, but they do not bring them any closer to capturing any observed patterns in the fluxes during this case.

The second case study period was a cloudy period in the spring. The “Summer” section of the table applies from 14 April to 15 October. Both spring case studies use the “Summer” section of the land use table. Radiative fluxes for this period can be seen in Figure 6.2 (second and third panel). At this time, the sun was rising over the N-ICE ship, so there is a shortwave component to the flux. The modified values did not do well for this case and changing the LANDUSE.TBL values removed many of the clouds during this period. While the cloud mask is not shown here, this is clear in both the longwave and shortwave radiation. The shortwave radiation (bottom panels, Figure 6.2) shows less radiation in the unmodified modeled results than in the modified. In fact, the unmodified results match the measurements fairly well in the shortwave. The lack of clouds in the modified simulation can also be seen in the longwave downward flux (Figure 6.2, fourth and fifth panels). These fluxes for the modified simulation are consistently much lower than those from the original runs

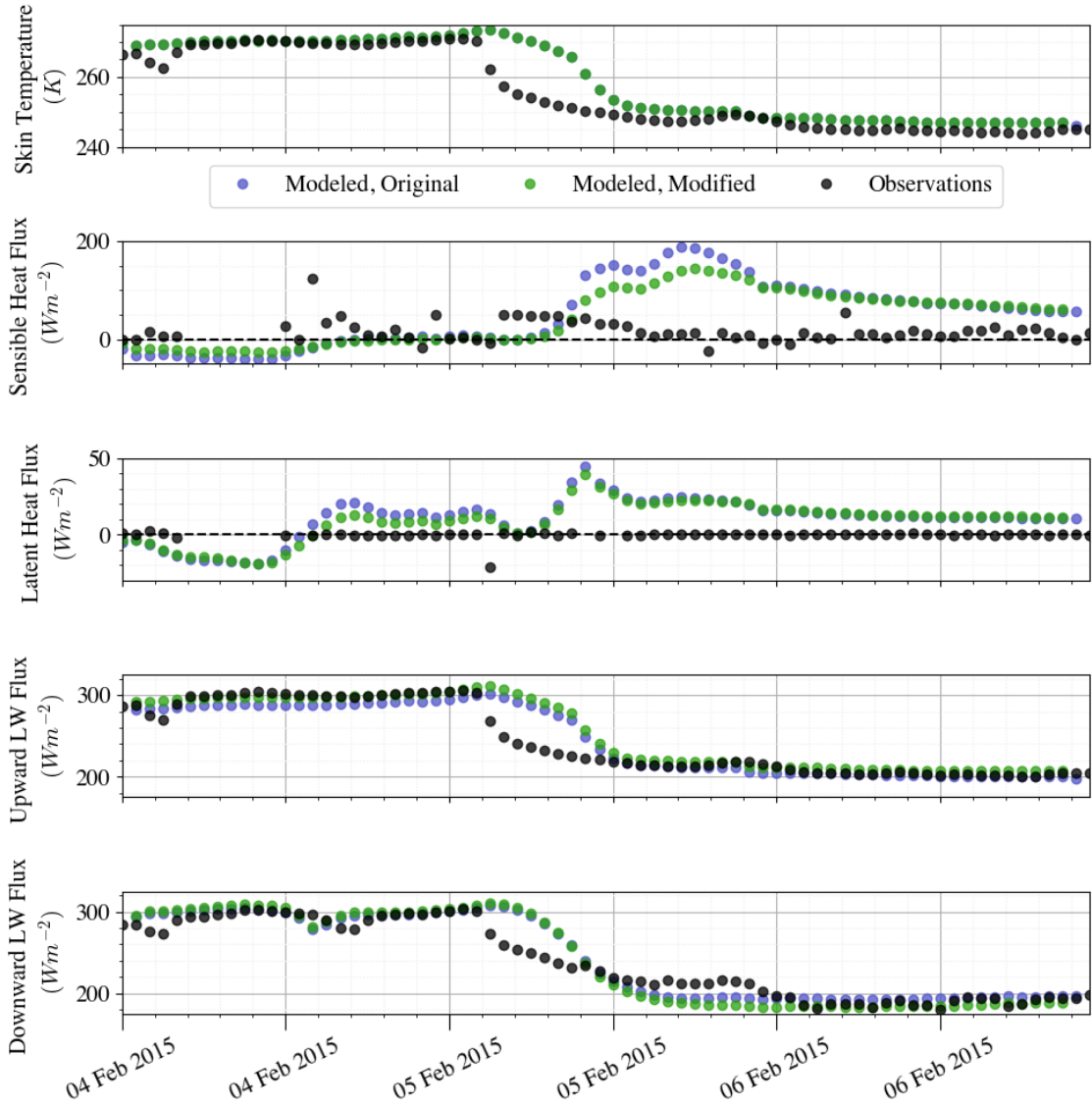


Figure 6.1: Temperature (top), sensible and latent heat flux (second and third from top), and upward and downward components of longwave radiation (fourth and fifth) for the model with original LANDUSE.TBL values (blue), the model with modified LANDUSE.TBL values (green), and the observations (black) from 4 February to 6 February.

and have little variation until the last day when the model finally begins to produce cloud cover.

The modified LANDUSE.TBL produced higher sensible and latent heat flux values near the end of the study period (Figure 6.2, second and third panels). Some increased sensible heat flux values are observed near the end of this case, and at this point, the modified model is producing clouds and warming the air above the surface, making this the only variable and time period during this case that the modified simulation outperformed the original. Overall, mean biases (Table 3.3) were higher for the model runs using the modified values than those using the original table values.

The last case study period is from 22 May to 24 May, when the N-ICE field site experienced 24 hours of cloudless skies. This 24-hour period was captured well by both the modified and unmodified simulations in the shortwave (Figure 6.3, bottom panels) but the day prior had some disagreement. Again, the modified simulation produced fewer clouds than those produced by the original simulations. This time, however, it matches the observations better, as the original simulation did not produce clear-sky conditions early enough in the case. The same issues can be seen with longwave radiation. Upward longwave radiation (Figure 6.3, fourth and fifth panels) is overestimated by the original simulation for the first 24 hours of the case as the model produces clouds for too long into the evening on 22 May. The unmodified, however, does not produce enough downward longwave radiation, as this simulation did not produce enough clouds early enough. The original simulations produced lower biases for both components of shortwave radiation and the downward component of longwave radiation. Upward longwave radiation, however, had a lower bias in the modified simulation results, as the surface warmed.

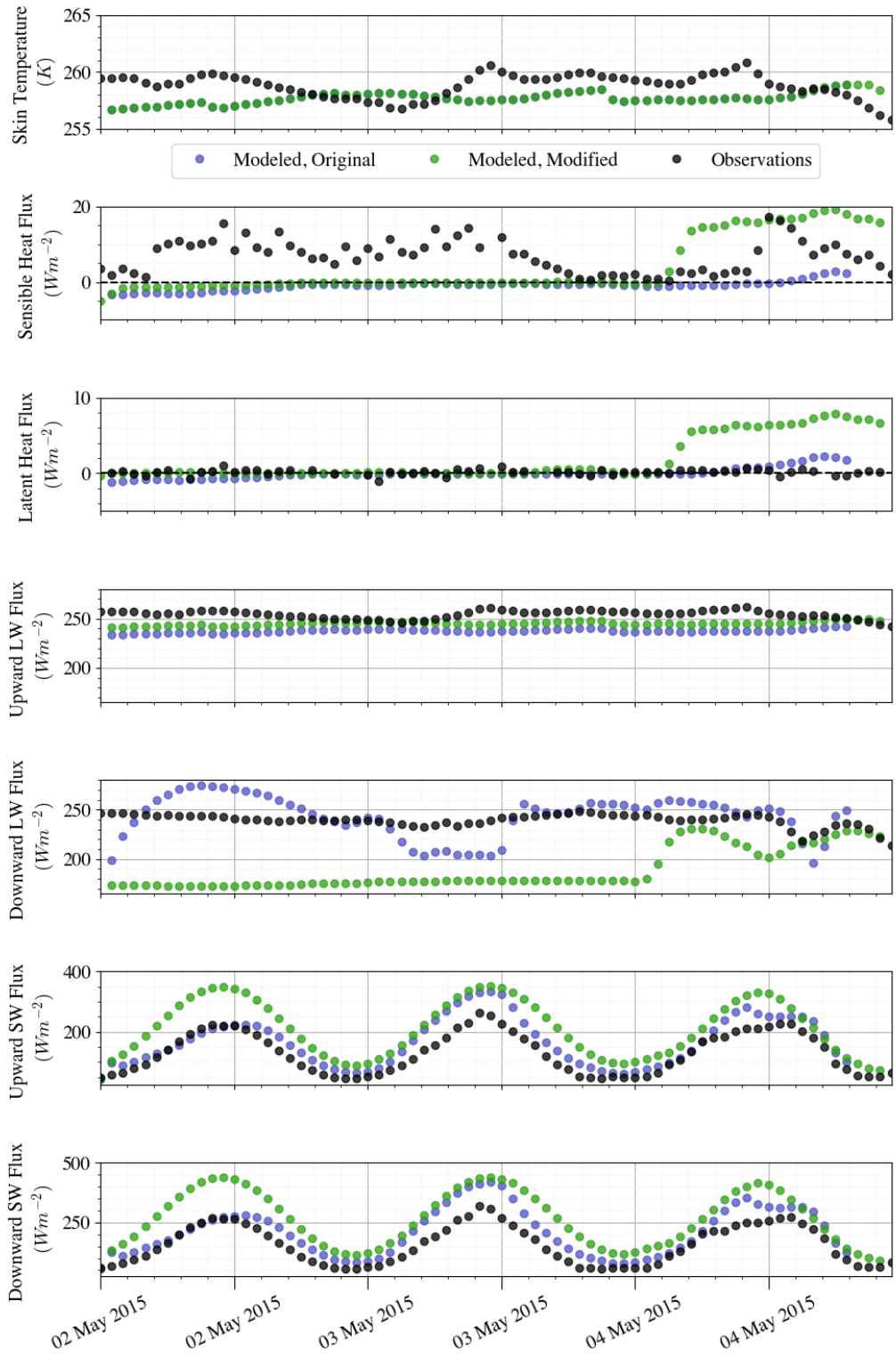


Figure 6.2: Temperature (top), sensible and latent heat flux (second and third from top), upward and downward components of longwave radiation (fourth and fifth), and upward and downward components of shortwave radiation (sixth and seventh) for the model with original LANDUSE.TBL values (blue), the model with modified LANDUSE.TBL values (green), and the observations (black) from 2 May to 4 May.

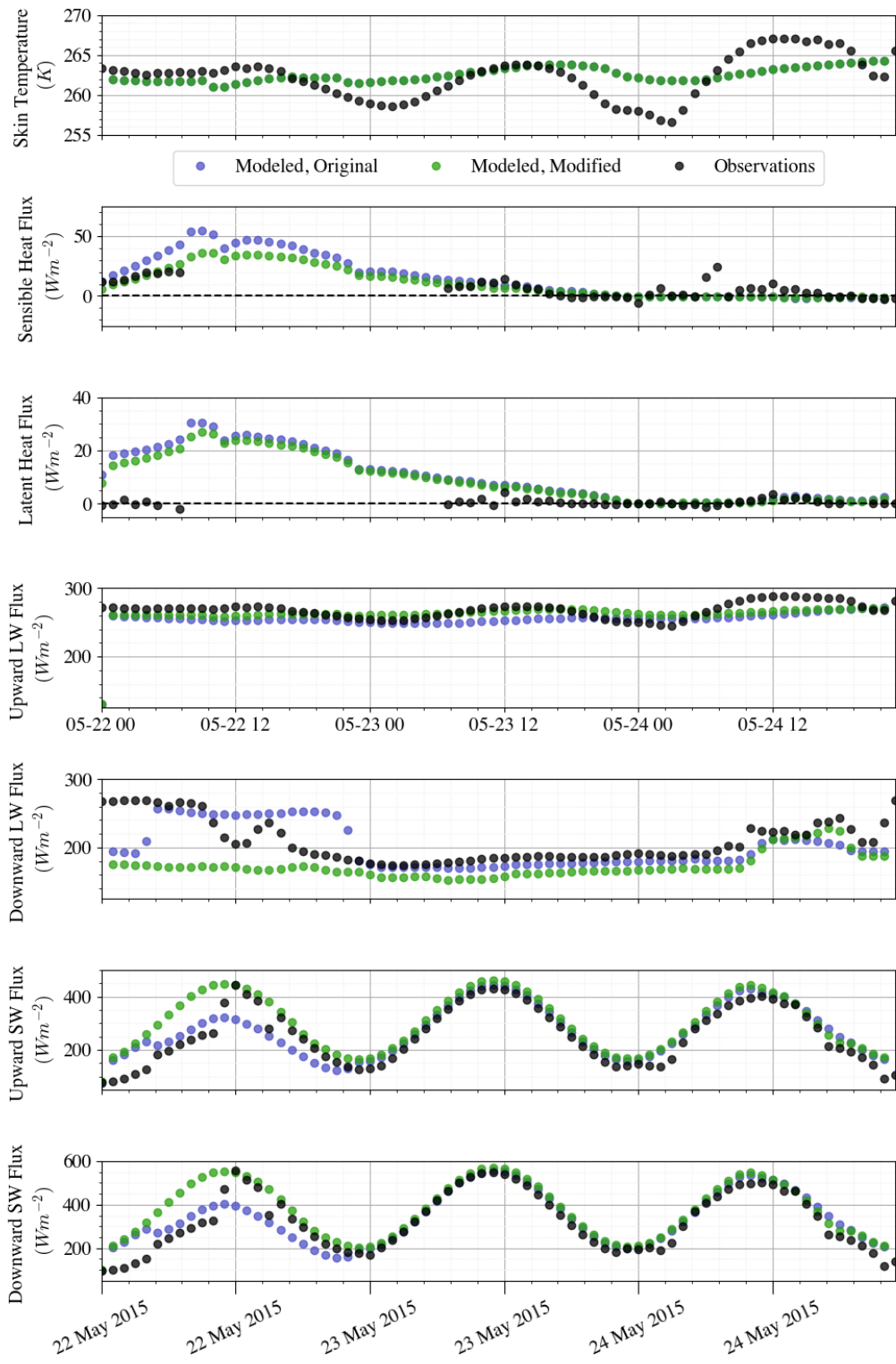


Figure 6.3: Temperature (top), sensible and latent heat flux (second and third from top), upward and downward components of longwave radiation (fourth and fifth), and upward and downward components of shortwave radiation (sixth and seventh) for the model with original LANDUSE.TBL values (blue), the model with modified LANDUSE.TBL values (green), and the observations (black) from 22 May to 24 May.

Latent and sensible heat flux values (Figure 6.3, second and third panel) were similar between the two model runs past the first 24 hours. They did differ during the first day when the models had disagreements about the cloud cover. The model originally overestimated these fluxes during this time period, so even a small decrease in these values could be an improvement. Table 3.3 shows that the latent heat flux bias decreased by almost 1 Wm^{-2} with the modifications, but the sensible heat flux bias increased.

6.3.2 Turbulent Flux Equations

Throughout the entire field expedition, the WRF offline calculation did a surprisingly good job of replicating the sensible heat flux observations. Figure 6.4 shows the observations in black and the WRF offline calculation in magenta. It is often hard to see the modeled values in the time series because they are so close to the observations that many of the points overlap each other, and they create a well-defined 1:1 line on the scatter plot. This indicates that errors in estimating the sensible heat flux are likely due to the errors in values being calculated schemes outside of the SL scheme and LSM.

The WRF equation depends heavily on the friction velocity value, which is shown in Figure 6.5. The observed friction velocity has been calculated by the EddyPro software, and the WRF was calculated using the Polar WRF offline code using equations 6.9. While WRF produces slightly smaller values of friction velocity, it is still fairly accurate throughout the entire observation period.

The results of the latent heat flux calculations (Figure 6.6) do not match the observations anywhere near as well as the sensible heat flux calculations. The latent heat flux values at N-ICE were very small, and because of this, the y-axis on the

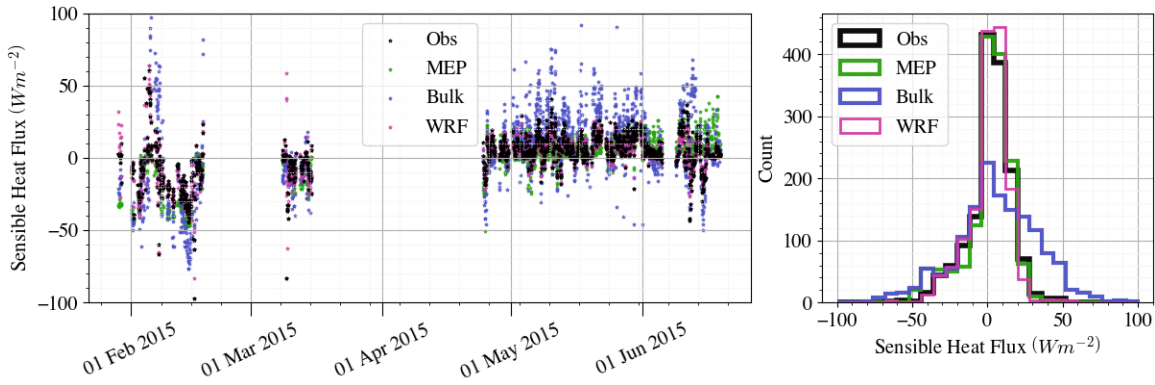


Figure 6.4: Sensible heat flux observed at N-ICE (black) and calculated from Polar WRF offline translated code (magenta), with the MEP equation (green) and with the bulk equation (blue).

scatter plot in Figure 6.6 has been reduced to -5 to 5 W m^{-2} . All ways of calculating latent heat flux result in large errors, and none are able to accurately replicate the small values observed. Particularly in the summer, all equations gave largely negative latent heat flux values, but observations remained small.

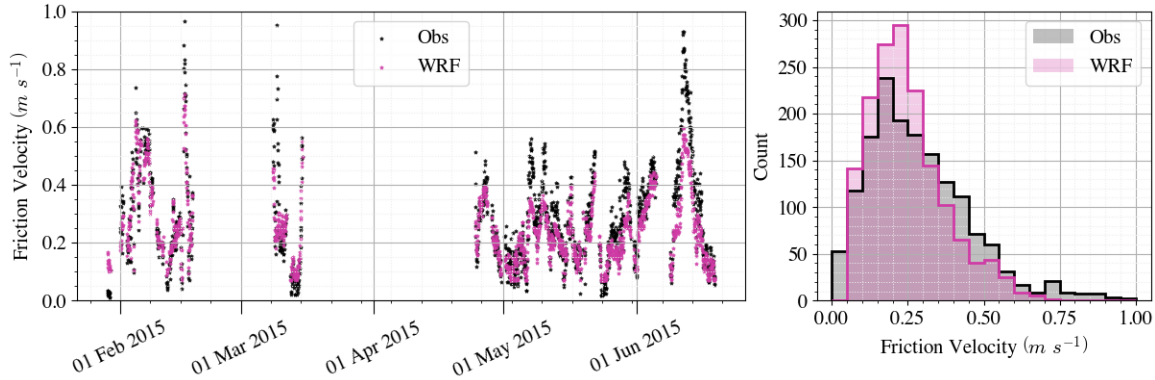


Figure 6.5: Friction velocity observed at N-ICE (black) and calculated from Polar WRF offline translated code (magenta).

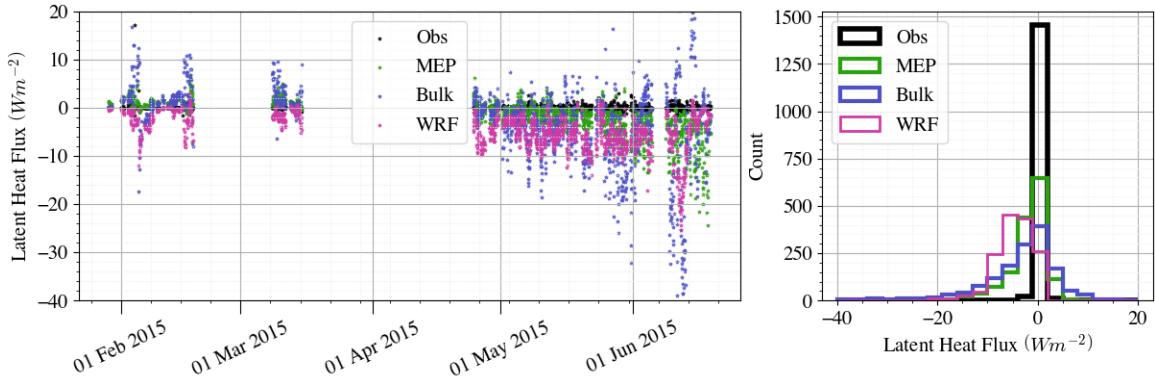


Figure 6.6: Latent heat flux observed at N-ICE (black) and calculated from Polar WRF offline translated code (magenta), with the MEP equation (green) and with the bulk equation (blue).

6.4 Conclusions

Slight improvements to the WRF model performance can be made by using the appropriate surface properties for thin, first-year sea ice. However, these modifications provide slight increases in model performance but are not the solution to the large discrepancies (compared to N-ICE observations) in the turbulent heat fluxes seen in Chapter 3. Surface albedo, emissivity, and surface roughness can be adjusted to reduce the differences between the model and N-ICE observations. When turbulent flux equations were coded separately (and run “offline”) from the model using the measured radiative fluxes, they produced results very close to observations. While further improvements are likely possible, the sensitivity studies performed here show that most of the error within Polar WRF (shown in Chapter 3) can be attributed to the inaccurate cloud microphysics (CM) schemes described in Chapter 4.

CHAPTER SEVEN

CONCLUSIONS, RECOMMENDATIONS, AND FUTURE WORK

The polar regions, notably the Arctic and maritime Antarctic, are experiencing impacts from climate change at magnitudes and rates that are among the highest in the world, and will become profoundly different in the near-term future (by 2050) under all warming scenarios (high confidence).

- IPCC Sixth Assessment Report, August 2021

7.1 Conclusions

This chapter provides conclusions of this study and makes recommendations for improving Polar WRF over thin, first-year sea ice. In addition, future work is outlined for improving the Polar WRF.

The results from the Polar Weather Research and Forecasting model (Polar WRF) in Chapter 3 showed that, regardless of cloud microphysics (CM) or planetary boundary layer (PBL) scheme, the model had some large biases. In the winter, every model simulation had a negative sensible heat bias, and all but one (the P3-YSU simulation) had a positive bias in longwave radiation. In the spring, all model simulations underestimated the net longwave radiation and overestimated the net shortwave. Latent heat flux biases were larger in the spring than in winter. The 2-MYNN run had the lowest overall biases in the winter and the G-YSU had the lowest biases in the spring and summer. Cloud radiative forcing (CRF) for these two schemes was calculated in Chapter 4 and showed that clouds in the 2-MYNN scheme had the correct CRF, but in the spring, the modeled CRF was quite low compared to the observations,

due to the fact that the cloud fraction was greatly underestimated by Polar WRF. Heterogeneities in the sea ice surface are likely missed in these simulations due to the 3 km by 3 km grid size used and the course resolution ice datasets used.

Eddy covariance measurements from N-ICE were processed through the LI-COR's EddyPro 7 software to estimate surface heat fluxes over the first-year ice using the eddy covariance method. The Noah Land Surface Model (LSM) used to calculate surface fluxes in Polar WRF currently uses the bulk approach over sea ice, which requires estimations of the Monin-Obukhov scaling and stability parameters. These parameters are dependent on wind, potential temperature gradients, and surface stability. The cold surface often results in a strongly stable surface layer, a characteristic typical in the polar regions, presenting potential errors in the stability regimes used to estimate these parameters. In Chapter 4, latent and sensible heat flux values were calculated for N-ICE using the bulk flux algorithm and the Maximum Entropy Production (MEP) method. Chapter 5 showed that both techniques of calculating the turbulent fluxes did an acceptable job of estimating the sensible heat flux, but both have larger ranges of values for the latent heat flux, indicating these equations were producing too much phase change. Chapter 6 compares these equations to the equations used by Polar WRF. The equations within WRF do very well at estimating the turbulent fluxes when the correct radiative fluxes are specified, indicating that most of the error within Polar WRF are due to inaccurate simulations of cloud properties. Observed latent heat flux values were quite low and could not be accurately replicated with the model or using any of the equations presented here. This could be a result of measurement error, but more work must be done to examine the latent heat flux measurements.

Chapter 6 presents the model sensitivity to changing land use parameters and to different turbulent flux equations. These results suggest that the model performance can be improved over first-year sea ice by modifying key parameters provided by the lookup tables within the model.

7.2 Recommendations

This section suggests recommendations for improving the Polar WRF model, based on the sensitivity studies performed in Chapter 6 that were motivated by Chapters 3 and 4.

7.2.1 Setting Surface Parameters

More testing needs to be done to determine if these values are best under specific conditions, but using the results described above, the following modifications are recommended for the LANDUSE.TBL file when working over first-year sea ice. However, it should be stressed for the user to be mindful that cloudiness is extremely important to the surface energy budget, and to be aware that these values may produce less cloud cover than using the original USGS values found in the LANDUSE.TBL. Therefore, additional modifications will likely be necessary to the CM schemes.

1. Increase albedo in both the winter and summer (column 3, Table 6.3)
2. Decrease surface roughness from 0.1 to 0.001 m (column 5, Table 6.3)
3. Decreased surface heat capacity and use a different value for winter and summer (column 6, Table 6.3)

Flores et al. (2021) measured surface roughness lengths over all land surfaces using several different remote-sensing techniques. All of their roughness length values for

surfaces similar to that seen at N-ICE were between 0.005 m and 0.001 m , further proving that the roughness length over the snow surface is less than the 0.1 m specified by the model.

7.2.2 Turbulent Flux Equations

Latent and sensible heat flux values in WRF are calculated within the surface modules using meteorology from the BL scheme and radiation from the radiation scheme. In this study, all physics schemes except for the surface layer (SL) scheme were removed and were run "offline", using the idealized version of WRF at a single location to calculate sensible and latent heat fluxes. When observed radiation, wind, temperature, and moisture values were used as input to the offline model, the calculated sensible heat flux values were quite accurate compared to the N-ICE measurements. The latent heat fluxes, however, were not and often had significantly larger negative values than what was observed. The latent heat flux at N-ICE could not be accurately replicated by the offline WRF calculation or any of the external ways of calculating it. Chapter 3 shows that all WRF simulations struggled to replicate the latent heat flux. Chapter 5 describes several methods for calculating the latent heat flux, but none accurately represented the latent heat flux seen at N-ICE.

Chapter 3 showed that the Polar WRF model, when run as a complete model, does not accurately represent the surface conditions seen at N-ICE. The sensible heat flux had a mean bias over all model simulations of -20 Wm^{-2} in the winter and 4.9 Wm^{-2} in the spring. Latent heat flux had a mean bias of -0.6 Wm^{-2} in the winter and 3.3 Wm^{-2} in the spring. However, the offline calculations accurately simulated the sensible heat flux, indicating that some input parameters used in the SL scheme and LSM are the primary source of this error. Radiation is input to the surface from

the radiation scheme in WRF but came directly from the N-ICE observations in the offline calculation. The offline calculation allows us to isolate the surface schemes and ensure any cloud-related errors are not impacting errors in the surface fluxes. The radiation is almost certainly incorrect as a result of incorrect cloud properties in the model. As described in Chapter 4, the clouds observed at N-ICE were primarily mixed phase (mixture of water and ice) and, as shown in Chapter 3, they were not accurately captured in any of the WRF simulations.

7.3 Future Work

7.3.1 Flux Equations

Two ways of estimating the latent and sensible heat flux were presented in Chapter 5 and were compared to equations used within WRF in Chapter 6. This research could be expanded to other ways of calculating the latent and sensible heat flux, such as the Priestly-Taylor method or the Bowen Ratio method. The two methods selected here were chosen due to their use in models (the bulk algorithm method) and recent development for use in the polar regions (Maximum Entropy Production method). However, there is the potential for other methods of estimating surface fluxes to perform well over first-year sea ice.

7.3.2 Clouds Microphysics Schemes

An early goal of this research was to look further into the cloud microphysics (MP) schemes used in WRF to improve polar clouds, particularly mixed-phase or those with small ice particles. However, upon further investigation of the model, there were very large biases in the latent and sensible heat flux calculations. While a portion of this is attributed to the incorrect portrayal of clouds, the amount cannot

be determined without first finding the errors in the flux equations themselves. While the recommendations made here may improve the atmospheric structure and moisture exchange within the model, they do not fix issues with the CM schemes.

All WRF microphysics (MP) schemes with the exception of the Predicted Particle Phase (P3) scheme use “binning” to identify particle characteristics. This means that cloud particle properties are simplified and assigned to a range of particle sizes. This might be an issue when mixed-phase particles are present. The P3 scheme removes this simplification by evolving the assigned cloud particle properties with the evolution of the particle itself, but has a size cutoff and, therefore, has the potential to exclude smaller ice particles that are often observed in the polar regions. Chapter 3 showed that the P3 scheme did not simulate the atmosphere at N-ICE well, and this could be due to an inappropriate size cutoff for cloud particles in the polar regions. Reducing this size limit could improve cloud properties from runs using the P3 scheme.

Polar WRF has been found to simulate clouds and cloud radiative forcing poorly over multi-year sea ice and Arctic land (Hines et al., 2011). These issues arise more notably with high, thin clouds, and are likely due to synoptic-scale influences. It would be informative to correlate the cloud radiative forcing biases with pressure changes and/or the proximity of nearby pressure systems to determine if this issue is also being observed at N-ICE. While Hines et al. (2011); Hines & Bromwich (2008) found that the vertical moisture profiles were accurately simulated over Arctic land, they state that it is possible that the moisture profiles and vertical mixing could be a source of error in low-level clouds over sea ice. This has not yet been studied over first-year sea ice and would be a beneficial next step to understanding why the low clouds simulated here are not accurate.

7.3.3 Ice Surface Heterogenities

The smallest grid cell size used in the studies presented here is 3 km by 3 km . This grid cell size is not small enough to resolve some of the finer-scale surface heterogeneities found with first-year sea ice. The sea ice datasets used here had approximately 12 by 12 km grid cells, resulting in some oversimplification of the ice surface being provided to the model.

While this problem is not due to any shortcoming of the model, the following modifications to the studies presented here could be done to examine this issue:

1. Make the entire parent domain smaller to reduce computational expenses.
2. Obtain a high-resolution gridded sea ice dataset with 1 km or smaller grid spacing.
3. Create another smaller nested domain with grid cells of 1 by 1 km .
4. If the sea ice dataset has $< 1\text{ km}$ grid size, another, smaller nested domain can be created with 0.3 by 0.3 km grid cells.

With these modifications to both the domain and grid cell size, it may be necessary to use a point-following domain setup in the case of N-ICE, as the ship is moving and may quickly move out of a 0.3 km square area.

BIBLIOGRAPHY

- Andreas, E. L., Fairall, C. W., Grachev, A. A., Guest, P. S., Horst, T. W., Jordan, R. E., & Persson, P. O. G. (2003). 3.11 turbulent transfer coefficients and roughness lengths over sea ice: The sheba results. (p. 10).
- Andreas, E. L., Horst, T. W., Grachev, A. A., Persson, P. O. G., Fairall, C. W., Guest, P. S., & Jordan, R. E. (2010). Parametrizing turbulent exchange over summer sea ice and the marginal ice zone. *Quarterly Journal of the Royal Meteorological Society*, 136(649), 927–943.
- Andreas, E. L., Persson, P. O. G., Grachev, A. A., Jordan, R. E., Guest, P. S., Fairall, C. W., & Horst, T. W. (2009). Announcing the sheba bulk turbulent flux algorithm. (p. 12).
- Arias, P., Bellouin, N., Coppola, E., Jones, R., Krinner, G., Marotzke, J., Naik, V., Palmer, M., Plattner, G.-K., Rogelj, J., Rojas, M., Sillmann, J., Storelvmo, T., Thorne, P., Trewin, B., Achuta Rao, K., Adhikary, B., Allan, R., Armour, K., Bala, G., Barimalala, R., Berger, S., Canadell, J., Cassou, C., Cherchi, A., Collins, W., Collins, W., Connors, S., Corti, S., Cruz, F., Dentener, F., Dereczynski, C., Di Luca, A., Diongue Niang, A., Doblas-Reyes, F., Dosio, A., Douville, H., Engelbrecht, F., Eyring, V., Fischer, E., Forster, P., Fox-Kemper, B., Fuglestvedt, J., Fyfe, J., Gillett, N., Goldfarb, L., Gorodetskaya, I., Gutierrez, J., Hamdi, R., Hawkins, E., Hewitt, H., Hope, P., Islam, A., Jones, C., Kaufman, D., Kopp, R., Kosaka, Y., Kossin, J., Krakovska, S., Lee, J.-Y., Li, J., Mauritzen, T., Maycock, T., Meinshausen, M., Min, S.-K., Monteiro, P., Ngo-Duc, T., Otto, F., Pinto, I., Pirani, A., Raghavan, K., Ranasinghe, R., Ruane, A., Ruiz, L., Sallée, J.-B., Samset, B., Sathyendranath, S., Seneviratne, S., Sörensson, A., Szopa, S., Takayabu, I., Tréguier, A.-M., van den Hurk, B., Vautard, R., von Schuckmann, K., Zaehle, S., Zhang, X., & Zickfeld, K. (2021). *Technical Summary*, (p. 33144). Cambridge, United Kingdom and New York, NY, USA: Cambridge University Press.
- Beesley, J. A. (2007). Estimating the effect of clouds on the arctic surface energy budget. (pp. 1–15).
- Beljaars, A. C., & Viterbo, P. (1994). The sensitivity of winter evaporation to the formulation of aerodynamic resistance in the ecmwf model. *Boundary-Layer Meteorology*, 71(1-2), 135–149.
- Beljaars, A. C. M., & Holtslag, A. A. M. (1991). Flux parameterization over land surfaces for atmospheric models. *Journal of Applied Meteorology*, 30(3), 327–341.

- Bohren, C. F., & Clothiaux, E. E. (2006). *Fundamentals of atmospheric radiation: an introduction with 400 problems*. John Wiley & Sons.
- Bohren, C. F., & Huffman, D. R. (2008). *Absorption and scattering of light by small particles*. John Wiley & Sons.
- Bromwich, D. H., Hines, K. M., & Bai, L. S. (2009). Development and testing of polar weather research and forecasting model: 2. arctic ocean. *Journal of Geophysical Research*, 114(D8), 2113–22.
- Businger, J. A., Wyngaard, J. C., Izumi, Y., & Bradley, E. F. (1971). Flux-profile relationships in the atmospheric surface layer. *Journal of the Atmospheric Sciences*, 28(2), 181–189.
- Campbell, J. R., Hlavka, D. L., Welton, E. J., Flynn, C. J., Turner, D. D., Spinhirne, J. D., Scott, V. S., & Hwang, I. H. (2002). Full-time, eye-safe cloud and aerosol lidar observation at atmospheric radiation measurement program sites: Instruments and dataprocessing. *Journal of Atmospheric and Oceanic Technology*, 19(4), 431–442.
- Chen, F., & Dudhia, J. (2001). Coupling an advanced land surface–hydrology model with the penn state–ncar mm5 modeling system. part i: Model implementation and sensitivity. *Monthly weather review*, 129(4), 569–585.
- Cogley, J. G., & Henderson-Sellers, A. (1984). Effects of cloudiness on the high-latitude surface radiation budget. *Monthly Weather Review*, 112(5), 1017–1032.
- Cohen, A. E., Cavallo, S. M., Coniglio, M. C., & Brooks, H. E. (2015). A review of planetary boundary layer parameterization schemes and their sensitivity in simulating southeastern u.s. cold season severe weather environments. *Weather and Forecasting*, 30(3), 591–612.
- Cohen, L., Hudson, S. R., Walden, V. P., Graham, R. M., & Granskog, M. A. (2017). Meteorological conditions in a thinner arctic sea ice regime from winter to summer during the norwegian young sea ice expedition (n-ice2015). *Journal of Geophysical Research: Atmospheres*, 122(14), 7235–7259.
- Cohen, L. D. (2006). *Boundary layer characteristics and ozone fluxes at Summit, Greenland*. Ph.D. thesis, University of Colorado at Boulder.
- Computational, & Laboratory, I. S. (2019). Cheyenne: Hpe/sgi ice xa system (university community computing).

- Core Writing Team, R. P., & (eds.), L. M. (2014). Arctic climate impact assessment. Tech. rep. 151 pp.
- Curry, J. A., & Ebert, E. E. (1992). Annual cycle of radiation fluxes over the arctic ocean: Sensitivity to cloud optical properties. *Journal of Climate*, 5, 1267–1280.
- Curry, J. A., Schramm, J. L., Rossow, W. B., & Randall, D. (1996). Overview of arctic cloud and radiation characteristics. *Journal of Climate*, 9(8), 1731–1764.
- Dee, D. P., Uppala, S. M., Simmons, A. J., Berrisford, P., Poli, P., Kobayashi, S., Andrae, U., Balmaseda, M., Balsamo, G., Bauer, d. P., et al. (2011). The era-interim reanalysis: Configuration and performance of the data assimilation system. *Quarterly Journal of the royal meteorological society*, 137(656), 553–597.
- DiGirolamo, C. L. P. D. J. C. P. G., N., & Zwally., H. J. (2022). Sea ice concentrations from nimbus-7 smmr and dmsp ssm/i-ssmis passive microwave data, version 2.
- Dudhia, J. (2014). Overview of wrf physics. *University Corporation for Atmospheric Research, Boulder, CO*.
- Dyer, A., & Bradley, E. F. (1982). An alternative analysis of flux-gradient relationships at the 1976 itce. *Boundary-Layer Meteorology*, 22(1), 3–19.
- Dyer, A., & Hicks, B. (1970). Flux-gradient relationships in the constant flux layer. *Quarterly Journal of the Royal Meteorological Society*, 96(410), 715–721.
- Dyer, A. J. (1974). A review of flux-profile relationships. *Boundary-Layer Meteorology*, 7(3), 363–372.
- Falge, E., Baldocchi, D., Olson, R., Anthoni, P., Aubinet, M., Bernhofer, C., Burba, G., Ceulemans, R., Clement, R., Dolman, H., et al. (2001). Gap filling strategies for defensible annual sums of net ecosystem exchange. *Agricultural and forest meteorology*, 107(1), 43–69.
- Floors, R., Badger, M., Troen, I., Grogan, K., & Permien, F.-H. (2021). Satellite-based estimation of roughness lengths and displacement heights for wind resource modelling. *Wind Energy Science*, 6(6), 1379–1400.
- Flynna, C. J., Mendozaa, A., Zhengb, Y., & Mathurb, S. (2007). Novel polarization-sensitive micropulse lidar measurement technique. *Opt. Express*, 15(6), 2785–2790.
- Foken, T., & Kretschmer, D. (1990). Stability dependence of the temperature structure parameter. *Boundary-layer meteorology*, 53(1), 185–189.

- Foken, T., & Napo, C. J. (2008). *Micrometeorology*, vol. 2. Springer.
- Francis, J. A., Chan, W., Leathers, D. J., Miller, J. R., & Veron, D. E. (2009). Winter northern hemisphere weather patterns remember summer arctic sea-ice extent. *Geophysical Research Letters*, 36(7).
- Gallet, J.-C., Merkouriadi, I., Liston, G. E., Polashenski, C., Hudson, S., Rösel, A., & Gerland, S. (2017). Spring snow conditions on arctic sea ice north of svalbard, during the norwegian young sea ice (n-ice2015) expedition. *Journal of Geophysical Research: Atmospheres*, 122(20), 10,820–10,836.
- Gavrilov, A., & Petrov, Y. (1981). Accuracy of the estimates for turbulent fluxes measured over the sea by standard hydrometeorological instruments. *Meteor i Gidrol*, 4, 52–59.
- Grachev, A. A., Andreas, E. L., Fairall, C. W., Guest, P. S., & Persson, P. O. G. (2007). Sheba flux-profile relationships in the stable atmospheric boundary layer. *Boundary-Layer Meteorology*, 124(3), 315–333.
- Graham, R. M., Cohen, L., Petty, A. A., Boisvert, L. N., Rinke, A., Hudson, S. R., Nicolaus, M., & Granskog, M. A. (2017a). Increasing frequency and duration of arctic winter warming events. *Geophysical Research Letters*, 44(13), 6974–6983.
- Graham, R. M., Cohen, L., Ritzhaupt, N., Segger, B., Graversen, R. G., Rinke, A., Walden, V. P., Granskog, M. A., & Hudson, S. R. (2019). Evaluation of six atmospheric reanalyses over arctic sea ice from winter to early summer. *Journal of Climate*, 32(14), 4121–4143.
- Graham, R. M., Rinke, A., Cohen, L., Hudson, S. R., Walden, V. P., Granskog, M. A., Dorn, W., Kayser, M., & Maturilli, M. (2017b). A comparison of the two arctic atmospheric winter states observed during n-ice2015 and sheba. *Journal of Geophysical Research: Atmospheres*, 122(11), 5716–5737.
- Granskog, M., Assmy, P., Gerland, S., Spreen, G., Steen, H., & Smedsrød, L. (2016). Arctic research on thin ice: Consequences of arctic sea ice loss. *Eos*, 97, 1–6.
- Granskog, M. A., Fer, I., Rinke, A., & Steen, H. (2018). Atmosphere-ice-ocean-ecosystem processes in a thinner arctic sea ice regime: The norwegian young sea ice (n-ice2015) expedition. *Journal of Geophysical Research: Oceans*, 123(3), 1586–1594.
- Granskog, M. A., Pavlov, A. K., Sagan, S., Kowalcuk, P., Raczkowska, A., & Stedmon, C. A. (2015). Effect of sea-ice melt on inherent optical properties and

- vertical distribution of solar radiant heating in arctic surface waters. *Journal of Geophysical Research: Oceans*, 120(10), 7028–7039.
- Grenfell, T. C., & Warren, S. G. (1999). Representation of a nonspherical ice particle by a collection of independent spheres for scattering and absorption of radiation. *Journal of Geophysical Research: Atmospheres*, 104(D24), 31697–31709.
- Guide, W. U. (2019). User's guide for the advanced research wrf (arw) modeling system version 3.6.
- Handorf, D., Foken, T., & Kottmeier, C. (1999). The stable atmospheric boundary layer over an antarctic ice sheet. *Boundary-Layer Meteorology*, 91(2), 165–189.
- Hines, K. M., & Bromwich, D. H. (2008). Development and testing of polar weather research and forecasting (wrf) model. part i: Greenland ice sheet meteorology. *Monthly Weather Review*, 136(6), 1971–1989.
- Hines, K. M., & Bromwich, D. H. (2017). Simulation of late summer arctic clouds during ascos with polar wrf. *Monthly Weather Review*, 145(2), 521–541.
- Hines, K. M., Bromwich, D. H., Bai, L., Bitz, C. M., Powers, J. G., & Manning, K. W. (2015). Sea ice enhancements to polar wrf. *Monthly Weather Review*, 143(6), 2363–2385.
- Hines, K. M., Bromwich, D. H., Bai, L.-S., Barlage, M., & Slater, A. G. (2011). Development and testing of polar wrf. part iii: Arctic land. *Journal of Climate*, 24(1), 26–48.
- Hines, K. M., Bromwich, D. H., Wang, S.-H., Silber, I., Verlinde, J., & Lubin, D. (2019). Microphysics of summer clouds in central west antarctica simulated by the polar weather research and forecasting model (wrf) and the antarctic mesoscale prediction system (amps). *Atmospheric Chemistry and Physics*, 19(19), 12431–12454.
- Holland, M. M., & Bitz, C. M. (2003). Polar amplification of climate change in coupled models. *Climate Dynamics*, 21(3-4), 221–232.
- Hong, S.-Y., Dudhia, J., & Chen, S.-H. (2004). A revised approach to ice microphysical processes for the bulk parameterization of clouds and precipitation. *Monthly Weather Review*, 132, 103–120.
- Hoyer, S., & Hamman, J. (2017). xarray: N-D labeled arrays and datasets in Python. *Journal of Open Research Software*, 5(1).

- Hunter, J. D. (2007). Matplotlib: A 2d graphics environment. *Computing in Science & Engineering*, 9(3), 90–95.
- Inc, L.-C. (2021). *EddyPro version 7.0 Help and User's Guide*. LI-COR, Inc. Lincoln, NE.
- Inoue, J., Curry, J. A., & Maslanik, J. A. (2008). Application of aerosondes to melt-pond observations over arctic sea ice. *Journal of Atmospheric and Oceanic Technology*, 25(2), 327–334.
- Intrieri, J. M., Fairall, C. W., Shupe, M. D., Persson, P. O. G., Andreas, E. L., Guest, P. S., & Moritz, R. E. (2002). An annual cycle of arctic surface cloud forcing at sheba. *Journal of Geophysical Research*, 107(C10), 8039.
- Iribarne, J. V., & Godson, W. L. (1981). *Atmospheric Thermodynamics*.
- Itkin, P., Spreen, G., Cheng, B., Doble, M., Girard-Ardhuin, F., Haapala, J., Hughes, N., Kaleschke, L., Nicolaus, M., & Wilkinson, J. (2017). Thin ice and storms: Sea ice deformation from buoy arrays deployed during N-ICE2015: THIN ICE AND STORMS. *Journal of Geophysical Research: Oceans*, 122(6), 4661–4674.
- Janić, Z. I. (2001). Nonsingular implementation of the mellor-yamada level 2.5 scheme in the ncep meso model.
- Janjic, Z. I. (1994). The step-mountaing eta coordinate model: Further developments of the convection, viscous sublayer, and turbulence closure schemes. *Monthly Weather Review*, 122, 927–945.
- Jiménez, P. A., Dudhia, J., González-Rouco, J. F., Navarro, J., Montávez, J. P., & García-Bustamante, E. (2012). A revised scheme for the wrf surface layer formulation. *Monthly weather review*, 140(3), 898–918.
- Kahl, J. D. W., Galbraith, J. A., & Martinez, D. A. (1999). Decadal-scale variability in long-range atmospheric transport to the summit of the greenland ice sheet. *Geophysical Research Letters*, 26(4), 481–484.
- Kayser, M., Maturilli, M., Graham, R. M., Hudson, S. R., Rinke, A., Cohen, L., Kim, J.-H., Park, S.-J., Moon, W., & Granskog, M. A. (2017). Vertical thermodynamic structure of the troposphere during the norwegian young sea ice expedition (n-ice2015). *Journal of Geophysical Research: Atmospheres*, 122(20), 10,855–10,872.
- Klett, J. D. (1981). Stable analytical inversion solution for processing lidar returns. *Applied Optics*, 20(2), 211.

- Ladwig, W. (2017). wrf-python.
- Lente, G., & Ősz, K. (2020). Barometric formulas: various derivations and comparisons to environmentally relevant observations. *ChemTexts*, 6(2), 13.
- LI-COR, I. (2021). Eddypro software.
- Listowski, C., & Lachlan-Cope, T. (2017). The microphysics of clouds over the antarctic peninsula – part 2: modelling aspects within polar wrf. *Atmospheric Chemistry and Physics*, 17(17), 10195–10221.
- McBean, G., Alekseev, G., Chen, D., Førland, E., Fyfe, J., Groisman, P., King, R., Melling, H., & Vose, R. (2005). Arctic: Arctic climate impact assessment. Tech. rep.
- McClatchey, R. (1972). *Optical properties of the atmosphere*. 411. Air Force Cambridge Research Laboratories, Office of Aerospace Research.
- Meier, W. N., Hovelsrud, G. K., van Oort, B. E., Key, J. R., Kovacs, K. M., Michel, C., Haas, C., Granskog, M. A., Gerland, S., Perovich, D. K., Makshtas, A., & Reist, J. D. (2014). Arctic sea ice in transformation: A review of recent observed changes and impacts on biology and human activity. *Reviews of Geophysics*, 52(3), 185–217.
- Mellor, G. L., & Yamada, T. (1982). Development of a turbulence closure model for geophysical fluid problems. *Reviews of Geophysics and Space Physics*, 20(4), 851–875.
- Mendoza, A., & Flynn, C. (2006). Micropulse lidar (mpl) handbook. *The US Department of Energy*.
- Merkouriadi, I., Gallet, J.-C., Graham, R. M., Liston, G. E., Polashenski, C., Rösel, A., & Gerland, S. (2017). Winter snow conditions on arctic sea ice north of svalbard during the norwegian young sea ice (n-ice2015) expedition. *Journal of Geophysical Research: Atmospheres*, 122(20), 10,837–10,854.
- Mesinger, F. (1993). Forecasting upper tropospheric turbulence within the framework of the mellor-yamada 2.5 closure. *Res. Activ. Atmos. Oceanic Mod.*.
- Milbrandt, J. A., & Morrison, H. (2016). Parameterization of cloud microphysics based on the prediction of bulk ice particle properties. part iii: Introduction of multiple free categories. *Journal of the Atmospheric Sciences*, 73(3), 975–995.

- Miller, G. H., Landvik, J. Y., Lehman, S. J., & Southon, J. R. (2017). Episodic neoglacial snowline descent and glacier expansion on svalbard reconstructed from the 14c ages of ice-entombed plants. *Quaternary Science Reviews*, 155, 67–78.
- Miller, N. B., Shupe, M. D., Cox, C. J., Walden, V. P., Turner, D. D., & Steffen, K. (2015). Cloud radiative forcing at summit, greenland. *Journal of Climate*, 28(15), 6267–6280.
- Mlawer, E. J., Taubman, S. J., Brown, P. D., Iacono, M. J., & Clough, S. A. (1997). Radiative transfer for inhomogeneous atmospheres: Rrtm, a validated correlated-k model for the longwave. *Journal of Geophysical Research: Atmospheres*, 102(D14), 16663–16682.
- Morrison, H., Curry, J. A., & Khvorostyanov, V. I. (2005). A new double-moment microphysics parameterization for application in cloud and climate models. part i: Description. *Journal of the Atmospheric Sciences*, 62(6), 1665–1677.
- Morrison, H., & Milbrandt, J. A. (2015). Parameterization of cloud microphysics based on the prediction of bulk ice particle properties. part i: Scheme description and idealized tests. *Journal of the Atmospheric Sciences*, 72(1), 287–311.
- Mukul Tewari, N., Tewari, M., Chen, F., Wang, W., Dudhia, J., LeMone, M., Mitchell, K., Ek, M., Gayno, G., Wegiel, J., et al. (2004). Implementation and verification of the unified noah land surface model in the wrf model (formerly paper number 17.5). In *Proceedings of the 20th conference on weather analysis and forecasting/16th conference on numerical weather prediction, Seattle, WA, USA*, vol. 14.
- Munoz-Martin, J. F., Perez, A., Camps, A., Ribó, S., Cardellach, E., Stroeve, J., Nandan, V., Itkin, P., Tonboe, R., Hendricks, S., Huntemann, M., Spreen, G., & Pastena, M. (2020). Snow and ice thickness retrievals using gnss-r: Preliminary results of the mosaic experiment. *Remote Sensing*, 12(24).
- Oikkonen, A. (2017). *Evolution of sea ice cover: Result of interplay between dynamics and thermodynamics*. Finnish Meteorological Institute.
- Olson, J. B., Kenyon, J. S., Angevine, W., Brown, J. M., Pagowski, M., Sušelj, K., et al. (2019). A description of the mynn-edmf scheme and the coupling to other components in wrf–arw.
- Overland, J. (2011). Potential arctic change through climate amplification processes. *Oceanography*, 24(3), 176–185.

- Paulson, C. A. (1970). The mathematical representation of wind speed and temperature profiles in the unstable atmospheric surface layer. *Journal of Applied Meteorology*, 9(6), 857–861.
- Persson, P. O. G. (2002). Measurements near the atmospheric surface flux group tower at sheba: Near-surface conditions and surface energy budget. *Journal of Geophysical Research*, 107(C10), 8045.
- Pilgj, N., Czernecki, B., Krayza, M., Migala, K., & Kolendowicz, L. (2018). Application of the polar wrf model for svalbard - sensitivity to planetary boundary layer, radiation and microphysics schemes. *Polish Polar Research*, 39(3), 349–370.
- Placzek, G. (1934). *Rayleigh-streuung und Raman-effekt*, vol. 2. Akademische Verlagsgesellschaft.
- Powers, J. G., Manning, K. W., Bromwich, D. H., Cassano, J. J., & Cayette, A. M. (2012). A decade of antarctic science support through amps. *Bulletin of the American Meteorological Society*, 93(11), 1699–1712.
- Ramanathan, P. (1989). *Synchronization and distributed agreement in real-time systems*. University of Michigan.
- Randall, D., Curry, J. A., Battisti, D., Flato, G., Grumbine, R., Hakkinen, S., Martinson, D., Walsh, J., Weatherly, J., & Preller, R. (1998). Status of and outlook for large- scale modeling of atmosphere-ice- ocean interactions in the arctic. *Bulletin of the American Meteorological Society*, 79(2), 197–219.
- Reeves Eyre, J. E. J., Zeng, X., & Zhang, K. (2021). Ocean surface flux algorithm effects on earth system model energy and watercycles. *Frontiers in Marine Science*, 8, 642804.
- Royer, J., Planton, S., & Déqué, M. (1990). A sensitivity experiment for the removal of arctic sea ice with the french spectral general circulation model. *Climate Dynamics*, 5, 1–17.
- Schweiger, A. J. (2004). Changes in seasonal cloud cover over the arctic seas from satellite and surface observations. *Geophysical Research Letters*, 31(12).
- Schweiger, A. J., Lindsay, R. W., Key, J. R., & Francis, J. A. (1999). Arctic clouds in multiyear satellite data sets. *Geophysical Research Letters*, 26(13), 1845–1848.
- Schweiger, R. L. J. Z. M. S. H. S., A. (2011). Uncertainty in modeled arctic sea ice volume. *Journal of Geophysical Research: Atmospheres*.

- Serreze, M. C., Kahl, J. D., & Schell, R. C. (1992). Low-level temperature inversions of the eurasian arctic and comparisons with soviet drifting station data. *Journal of Climate*, (5), 165–629.
- Shupe, M. D., & Intrieri, J. M. (2003). Cloud radiative forcing of the arctic surface: The influence of cloud properties, surface albedo, and solar zenith angle. *Journal of Climate*, 17, 616–628.
- Shupe, M. D., & Intrieri, J. M. (2004). Cloud radiative forcing of the arctic surface: The influence of cloud properties, surface albedo, and solar zenith angle. *Journal of Climate*, 17(3), 616–628.
- Shupe, M. D., Rex, M., Dethloff, K., Damm, E., Fong, A., Gradinger, R., Heuzé, C., Loose, B., Makarov, A., Maslowski, W., et al. (2020). Arctic report card 2020: The mosaic expedition: A year drifting with the arctic sea ice.
- Skamarock, W. C., Klemp, J. B., Dudhia, J., Gill, D. O., Liu, Z., Berner, J., Wang, W., Powers, J. G., Duda, M. G., Barker, D. M., et al. (2019). A description of the advanced research wrf model version 4. *National Center for Atmospheric Research: Boulder, CO, USA*, 145(145), 550.
- Sledd, A., & L'Ecuyer, T. (2019). How much do clouds mask the impacts of arctic sea ice and snow cover variations? different perspectives from observations and reanalyses. *Atmosphere*, 10(1), 12–26.
- Sotiropoulou, G., Tjernström, M., Sedlar, J., Achtert, P., Brooks, B. J., Brooks, I. M., Persson, P. O. G., Prytherch, J., Salisbury, D. J., Shupe, M. D., Johnston, P. E., & Wolfe, D. (2016). Atmospheric conditions during the arctic clouds in summer experiment (acse): Contrasting open water and sea ice surfaces during melt and freeze-up seasons. *Journal of Climate*, 29(24), 8721–8744.
- Spinhirne, J., Hlavka, D., Scott, V., Galbraith, A., & Reagan, J. (2007). Cloud and aerosol height distribution retrieval and analysis employing continuous operation lidar data.
- Stillwell, R. A., Neely III, R. R., Thayer, J. P., Shupe, M. D., & Turner, D. D. (2018). Improved cloud-phase determination of low-level liquid and mixed-phase clouds by enhanced polarimetric lidar. *Atmospheric Measurement Techniques*, 11(2), 835–859.
- Stramler, K., Del Genio, A. D., & Rossow, W. B. (2011). Synoptically driven arctic winter states. *Journal of Climate*, 24(6), 1747–1762.

- Stroeve, J., Holland, M. M., Meier, W., Scambos, T., & Serreze, M. (2007). Arctic sea ice decline: Faster than forecast. *Geophysical Research Letters*, 34(9).
- Stroeve, J., & Notz, D. (2018). Changing state of arctic sea ice across all seasons. *Environmental Research Letters*, 13(10), 103001.
- Stull, R. B. (1988). *An Introduction to Boundary Layer Meteorology*. Kluwer Academic Publishers, Dordrecht, Boston and London.
- Tao, W.-K., Simpson, J., & McCumber, M. (1989). An ice-water saturation adjustment. *Monthly Weather Review*, 117, 231–235.
- Tastula, E.-M., Vihma, T., & Andreas, E. L. (2012). Evaluation of polar wrf from modeling the atmospheric boundary layer over antarctic sea ice in autumn and winter. *Monthly Weather Review*, 140(12), 3919–3935.
- Tewari, M., Chen, F., Wang, W., Dudhia, J., LeMone, M., Mitchell, K., Ek, M., Gayno, G., Wegiel, J., Cuenca, R., et al. (2004). Implementation and verification of the unified noah land surface model in the wrf model. In *20th conference on weather analysis and forecasting/16th conference on numerical weather prediction*, vol. 1115, (pp. 2165–2170).
- Tjernström, M., Leck, C., Persson, P. O. G., Jensen, M. L., Oncley, S. P., & Targino, A. (2004). Experimental equipment: A supplement to the summertime arctic atmosphere: Meteorological measurement during the arctic ocean experiment 2001. *Bulletin of the American Meteorological Society*, 85(9), Es14–es18.
- Tjernström, M., Žagar, M., Svensson, G., Cassano, J. J., Pfeifer, S., Rinke, A., Wyser, K., Dethloff, K., Jones, C., Semmler, T., & Shaw, M. (2005). Modelling the arctic boundary layer: An evaluation of six arcmip regional-scale models using data from the sheba project. *Boundary-Layer Meteorology*, 117(2), 337–381.
- Turner, D. D. (2005). Arctic mixed-phase cloud properties from aerol lidar observations: Algorithm and results from sheba. *Journal of Applied Meteorology*, 44(4), 427–444.
- Turner, J., Harangozo, S. A., Marshall, G. J., King, J. C., & Colwell, S. R. (2002). Anomalous atmospheric circulation over the weddell sea, antarctica during the austral summer of 2001/02 resulting in extreme sea ice conditions. *Geophysical Research Letters*, 29(24).
- Untersteiner, N. (1980). Aijdex review. *Sea Ice Processes and Models*, edited by: Pritchard, RS, University of Washington, Seattle, (pp. 3–11).

- Uttal, T., Curry, J. A., McPhee, M. G., Perovich, D. K., Moritz, R. E., Maslanik, J. A., Guest, P. S., Stern, H. L., Moore, J. A., Turenne, R., Heiberg, A., Serreze, M. C., Wyllie, D. P., Persson, O. G., Paulson, C. A., Halle, C., Morison, J. H., Wheeler, P. A., Makshtas, A., Welch, H., Shupe, M. D., Intrieri, J. M., Stamnes, K., Lindsey, R. W., Pinkel, R., Pegau, W. S., Stanton, T. P., & Grenfeld, T. C. (2002). Surface heat budget of the arctic ocean. *Bulletin of the American Meteorological Society*, 83(2), 255–275.
- Verlinde, J., Harrington, J. Y., McFarquhar, G. M., Yannuzzi, V. T., Avramov, A., Greenberg, S., Johnson, N., Zhang, G., Poellot, M. R., Mather, J. H., Turner, D. D., Eloranta, E. W., Zak, B. D., Prenni, A. J., Daniel, J. S., Kok, G. L., Tobin, D. C., Holz, R., Sassen, K., Spangenberg, D., Minnis, P., Tooman, T. P., Ivey, M. D., Richardson, S. J., Bahrman, C. P., Shupe, M., DeMott, P. J., Heymsfield, A. J., & Schofield, R. (2007). The mixed-phase arctic cloud experiment. *Bulletin of the American Meteorological Society*, 88(2), 205–222.
- Vihma, T., & Pirazzini, R. (2005). On the factors controlling the snow surface and 2-m air temperatures over the arctic sea ice in winter. *Boundary-Layer Meteorology*, 117(1), 73–90.
- Walden, V. P., Hudson, S. R., Cohen, L., Murphy, S. Y., & Granskog, M. A. (2017a). Atmospheric components of the surface energy budget over young sea ice: Results from the n-ice2015 campaign. *Journal of Geophysical Research: Atmospheres*, 122(16), 8427–8446.
- Walden, V. P., Murphy, S., Hudson, S. R., & Cohen, L. (2017b). N-ice2015 atmospheric turbulent fluxes.
- Walsh, J. E., & Chapman, W. L. (1998). Arctic cloud–radiation–temperature associations in observational data and atmospheric reanalyses. *Journal of Climate*, 11(11), 3030–3045.
- Wang, J., & Bras, R. (2011). A model of evapotranspiration based on the theory of maximum entropy production. *Water Resources Research*, 47(3).
- Wang, J., & Bras, R. L. (2009). A model of surface heat fluxes based on the theory of maximum entropy production. *Water Resources Research*, 45(11).
- Wang, J., Bras, R. L., Nieves, V., & Deng, Y. (2014). A model of energy budgets over water, snow, and ice surfaces. *Journal of Geophysical Research: Atmospheres*, 119(10), 6034–6051.

- Wang, X., & Key, J. R. (2005). Arctic surface, cloud, and radiation properties based on the avhrr polar pathfinder dataset. part i: Spatial and temporal characteristics. *Journal of Climate*, 18, 2558–2574.
- Webb, E. K. (1970). Profile relationships: The log-linear range, and extension to strong stability. *Quarterly Journal of the Royal Meteorological Society*, 96(407), 67–90.
- Wiscombe, W. J., & Warren, S. G. (1980). A model for the spectral albedo of snow. i: Pure snow. *Journal of the Atmospheric Sciences*, 37(12), 2712–2733.
- Wunderling, N., Willeit, M., Donges, J. F., & Winkelmann, R. (2020). Global warming due to loss of large ice masses and arctic summer sea ice. *Nature Communications*, 11(1), 5177.
- Zhang, J., Lindsay, R., Steele, M., & Schweiger, A. (2008). What drove the dramatic retreat of arctic sea ice during summer 2007? *Geophysical Research Letters*, 35(11), L11505.
- Zhang, J., & Rothrock, D. (2003). Modeling global sea ice with a thickness and enthalpy distribution model in generalized curvilinear coordinates. *Monthly Weather Review*, (pp. 845–861).
- Zhang, Y.-M., Song, M.-R., Dong, C.-M., & Liu, J.-P. (2021). Modeling turbulent heat fluxes over arctic sea ice using a maximum-entropy-production approach. *Advances in Climate Change Research*, 12(4), 517–526.
- Zilitinkevitsch, S., & Tschalikov, D. (1968). The vertical structure of the planetary boundary layer at unstable stratification. *Meteorologie und Hydrologie*, 6, 41–49.

APPENDIX A

GLOSSARY

A.1 Acronyms

2-MYJ Model runs using: Morrison Bulk Two-Moment (CM) and
Mellor–Yamada–Janjic (PBL)

2-MYNN Model runs using: Morrison Bulk Two-Moment (CM) and
Mellor–Yamada Nakanishi Niino (PBL)

5-MYJ Model runs using: WRF Single-Moment 5-Class (CM) and
Mellor–Yamada–Janjic (PBL)

5-MYNN Model runs using: WRF Single-Moment 5-Class (CM) and
Mellor–Yamada Nakanishi Niino (PBL)

AGU American Geophysical Union

AIDJEX Arctic Ice Dynamics Joint Experiment

AOE International Arctic Ocean Experiment

ARM Atmospheric Radiation Measurements program

AVHRR Advanced Very High Resolution Radiometer

BDP Businger-Dyer-Pandolfo relationship

CM Cloud microphysics

CMIP5 Coupled Model Intercomparison Project Phase 5

CRF Cloud radiative forcing

DOE Department of Energy

DOE SCGSR The Department of Energy's Office of Science Graduate Student Research Program

EC Eddy covariance

ERA Interim European Centre for Medium-Range Weather Forecasting's Interim Re-Analysis

G-MYJ Model runs using: Goddard (CM) and
Mellor-Yamada-Janjic (PBL)

G-MYNN Model runs using: Goddard (CM) and
Mellor-Yamada Nakanishi Niino (PBL)

G-YSU Model runs using: Goddard (CM) and
Yonsei University (PBL)

GMD Global Monitoring Division

IPCC Intergovernmental Panel on Climate Change

LSM Land Surface Model

LW Longwave

MEP Maximum Entropy Production method

MM5 Fifth-Generation mesoscale model

MPL Micropulse Lidar

MYJ Mellor–Yamada–Janjic (PBL scheme)

MYNN Mellor–Yamada Nakanishi Niino (PBL scheme)

N-ICE The Norwegian Young Sea Ice field Campaign

N-ICE2015 The Norwegian Young Sea Ice field Campaign

NOAA National Oceanic and Atmospheric Administration

Noah LSM Unified Noah Land Surface Model

P3 Predicted Particle Properties (CM scheme)

P3-MYJ Model runs using: Predicted Particle Properties (CM) and

Mellor–Yamada–Janjic (PBL)

P3-YSU Model runs using: Predicted Particle Properties (CM) and

Yonsei University (PBL)

PBL Planetary boundary layer

PIOMAS Pan-Arctic Ice Ocean Modeling and Assimilation System

Polar WRF Polar Weather Research and Forecasting model

RRTM Rapid Radiative Transfer Model

RRTMG Rapid Radiative Transfer Model GCM (RRTM with increased model efficiency)

SHEBA The Surface Heat Budget of the Arctic Ocean Experiment

SNR Signal-to-Noise ratio

SSMI Special Sensor Microwave/Imager

SW Shortwave

WRF Weather Research and Forecasting Model

YSU Yonsei University (PBL scheme)

A.2 Constants and Variables

A.2.1 Alphabetical

$B(\theta_{pc})$ a scaling function of phase change parameter

C ocean heat flux

c heat capacity

c_0 surface heat capacity of fresh ice

C_D drag coefficient

C_{Ez} moisture exchange bulk transfer coefficient

C_{Hz} heat exchange bulk transfer coefficient

c_p specific heat

c_p specific heat of air

CRF cloud radiative forcing

D_q surface layer friction velocity constant

F_s energy storage

g asymmetry factor or gravity

H_l latent heat flux

H_s sensible heat flux

I_0 apparent thermal inertia of air

I_{wsi} thermal inertia parameter

L Obukhov length

L_i latent heat of fusion

L_v latent heat of vaporization

M_{avail} moisture availability

Q_{all} all-sky radiation

Q_{clear} clear-sky radiation

$Q_{lw\downarrow}$ longwave downward flux

$Q_{lw\uparrow}$ longwave upward flux

Q_{net} net radiation

q_s specific humidity at the surface

$Q_{sw\downarrow}$ shortwave downward flux

$Q_{sw\uparrow}$ shortwave upward flux

q_z specific humidity at measurement height

R residual flux

R_b bulk Richardson number

R_i Richardson number

s surface

S salinity of ice

S_i vertical wind sheer

SN_{COVR} snow cover fraction

SN_H snow height

T_{ice} sea ice temperature

T_r reference temperature (300K)

T_s temperature at the surface

T_z temperature at measurement height

w wind speed

w_1 wind speed at the first layer

y_{mod} modeled value

y_{obs} observed value

z measurement height

z_0 roughness length

z_{0brd} background roughness length

z_{0eff} effective roughness length

z_{0h} temperature roughness length

z_{0q} moisture roughness length

z_1 first layer height

z_2 second layer height

z_r reference height

A.2.2 Greek Letters

κ Kármán constant

λ thermal conductivity

μ ocean freezing constant

ω single scattering albedo

$w'\theta'_v$ covariance of wind speed and virtual potential temperature

ρ air density

θ solar zenith angle

θ_{pc} phase change parameter

θ_s potential temperature at the surface

θ_v virtual potential temperature

θ_z potential temperature at measurement height

φ_h scaling parameter for heat

φ_m scaling parameter for moisture

ζ surface-layer stability parameter

APPENDIX B

THE EFFECT OF DATA GAP FILLING ON SENSIBLE HEAT FLUX CALCULATIONS

This chapter was written as a final project for CE 506: Theory and Measurement of Turbulent Fluxes, April 28th, 2016. Report and figures are in their original format.

Abstract

The flux dataset collected during the Norwegian Young Sea Ice Cruise (N-ICE) project had a number of problems. The most restricting problem is the number of data gaps throughout the 30-minute pre-processed data files. In some cases, the amount of missing data made the file unable to be processed. In order to fix this, the data was filled by taking the section of data before it (or after, in the case that the missing data was too close to the start of the dataset) and replicating it for the time period with no recorded data. To ensure that this method of data filling was acceptable, data from Barrow, Alaska was used to compare the post-processed data of a complete dataset with the post-processed results from the same dataset after (artificially added) gaps had been filled. Analysis of both the difference in sensible heat fluxes and the turbulent spectra from before and after the data filling were examined and determined the filling method appropriate for the type of gaps in the N-ICE data.

B.1 Introduction

The Norwegian Young Sea Ice Cruise (N-ICE) project occurred from February 2015 to June 2015 (5 months). The primary objective of the project was to understand the ice dynamics and energy flux in the Arctic associated with young sea ice. Measurements were taken above newly formed sea ice while the R/V Lance research ship, used as a base for the researchers and a powerhouse for the equipment, flowed with the ice (Granskog et al., 2016). The eddy flux data collected during N-ICE is currently still in the processing phase. Any sections of missing data must first be repaired to ensure the complete dataset can be processed without the removal of any

files. The main goal of this paper is to determine if the filling method used was an appropriate method by examining if it disturbed patterns or drastically changed heat flux values.

A large number of gaps exist in the N-ICE atmospheric turbulence data. These gaps could occur for a number of reasons, including rime ice accumulation on instruments, extreme cold temperatures (Cohen, 2006), issues with the power supply to the instruments, computer, or datalogger, and the packing up and moving of the instruments. The flux datasets from this experiment are in 30-minute files, often with small gaps of missing data within the file time period. It is important to patch these small data gaps, as too many can reduce the number of files that can be processed through the Licor processing software EddyPro (LI-COR, 2021; Inc, 2021)

Some data-filling methods include using the mean diurnal variation or using look-up tables. The mean diurnal variation method takes the mean of the half-hour before the gap in missing data and fills the gap with that mean. In the look-up table method, meteorological variations and other forcings can be taken into consideration (Falge et al., 2001) For this dataset, however, a different approach was used. It did not seem appropriate to fill this minute with the mean of the previous half-hour because the gaps in data being filled were approximately around one minute in length. In addition, the half-hour before these gaps likely had a number of data gaps, too. The approach to gap-filling described in this paper is based on taking the values immediately before (or after) the data gap, and replacing the missing data values with them, essentially duplicating the previous minute.

This paper begins with a more detailed description of all data used. This is followed by an examination of the data-filling method used, including both a time-

series analysis and a look at the spectra of the fluctuations. This paper will conclude with a description of future work to be done and a summary of the results presented here.

B.2 Methods

The primary objective of this project is to determine a method to fill the dataset from N-ICE. From January 2015 to June 2015, a ship was frozen into newly forming sea ice in the Arctic ocean (Granskog et al., 2016). An array of instruments was installed onboard the ship, making measurements of temperature, wind speed, wind direction, fluctuations in water vapor, and carbon dioxide, which can be used to calculate heat fluxes. The dataset collected by these instruments is the focus of this project, with the goal of conducting the most accurate possible sensible and latent heat flux calculations using EddyPro.

A major problem with the dataset was the existence of semi-regular data gaps throughout the collection period. These chunks of missing data appeared approximately every 5 minutes and lasted for about a minute. While these gaps were not present in every file, they could be found throughout the majority of the collection period. In addition to these semi-regular data gaps, irregular data gaps of varying duration also existed but occurred at a much lower rate. For the majority of the dataset, the spacing and duration of gaps were consistent.

There were much larger gaps in the data, too, where the instrument was likely taken down for the ship to be moved. Gaps lasting more than a 30-minute data file were regarded as breaks in data collection (instead of missing data) and no data filling was attempted for these time periods. The three largest data breaks were used to separate the data into three separate time periods, primarily for plotting purposes.

These periods are 14 February 2015 through 18 February 2015, 9 March 2015 through 18 March 2015, and 24 April 2015 through 6 June 2015.

As EddyPro reads the files and begins to process them, it checks for missing data. The threshold of missing data that is allowed can be changed, and for this project, the missing data allowance was set to 33% missing data. This missing data allowance means that 30-minute input files that had less than 66% data collection during that time period would not be used in the calculation of the fluxes. If a file was missing more than 33% of the data due to missing gaps, the file was removed from processing. To ensure all collected data is used, every file must be made to contain less than 33% data.

To create a complete dataset, these semi-regular and irregular (shorter than 30-minute) gaps had to be filled. The filling method selected for this project took the time period before the gap and inserted it into the time period of the gap for every measured variable. In other words, in each gap, the minute before the gap was repeated. If there was not enough data before the gap to use in the filling, the data from after the gap was used (as each 30-minute file was filled separately from one another, previous files were not used). It is important to note that the same time period was selected for each variable for each gap to fill the gap, conserving any correlations between fluxes in different variables that may exist.

To ensure that this data-filling technique was accurately portraying the fluxes that might have been occurring, another dataset was used for comparison. Three sets of files collected in Barrow, Alaska from 2012 were used. While Barrow does not have the exact same conditions as the N-ICE project, it is in a similar climate and is a relatively close representation of the N-ICE conditions. The time periods of Barrow

data were 2 April 2012 at 01:30 to 04:30, 24 May 2012 at 16:30 to 25 May 2012 at 14:30, and 9 June 2012 at 14:30 to 20:30. These files were of the same format as the N-ICE data, but contained no gaps. The correct fluxes of this dataset could be calculated because of the completeness of the files. Regular gaps throughout the entire dataset are likely the worst-case scenario, as one-minute gaps every 5 minutes would not only remove small eddies occurring on less than a minute time scales could be removing patterns or eddies occurring on a 5-minute time scale. In addition, adding in the section of data before the gap could produce an artificial correlation, showing eddies occurring that did not actually exist. Because of this it was decided that regular gaps would be removed from the Barrow dataset for quality checking.

B.3 Results and Discussion

B.3.1 Barrow, Alaska – Quality Checking of Filling Algorithm

Mean Departures from Original Sensible Heat Flux

For the April section of Barrow data, both the filled data and the data with gaps matched the original data very closely when sensible heat flux was calculated. This is displayed in Figure B.1 A. Figure B.1 B shows the percent differences in the data with gaps and the filled data from the original data. This was done by using Eq. B.1 and B.2, respectively. All percent differences are less than 1, indicating that the calculated sensible heat flux for both the data with the gaps in it and the data that has been filled is close to the sensible heat fluxes calculated by the complete dataset.

$$\frac{Data_{withgaps} - Data_{original}}{Data_{original}} \times 100 \quad (B.1)$$

$$\frac{Data_{gapfilled} - Data_{original}}{Data_{original}} \times 100 \quad (B.2)$$

The magnitude of the mean difference is 0.0316 W m^{-2} between the original data and the data with the gaps inserted into it. The mean difference between the original and the filled data is 0.0698 W m^{-2} . The sensible heat flux calculated using the data with gaps in it was closer to the original sensible heat fluxes than that calculated with the filled data. However, both are small differences, so for the April case, the filling algorithm can be said to have done well. The percent differences further attest to both cases fitting the original dataset well, as the larger percent difference from the original is less than 40%. With sensible heat values as small as they are in this section, it seems reasonable.

In the May case, the three data runs also closely followed the same sensible heat flux pattern. This is shown in Figure B.1 C, and the differences in EddyPro calculated sensible heat flux for this month are shown in Figure B.1 D. During this month, the mean differences between the filled data and the data with artificial gaps versus the original dataset calculations were very similar. The data with gaps had a mean difference from the original data of 0.1387 W m^{-2} , and the filled data had a mean difference from the original of 0.1389 W m^{-2} . The files with the gaps inserted into them did a slightly better job than the filled data. All sensible heat fluxes were less than 10% different from the calculated sensible heat fluxes from the full dataset. These percentages are much smaller than those seen with the April dataset as the sensible heat flux values are higher. For example, a change of the same magnitude in May would yield a lower percentage as the overall values are higher. This section contained the most points of the three Barrow datasets, with 28 data points, and shows that the filled data matches the original well.

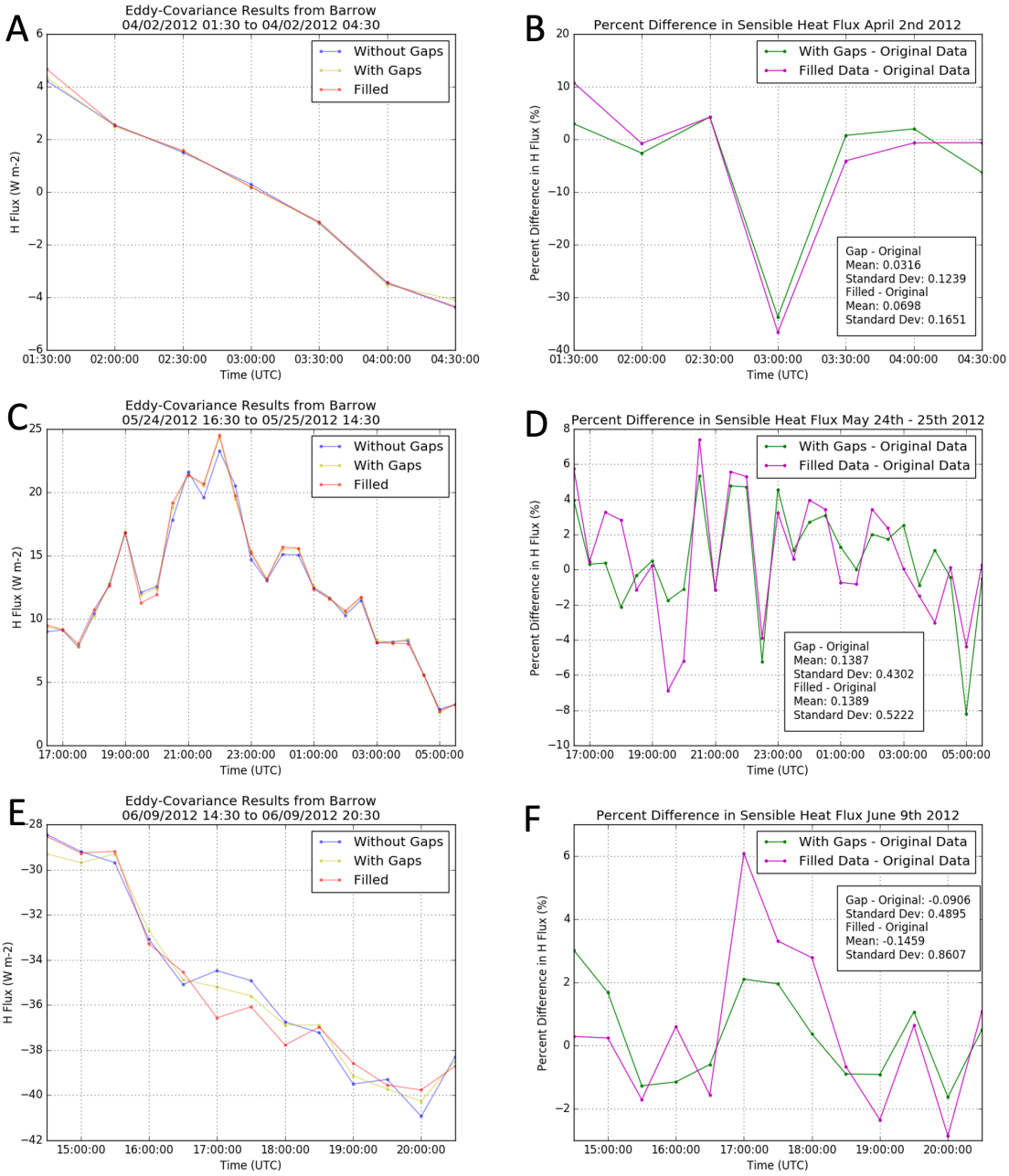


Figure B.1: Sensible heat fluxes calculated from the Barrow, Alaska data (left) for April, May, and June. The calculations using the entire dataset (without any artificial gaps) are represented by the blue lines, the calculations done with the data the gaps inserted, but not filled, are shown with the yellow line, and the calculations done with the filled data are shown with the red line. Percent differences from the original, complete dataset are shown on the left. Percent differences calculated using Eq. B.1 are shown in green, and Eq. B.2 are shown in purple. Mean differences and standard deviations are shown for the values (not the percent differences) for both cases in the left figures.

The section of data from June again showed that the data with gaps inserted into it did a better job at calculating the fluxes than the data with gaps inserted into it. This section of data contained 13 30-minute data files. The mean difference from the original for the data with gaps was -0.09065 Wm^{-2} , and the mean difference from the original for the filled data was -0.14593 Wm^{-2} . The sensible heat flux pattern here was captured reasonably well by the filled data and the data with gaps, but it can be seen by looking at Figure B.1 E that the sensible heat flux calculated using the data with gaps did follow the original sensible heat flux pattern better than the filled data calculations did. This is further emphasized in the percent difference figure (Figure B.1 F), showing that the largest percent difference in sensible heat flux using the data with gaps from the original sensible heat flux was approximately 3%, while the percent difference using the filled data was as large as 6%. These percentages are, again, smaller than other months because of the larger magnitude of the sensible heat values, looking at the time series of sensible heat calculations, a larger discrepancy than in any of the other months can be seen around 1700, yet the percent differences are still smaller than other months.

In each individual month, the data with the gaps inserted into it appeared to portray the original data better than the filled data did when run through EddyPro to calculate sensible heat fluxes. However, all differences were quite small, as could be seen in the mean difference calculations, and the sensible heat flux pattern was conserved throughout calculations using all datasets. Because each dataset from Barrow was relatively small, with the largest dataset containing only 28 points (May), a mean of all Barrow differences was calculated. These means were 0.0593 Wm^{-2} , and 0.0498 Wm^{-2} for the filled data calculations and the calculations using the data

with gaps, respectively. While this shows that the data with the gaps did a better job at calculating sensible heat fluxes, the differences in these means are so small that it can be said that they both did a fine job of estimating sensible heat fluxes.

It seems intuitive that, because the data with gaps did a better job of calculating the actual sensible heat flux than the filled data did, the data with gaps is a better representation of the heat fluxes. While this may be the case, the filled data was still selected to be used with the N-ICE data. As mentioned in the previous section, EddyPro has a missing data allowance threshold, causing some of the data with a large number of gaps to be removed from processing. Filling the gaps ensures that the data will be processed by EddyPro, making all collected data useable regardless of the gaps. This makes the process of gap filling worth doing, even if it has a slightly larger departure from the actual heat fluxes than the data before the gaps are filled.

Spectral differences

One of the products calculated by EddyPro is the power spectra of the wind components at a number of frequencies. This shows the frequencies at which the turbulent motion is occurring, higher power indicates that the eddies have more efficient heat transport. Larger eddies have lower frequencies but often have a greater amount of heat transport as they likely have more mass and momentum. On the other hand, smaller eddies have higher frequencies, and, while they do not have the ability to transport as much heat as a larger eddy, they occur much more frequently (Cohen et al., 2015).

To determine if we are impacting the power going to the different turbulent spectral frequencies by filling the data, the spectra calculations done with the Barrow dataset were examined. To find the difference between the spectral power at each

frequency before and after the filling, the mean monthly percent difference was calculated and is shown in Figure B.2. These are not truly monthly means, as they are only a few days of the month at most. It should also be noted that the frequency of the data gaps was determined by the “worst-case scenario” of data gaps in the original dataset. It is likely that larger spectra differences were seen with this situation at specific frequencies due to the regularity of the data gaps and filling.

Many missing data points existed at high frequencies, so the first 8 frequencies were removed. High-frequency eddies were not impacted by the data-filling method, as can be seen in all plots shown in Figure B.2. The largest total impact on the turbulent spectra is seen just after a frequency of 10-2 Hz. At this point, spikes in the turbulent spectra of all components of the wind (W , V , and U) can be observed. The largest spikes at this point are the V wind component spectra, reaching as high as approximately 450% difference in April. A second spike can be seen just after the first, halfway between 10-2 and 10-1 Hz. The V component of the wind is, again, the most impacted at this frequency for almost all of the months. An exception is in May, where the U component of the wind has a slightly larger percent difference than the V component. These two frequencies are the only frequencies at which percent differences exceed 100% of the original. This indicates that the frequencies affected most by the data filling are at approximately 0.0192 Hz and 0.2257 Hz. It is important to be aware that turbulent energy at these frequencies is affected by the gap-filling process.

B.3.2 N-ICE Filled Data Comparison

When comparing the time series of filled data with the data containing gaps from the N-ICE project, there is not an obvious difference in the calculated sensible heat

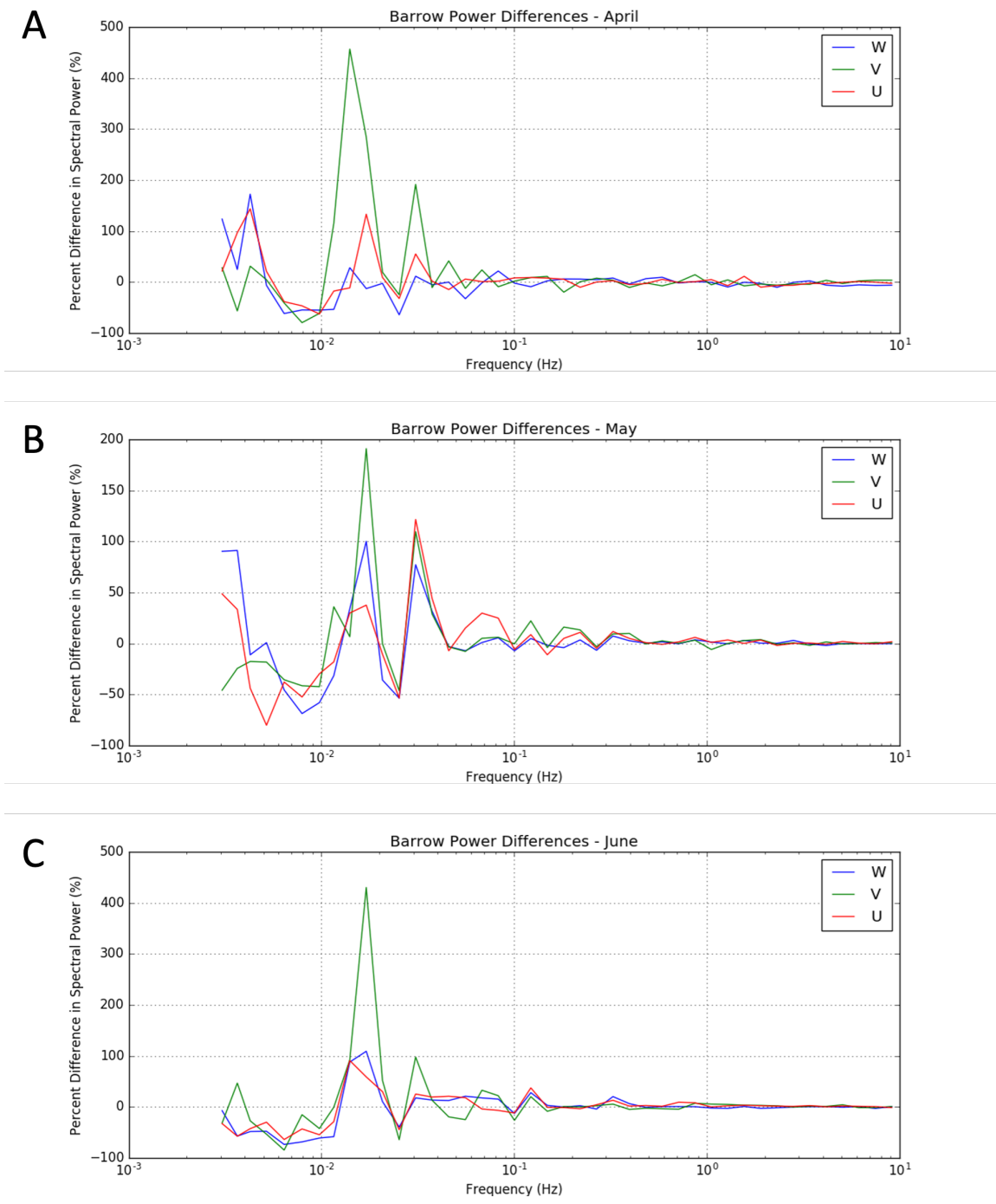


Figure B.2: The percent difference in mean monthly spectra calculated by the filled data from the original data (Eq. B.1) for April, May, and June. The W, V, and U components of the wind are shown in blue, green, and red, respectively.

fluxes. Examining the time series for section 1 (Figure B.3 A) shows little to no difference between the two. Figure B.4 A displays the percent differences between the two calculations and shows that the differences are close to zero until the last day of the dataset, with the largest difference not exceeding 200% of the heat flux calculation by the original dataset. In addition, this difference occurs during an apparent data spike, which is likely not an accurate measurement. Regardless of the spike, this difference is relatively low compared to the differences found in the other two sections (Figure B.3 B and Figure B.3 C and Figure B.3 B and Figure B.3 C), where magnitudes of differences can reach as high as over 2000%. It should be noted that in section 3 there is a location with a difference of 30 Wm^{-2} , which equates to over a 10000 % difference (around 25 May), but this is just one point, and when compared with the time series shown in Figure B.2, it becomes obvious that this is the location of a spike that is likely an error in the data, and not necessarily a calculation error. The largest differences often occur when these spikes occur, indicating something else interfering with the data other than the filling calculations. When these spikes are disregarded, percent differences generally stay around or under 500%, with some exceptions in the second and third sections of data. Throughout the entire time series shown in Figure B.3, the patterns seen in the sensible heat flux are conserved in both calculations. This further confirms that the filling of the data, while often making the flux calculations a bit further from the actual fluxes, can conserve any trends in the data while ensuring that all files can be used in the calculation.

B.4 Future Work

The best option for improving any data-filling method is eliminating the need for it. An examination of the instruments used for this project along with any external factors that could be influencing the data collection should be conducted to determine why these semi-regular and random data gaps are occurring throughout the data set. While some gaps in data can be expected, something had to have been causing the semi-regular data gaps to occur for one minute every five minutes throughout the majority of the project. At this point, however, determining the source of error in the instruments will not help this dataset, but could improve data collection in the future, removing the need for a data-filling method.

The next steps in this project are expanding the dataset the method is being checked with or using a different dataset with more similar conditions to the N-ICE data. The dataset from Barrow, Alaska used, while complete, was a tiny dataset, and was not over newly formed sea ice. Using a longer dataset would improve the percent differences in the turbulent spectra, as these were averages over the short period of time used here.

Another thing to consider when studying the results presented here is the meteorological conditions occurring. If meteorological data were compared to the differences in the fluxes calculated by the original and filled data from Barrow, it is possible that it could be determined what conditions this filling works best in and where it is less effective. This could help to determine if this data-filling method is the correct one for certain project sites. In addition, looking at the changes in the latent heat flux could also give valuable information about how the data filling is impacting the data processing. Lastly, inserting a variety of different gaps into the test dataset would give

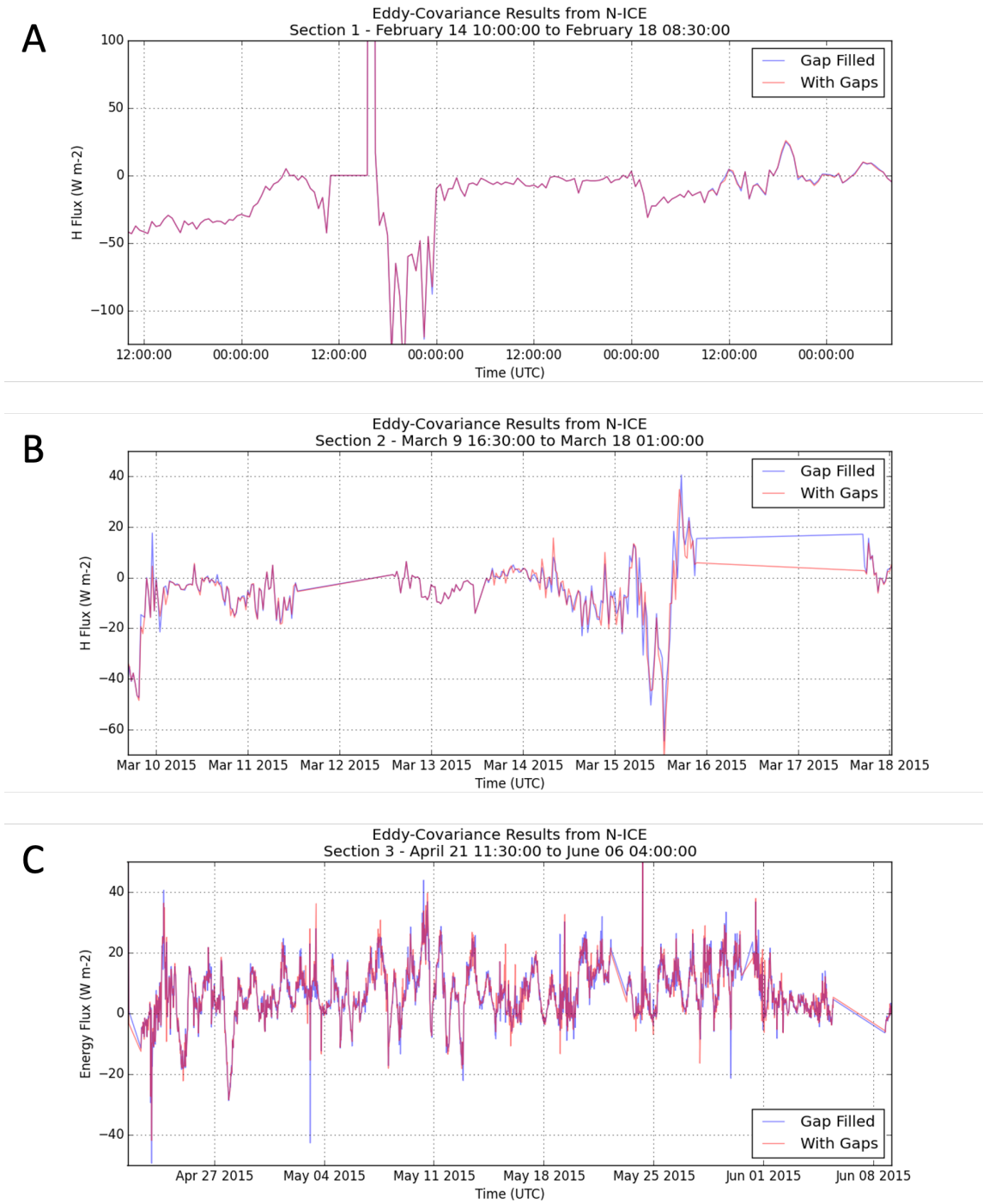


Figure B.3: Sensible heat flux (W m^{-2}) values for each of the three sections of N-ICE data. Both calculations were done with the original data (with gaps, shown in red), and the filled data (gap filled, shown in blue).

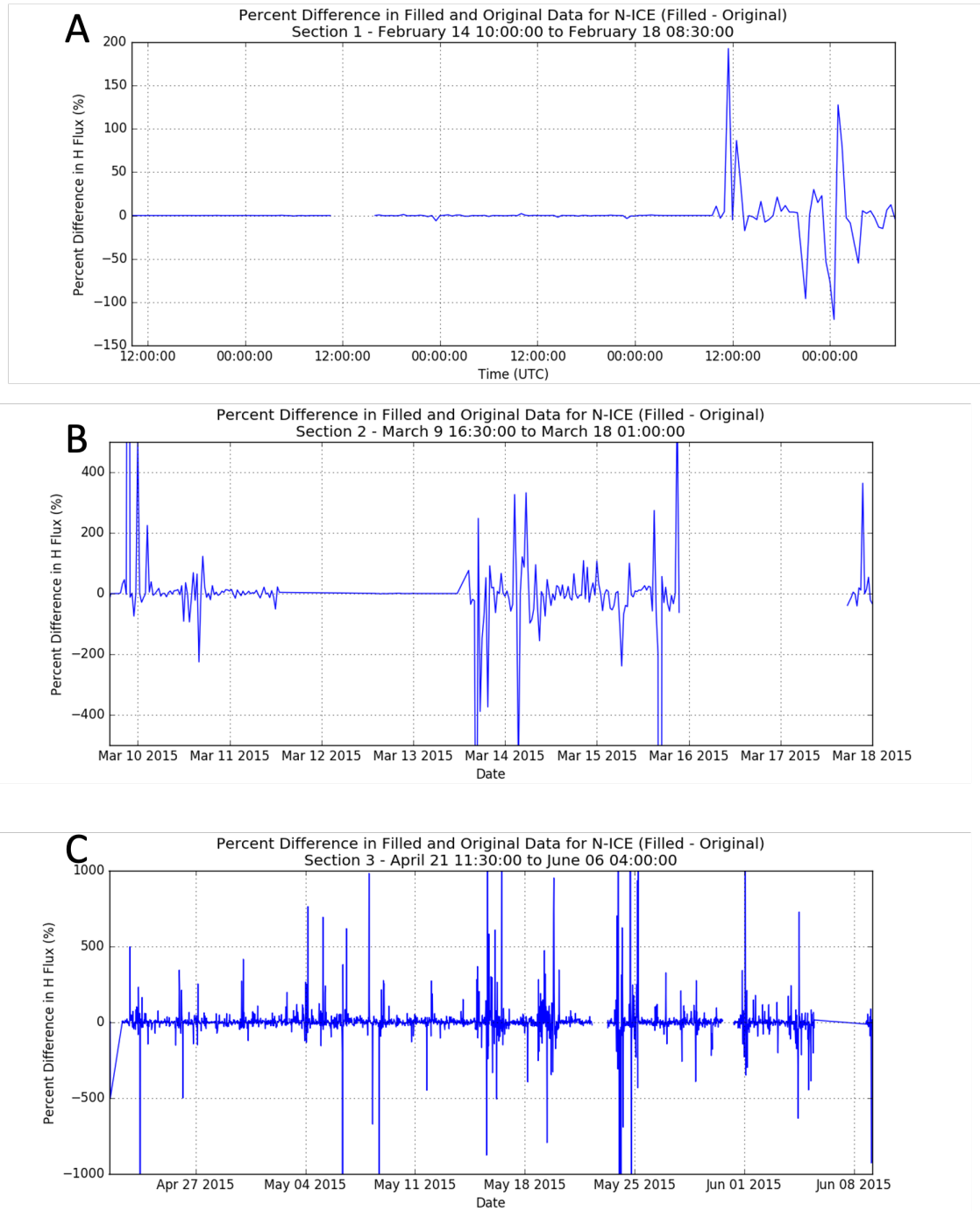


Figure B.4: The percent differences between the original dataset and the filled N-ICE dataset (each dataset shown in Figure B.3). Percent differences were calculated by subtracting the filled calculations from the original (data with gaps) and dividing by the original values, then multiplying by 100. Note the differences in axis range from one section to the next.

valuable information about the size of the gaps that this filling technique is effective for and how random data gaps change the turbulent spectra.

B.5 Conclusion

The N-ICE dataset has a number of problems, including sections of missing data. Some of the data is missing at regular intervals and some sections of missing data are random. Because of the missing data allowance threshold that EddyPro holds the data to, some of the 30-minute data files were being removed from processing, leading to an (even more) incomplete set of data. To fix this problem, a filling technique needed to be developed that did not negatively impact the calculations of the sensible heat flux.

The technique of filling gaps in eddy covariance data with a replica of the section of time before (or after, if there is not enough data before the gap) is shown to conserve trends in sensible heat flux data after processing. Small percent differences between known sensible heat flux values and sensible heat flux values calculated with the filled data were seen (less than 10% with the exception of one point) when the filling technique described here was applied to a complete dataset with artificial data gaps inserted into it. In addition, spectral power showed small differences for most frequencies with the exception of two, showing the frequencies at which the gap filling influences the spectra, and indicating that the filling does have an impact on the calculated turbulent spectra. This filling technique was deemed acceptable for use with the N-ICE data after examination of the Barrow, Alaska results. This data filling results in a higher number of files being accepted into EddyPro.

APPENDIX C

ADDITIONAL POLAR WRF VALIDATION STATISTICS

Table C.1: Mean model CRF bias (left), mean flux (middle, in parentheses), and mean absolute error (right) (Wm^{-2}). No shortwave CRF values are presented for winter as no shortwave radiation was present until spring. Floe 1 and 2 are considered winter and Floe 3 and 4 are spring. Acronyms represent the MP and PBL schemes (defined in Table 3.2). Rows are ordered by MP scheme and colored by PBL scheme.

| | Winter Net | Spring LW | Spring SW | Spring Net |
|---------------|---------------------|---------------------|---------------------|---------------------|
| G-YSU | -40.9, (16.5), 43.8 | -40.9, (16.5), 43.8 | 17.0, (-7.1), 23.0 | -23.8, (9.4), 28.2 |
| G-MYJ | -39.4, (17.4), 43.0 | -39.4, (17.4), 43.0 | 16.1, (-7.7), 22.7 | -23.3, (9.7), 28.0 |
| G-MYNN | -32.8, (23.5), 38.0 | -32.8, (23.5), 38.0 | 14.8, (-8.5), 21.3 | -18.0, (15.0), 24.0 |
| 5-MYJ | -34.8, (22.8), 39.3 | -34.8, (22.8), 39.3 | 17.5, (-5.7), 22.3 | -17.3, (17.0), 26.7 |
| 5-MYNN | -25.2, (31.1), 32.1 | -25.2, (31.1), 32.1 | 14.1, (-8.9), 20.0 | -11.1, (22.2), 23.3 |
| P3-YSU | -26.2, (30.9), 39.5 | -26.2, (30.9), 39.5 | 13.6, (-10.3), 21.2 | -12.6, (20.5), 28.1 |
| P3-MYJ | -39.4, (17.4), 43.0 | -39.4, (17.4), 43.0 | 16.1, (-7.7), 22.7 | -23.3, (9.7), 28.0 |
| 2-MYJ | -13.2, (41.7), 24.2 | -13.2, (41.7), 24.2 | 8.1, (-14.2), 16.6 | -5.0, (27.5), 20.9 |
| 2-MYNN | 1.6, (55.8), 20.2 | 1.6, (55.8), 20.2 | 65.9, (-16.4), 16.4 | 7.5, (39.4), 19.2 |